High Power Mid-infrared to Ultraviolet-visible Frequency Comb

A Thesis Presented

by

Anthony Catanese

to

The Graduate School

in Partial Fulfillment of the Requirements

for the Degree of

Masters of Arts

in

Physics

Stony Brook University

December 2020

Stony Brook University

The Graduate School

Anthony Catanese

We, the committee for the above candidate, recommend acceptance of this thesis.

Thomas K. Allison — Thesis Advisor
Department of Physics and Astronomy, and Chemistry

Thomas Weinacht — Chairperson of the Committee
Department of Physics and Astronomy

Alan Calder
Department of Physics and Astronomy

This dissertation is accepted by the Graduate School

Matthew Dawber
Graduate Program Director

To all those who gain sheer joy from the pursuit of objective truths.

Acknowledgments

I would like to thank Jay Rutledge, my lab partner, whose contributions were invaluable, including helping me record this data, and co-authoring the OPA publication by writing a great introduction to that paper, which I have adapted a significant portion of for this thesis. And Myles Silfies, who's expertise was key during many pivotal moments in this project, like generating first light from the OPA. Furthermore, I would like to acknowledge the contributions made by Jin, Chris, Peng, Alice, and Sergey. I would like to attribute my introduction to wave mechanics and my understanding of the split-step Fourier algorithm to Tom Weinacht; and express gratitude for Alan Calder's guidance and generosity in allowing us to run the PPLN waveguide simulations on his workstation at IACS. Finally, I would like to thank my advisor Tom Allison, whose enthusiasm and excitement when turning knobs along side us in the lab is infectious, his ability to explain physics by recalling exact formulas on the spot is humbling, and his dedication to producing the best experimental physicists is admirable.

Abstract

The first part of this thesis discusses the development of a 100 MHz repetition rate, 7 W, mid-infrared (MIR) frequency comb. This Optical Parametric Amplifier (OPA) design features two stages of periodically poled lithium niobate (PPLN), which are pumped by a Yb:fiber comb at 1.035 μm and seeded by a Er:fiber comb at 1550 nm. The output of this OPA is 100 fs, 2.9 μm idler pulses, with 7 W average power; and amplified signal pulses at 1.6 μm with 14 W average power. With stabilized high average power, short pulse duration, uniform beam spatial profile, and low noise, this OPA is ideal for further development into a light source to drive high harmonic generation (HHG) in solids.

The second part of this thesis reports on the experiment to generate high harmonics in periodically-polled Lithium niobate (PPLN) waveguides using this MIR frequency comb, and compares this experiment to a simulation which models broadband cascaded nonlinear effects in $\chi^{(2)}$ media. Experimental results from a 2017 experiment performed at NIST are also analyzed in the light of this new simulation. Using evidence from both experiments, an explanation for the physical generating mechanism of the harmonics in PPLN waveguides is offered.

Finally, initial steps are taken toward designing an upgraded signal seed branch to the MIR frequency comb. This improvement will enable the OPA to reach it full potential to generate few-cycle MIR pulses. This final section reports on a model for high repetition rate, nonlinear, Erbium Doped Fiber Amplifier (EDFA) pumped at 980 nm and seeded at 1550 nm. This approach uses a hybrid combination of the two-level approximation laser rate equations coupled to the Generalized Nonlinear Schrodinger Equation (GNLSE) in order to capture, in high fidelity, the physics of laser amplifiers along with the ultrafast pulse propagation effects of dispersion and quadratic nonlinearity in optical fibers.

Contents

List of Figures

1. Introduction

1.1 Motivation

The extension of optical frequency comb techniques to the mid-infrared (mid-IR) have been mainly motivated by their applications, which can be broadly categorized by their power requirements. The low power applications ($<$1 W) are adequate for molecular spectroscopy, and lately topics of interest have been spectroscopy in the "fingerprint" region [14, 71] and trace-gas sensing with high discrimination [22, 54]. Therefore, the development of mid-infrared combs at the $<$1 W level for molecular spectroscopy has thus been an area of intense activity.

In addition to spectroscopy, frequency combs in the mid-infrared (MIR) are an excellent sources for driving nonlinear optics in solids. It is these applications, which require high laser power ($>$1 W) [1]. The 2-5 μm wavelength range is particularly attractive because it offers a pivot to generating both ultraviolet-visible (UV-VIS) frequency combs via high harmonic generation (HHG) [25, 30, 60], and

---

[1] For the purpose of driving nonlinear optics peak power is the relevant metric. Here we are considering $\sim$ MHz pulsed laser systems with $\sim$ fs pulse durations in order to make this broad categorization

broadband infrared combs via difference frequency generation (DFG)[24, 74] or supercontinuum generation [65].

For the purpose of developing these high power drivers, frequency combs based on Optical Parametric Amplification (OPA) offer several advantages. Since no energy is stored in the parametric gain medium, which causes excessive heating, the only high power limitation is crystal burning. And with DFG combs based on multiple branches, the separate branches can be amplified to high average powers in fiber amplifiers. [21, 50, 80]. Also, building multiple amplification stages in series is relatively simple, and can achieve higher powers than one single stage.

For nonperturbative nonlinear optics sensitive to the phase of the electric field (e.g. solid-state HHG), OPAs based on DFG between a pump and signal derived from the same comb are particularly attractive due to passive elimination of the carrier-envelope offset frequency, f_0, producing a train of carrier-envelope phase (CEP) stable pulses [9, 36]. This stands in contrast to competing technologies based on Cr:ZnS [73] or Tm:fiber [42], for which it is nontrivial to stabilize f_0 to zero.

A variety of mid-IR frequency comb technologies have emerged over the last decade, among them mode-locked quantum cascade lasers [33], microresonator combs [46], and combs based on optical parametric amplifiers (OPA) [63] and optical parametric oscillators (OPO) [1].

The first part of this thesis presents a 2.9 μm frequency comb based on high-power DFG in a two-stage OPA, operating at 100 MHz repetition rate with 6.7 W average power and 100 fs pulse duration. To our knowledge, this remains

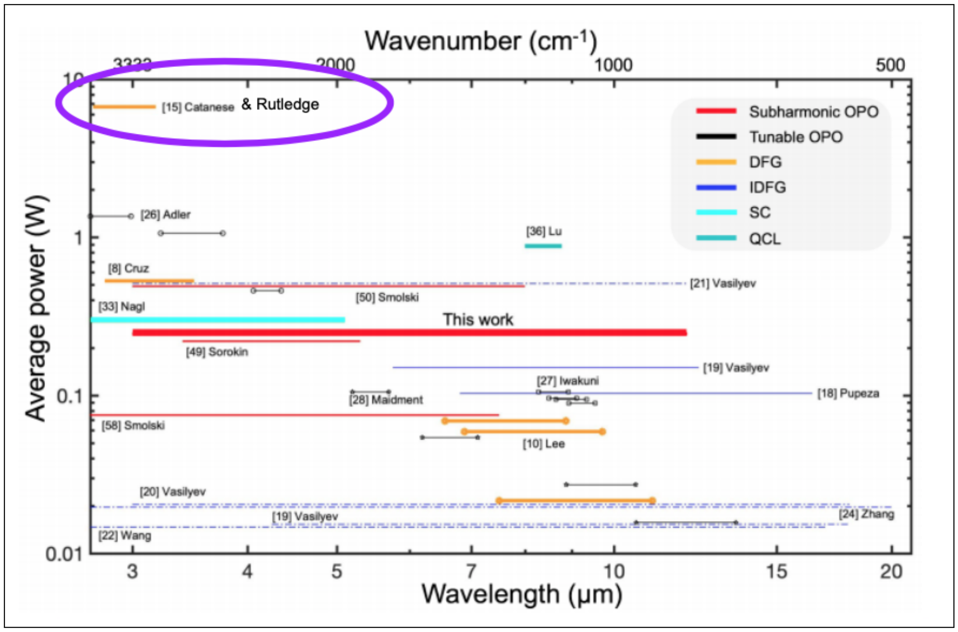

Figure 1.1: Comparison of the average power of MIR frequency combs vs. wavelength. The purple circle indicates the work done in this thesis, which should not be confused with "This work" since this figure was published by [62]

.

the highest power mid-IR optical frequency comb reported to date (figure 1.1) and among the highest average power ultrafast mid-IR light sources in general. Furthermore, we demonstrate that this OPA has the potential to generate sufficient bandwidth to support few-cycle mid-IR pulses with further refinement of the seeding signal branch.

Frequency combs which extend from the MIR to the UV-VIS are continuously advancing the fields of spectroscopic sensing for chemical detection, identifying infectious disease through breath analysis, trace gas monitoring in the oil and gas industry, atomic clocks, quantum memories, imaging of nanometer scale structures, attosecond pulse generation, and calibration of astronomical spectrographs. [4, 23, 64, 79]. Originally designed for atomic clocks, frequency combs provide an optical clockwork which enables counting atomic oscillations which are about 10^5 times faster than Cesium clocks, which allows for unprecedented precision in the measurement of time (on the order of 1 part in 10^{18}) [32, 72]. Today, the frequency comb remains on the forefront of precision measurement technology, and recently it has been proposed to use widely tuneable cavity enhanced frequency comb spectroscopy for human breath analysis [29]. Well resolved spectra could possibly be used to detect Covid-19 by identifying a change in cells metabolism.

The second part of this thesis presents the results of an experiment to generate a broadband MIR to UV-VIS frequency comb using our MIR frequency comb as a driver for high harmonic generation (HHG) in periodically polled lithium niobate waveguides (PPLN). Experimental results are shown to be consistent with a simulation of cascaded $\chi^{(2)}$ processes, which answers a question first proposed by [30] and the Scott Diddams group at NIST—"By what mechanism is the light generated in PPLN waveguides?".

In the third part of this thesis I present a novel model for simulating pulse propagation down Erbium doped gain fiber, which is the active element in the Erbium Doped Fiber Amplifier (EDFA) that generates the OPA's signal seed. This high fidelity EDFA model designed for a MHz repetition rate, picosecond pulse duration, non-linear EDFA, combines elements including pump absorption, amplified stimulated emission, excited state population depletion, and gain saturation; along with fiber dispersion and non-linearity; and consideration to multiple pumps which are co-propagating and counter propagating with the signal. Although my analysis focuses on only 1 piece of the next generation OPA signal seed branch, in the appendix I have included code which solves the Generalized Nonlinear Schrodinger Equation (GNLSE). This code can be easily be adapted to model the entire next generation EDFA system. This is the first step to further refining the signal seed branch of the OPA in order to generate the bandwidth needed to support few-cycle MIR pulses.

1.2 What is a Frequency Comb?

A frequency comb is the spectrum of a laser that emits a pulse train that is periodic in time and has a stable carrier envelope phase (CEP). One way of making a frequency comb is a mode-locked laser (MLL) [2]. Model locking stabilizes the frequency spacing and relative phase of the oscillations within a laser cavity, so that the output spectrum consists of equally spaced frequencies, which resemble the teeth of a comb [68]. The well defined frequencies in a comb are useful for coupling optical clocks to the microwave region of the electromagnetic spectrum, performing molecular spectroscopy, and in general anywhere precise measurement of frequency is required.

Figure 1.2 shows a concept drawing of the spectrogram of a frequency comb, which illustrates the relationship between the time and frequency domain representations of the pulse train generated by a mode locked laser. In the time

---

[2] A MLL is not the only way to make a frequency comb, but the term MLL often appears in the definition of a comb. Other ways to make a frequency combs include (but are not limited to) electro-optic modulation (EOM), optical parametric oscillators (OPO), and microresonators, which can also generate a phase stable pulse train.

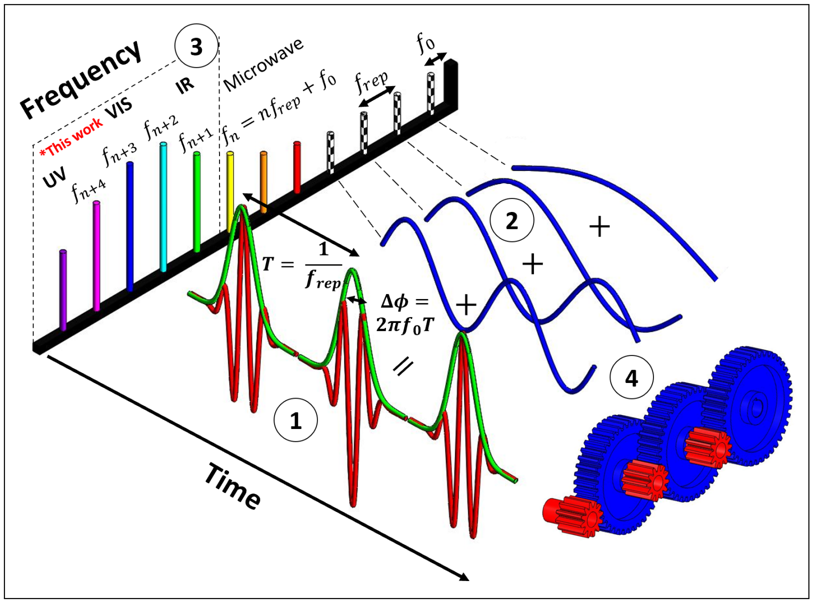

Figure 1.2: Cartoon spectrogram of a frequency comb showing frequency on the y-axis and time on the x-axis. **1)** Time domain representation of a mode locked laser is a pulse train with repetition rate f_{rep}. and carrier envelope phase offset frequency f_0. **2)** This pulse train is constructed from a superposition of laser cavity frequencies which are locked in frequency spacing and relative phase. **3)** In the frequency domain the "comb teeth" are separated by f_{rep} and the spectrum is shifted by f_0 such that the n^{th} frequency component is determined by $f_n = nf_{\text{rep}} + f_0$. Note, this spectrum is not to scale, there are approximately 10^7 comb teeth in the range from the MIR to the UV. **4)** An analogy is often made between a frequency comb and a reduction gear train because both systems have a deterministic frequency and phase.

domain picture the period of the pulse train is $T = 1/f_{\text{rep}}$, where f_{rep} is the repetition rate of the laser, and the carrier envelope phase (CEP) offset per pulse is given by $\Delta\phi = 2\pi f_0 T$, where f_0 (also referred to as f_{ceo}) is the CEP offset frequency. For example, if $f_{\text{rep}} = 100$ MHz and $f_0 = 25$ MHz then the CEP repeats every 4 pulses. The pulse train is constructed from a superposition of the frequencies oscillating within the laser cavity each with frequency f_n and carrier envelope phase offset frequency f_0. Mode locking stabilizes the frequency spacing and relative phases of the oscillations. Fourier transforming into the frequency domain reveals n equidistant constituent frequencies which are spaced by f_{rep} and all share the same carrier envelope offset frequency f_0. Therefore, the frequency of the n^{th} comb tooth is entirely determined by the formula,

$$f_n = f_0 + n * f_{rep} \tag{1.1}$$

A detailed explanation of methods of a model locking a laser is beyond this scope, since this project was not about making a frequency comb from scratch but rather amplification and frequency conversion to the MIR, and then to the UV-VIS, of commercially available comb manufactured by Menlo Systems. A block diagram of this process is shown in figure 1.3.

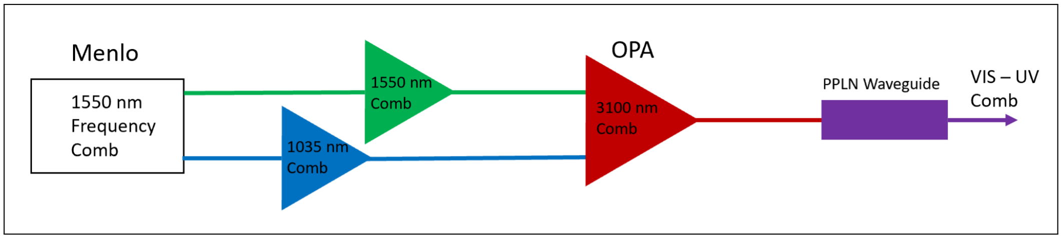

Figure 1.3: We begin with a commercially available 1550 nm, 100 MHz, frequency comb manufactured by Menlo Systems. This is amplified in one branch (green), and also wavelength shifted to 1035 nm and amplified in a second branch (blue). The OPA converts these two wavelengths via DFG to a 3100 nm comb. And the PPLN Waveguide generates harmonics of the 3100 nm light which extend through the visible and into the ultraviolet (down to 330 nm).

I feel it's important to show evidence that the MIR light generated in the OPA and the UV-VIS light generated the PPLN waveguide, are frequency combs (i.e. they obey formula 1.1). Therefore, figure 1.4 shows the heterodyne optical beat frequency measurement between the 2nd harmonic of the OPA pump light (501 nm center wavelength), and the 6th harmonic of OPA MIR light (513 nm center wavelength) generated in the PPLN waveguide. When both signals are incident on a photodiode the resulting beat note generates a voltage which is modulated at the difference between the two carrier envelope phase frequencies according to,

$$f_{beat} = f_{01} - f_{02} \tag{1.2}$$

The 2nd harmonic of the OPA pump has f_{01}, and the 6th harmonic of the MIR light by necessity has $f_{02} = 0$ [3]. Therefore, we would expect a beat note at f_{01} and this is what is shown in the right plot of figure 1.4. It is important to mention that we have only considered a 1 comb tooth in equation 1.2, when in reality there are about 10^6 comb teeth beneath the envelopes in in figure 1.4 (left) which participate in mixing. The amplitude of the beat note is shown for two power settings. The resolution bandwidth limit is 100 KHz [4], and this can be used as a proxy for line width, which indicates that the comb is stable across approximately 1000 pulses.

---

[3] The idler $f_0 = 0$ because it was generated via the difference of two other frequencies with the same f_0, which means this term drops away in the subtraction. All the harmonics of the idler have the same $f_0 = 0$

[4] A resolution bandwidth limit of 100 KHz refers to the fact that at settings below this filter width in the spectrum analyzer the peak amplitude of the signal begins to decrease.

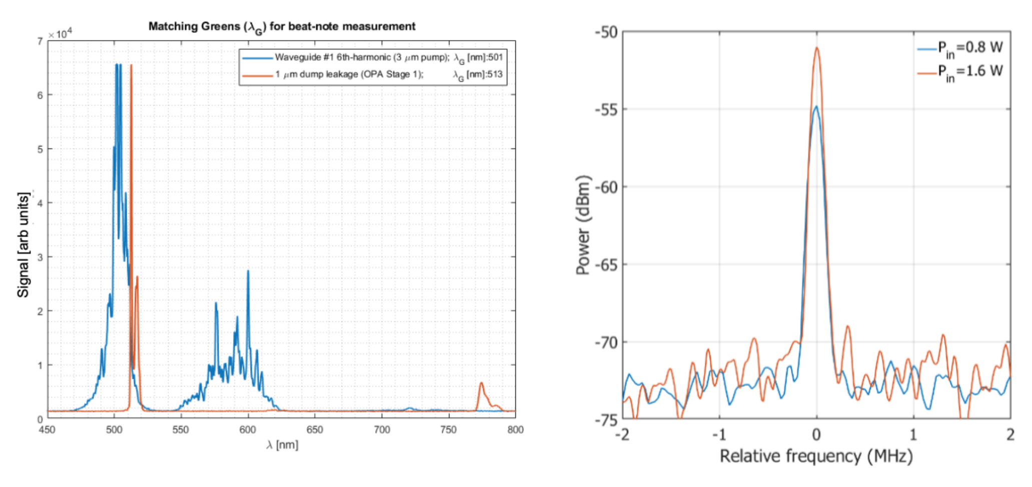

Figure 1.4: Heterodyne measurement used to verify that the light from the OPA, and the light generated in the PPLN Waveguide which is pumped by the OPA, are frequency combs. (Left) green light generated by frequency doubling the 1035 nm OPA pump light (orange) is mixed with 6th harmonic from the PPLN waveguide (blue), and the beat note (shifted down to 0 frequency), shown in the right plot, for 2 power levels, confirms the phase stability of the frequency comb. The RBW is 100 kHz.

1.3 Derivation of the Master Nonlinear Wave Equation

The derivation of the nonlinear wave equation, which describes the interaction of an electric field and a dielectric, begins with Maxwell's equations in SI units.

$$\vec{\nabla} \cdot \vec{D} = \rho \tag{1.3}$$

$$\vec{\nabla} \cdot \vec{B} = 0 \tag{1.4}$$

$$\vec{\nabla} \times \vec{E} = -\frac{\partial \vec{B}}{\partial t} \tag{1.5}$$

$$\vec{\nabla} \times \vec{H} = \frac{\partial \vec{D}}{\partial t} + \vec{J} \tag{1.6}$$

We will assume there is no free charge ($\rho = 0$), no free current ($\vec{J} = 0$), and the material is non-magnetic ($\mu = 1$). However, the material will be allowed to be nonlinearly polarized,

$$\vec{D} = \varepsilon_0 \vec{E} + \vec{P} \tag{1.7}$$

Where the polarization P can be expanded in powers of the electric field.

$$\vec{P} = \varepsilon_0 (\chi^{(1)} \vec{E} + \chi^{(2)} \vec{E}^2 + \chi^{(3)} \vec{E}^3 + ...) \tag{1.8}$$

In general χ^j is a dielectric tensor, but in the case of linearly polarized light $\chi^{(1)}$, $\chi^{(2)}[m/V]$, and $\chi^{(3)}[m^2/V^2]$ are reduced to scalar quantities. The derivation of the wave equation proceeds by taking the curl of Faraday's law, switching the time and space derivatives, using Ampere's law to replace $\vec{\nabla} \times \vec{B}$, making substitutions for $\vec{D} = \varepsilon_0 \vec{E} + \vec{P}$ and $c = 1/\sqrt{\mu_0 \varepsilon_0}$, and finally using a vector identity to replace the triple cross product and dropping the divergence of E (which is making the assumption that the transverse variation of the electric field is small). Then the nonlinear polarization plays the role of a driving term in the wave equation which can be written in the form,

$$\nabla^2\vec{E} - \frac{1}{\varepsilon_0 c^2}\frac{\partial^2 \vec{D^{(1)}}}{\partial t^2} = \frac{1}{\varepsilon_0 c^2}\frac{\partial^2 \vec{P_{NL}}}{\partial t^2} \tag{1.9}$$

Where $\vec{D^{(1)}} = \varepsilon_0\vec{E} + \vec{P^{(1)}} \equiv \varepsilon_0\varepsilon^{(1)}\vec{E}$, and $\varepsilon^{(1)} = 1 + \chi^{(1)}$ is a scalar quantity for an isotropic material, but $\varepsilon^{(1)}$ is a function of frequency ω for a medium with dispersion. And $\vec{P_{NL}} = \varepsilon_0\chi^{(2)}\vec{E}^2 + \varepsilon_0\chi^{(3)}\vec{E}^3 + \ldots$. Making these substitutions we arrive at the time domain wave equation.

$$\nabla^2\vec{E} - \frac{\varepsilon^{(1)}(\omega)}{c^2}\frac{\partial^2\vec{E}}{\partial t^2} = \frac{1}{\varepsilon_0 c^2}\frac{\partial^2 \vec{P_{NL}}}{\partial t^2} \tag{1.10}$$

In the case of discrete frequencies, equation 1.10 can be written as an envelope centered around frequency ω_n as in equation 1.11. In that case the solution can be written as a superposition of waves with frequency ω_n [11].

$$\nabla^2\vec{E}_n - \frac{\varepsilon^{(1)}(\omega_n)}{c^2}\frac{\partial^2\vec{E}_n}{\partial t^2} = \frac{1}{\varepsilon_0 c^2}\frac{\partial^2 \vec{P_n^{NL}}}{\partial t^2} \tag{1.11}$$

The rest of the derivation is structured in order to achieve the same result as in [18], since this is the theory we used to model HHG in PPLN waveguides. Defining the Fourier transform as, $X(\omega) = \mathscr{F}[x(t)] = \int_{-\infty}^{\infty} x(t)e^{-i\omega t}dt$ we can Fourier transform equation 1.10, using the identity $\mathscr{F}[dx(t)/dt] = -i\omega X(\omega)$, and get a frequency domain representation of the nonlinear wave equation for a plane wave propagating in the z direction.

$$\frac{\partial^2 E_\omega}{\partial z^2} + \frac{\omega^2}{c^2}\varepsilon(\omega)E_\omega = \frac{-\omega^2}{\varepsilon_0 c^2} P_{NL\omega} \tag{1.12}$$

In the case of no nonlinearity, the right hand side of this equation is 0 and the solution is $E_\omega(z,\omega) = U_\omega e^{ik(\omega)z}$, where U_ω is a constant, and the dispersion relation is $k(\omega) = \omega/c\sqrt{\varepsilon(\omega)}$. If the nonlinear polarization is considered to be a small perturbation, then this equation can be solved using the slowly varying envelope approximation where U_ω is considered to be a slowly varying function of space and frequency, so we write $E_\omega(z,\omega) = U_\omega(z,\omega)e^{ik(\omega)z}$. Taking derivatives and plugging the expression for E_ω into the left hand side of equation 1.14 we find,

$$\frac{\partial^2 U_\omega}{\partial z^2} - 2ik(\omega)\frac{\partial U_\omega}{\partial z} = \frac{-\omega^2}{\varepsilon_0 c^2} P_{NL\omega} e^{ik(\omega)z} \tag{1.13}$$

In the slowly varying envelope approximation (SVA) the second derivative is dropped, which is valid when the change in envelope is small on the scale of the wavelength, $\partial_z U_\omega << 2k|U_\omega|$. After transforming back to E_ω, the equation referred to as the forward Maxwell equation is obtained.

$$\frac{\partial E_\omega}{\partial z} + ik(\omega)E_\omega = \frac{-i\omega^2}{2\varepsilon_0 c^2 k(\omega)} P_{NL\omega} \tag{1.14}$$

Next we define a real electric field consisting of a slowly varying real envelope $B(z,t)$ multiplied by a real carrier wave with a time dependent phase $\phi(t)$ defined by equation 1.15

$$E(z,t) = B(z,t)cos(\omega_0 t - k_0 z + \phi(t)) \tag{1.15}$$

Equivalently we can define the electric fields using a complex envelope $A(z,t) = B(z,t)e^{i\phi(t)}$ as given by equation 1.16.

$$E(z,t) = \frac{1}{2}A(z,t)e^{i\omega_0 t - ik_0 z} + \frac{1}{2}A^*(z,t)e^{-i\omega_0 t + ik_0 z} \tag{1.16}$$

For instance $A(z,t)$ could be a Gaussian envelope with a quadratic time dependent phase which can be written like [2],

$$A(z,t) = e^{\frac{-(1+iC)t^2}{t_0^2}} \tag{1.17}$$

Where C is a dimensionless constant which gives the magnitude of the chirp. Fourier transforming 1.16, using the identity $\mathscr{F}[x^*(t)] = X^*(-\omega)$ yields,

$$E(z,\omega) = \frac{1}{2}A(z,\omega-\omega_0)e^{-ik_0 z} + \frac{1}{2}A^*(z,-\omega-\omega_0)e^{ik_0 z} \tag{1.18}$$

This formula says that the spectrum of the real electric field $E(z,t)$ is double sided with each envelope centered around $+w_0$ and $-w_0$. We will write 1.16 as real part the complex envelope multiplied by a complex carrier wave,

$$E(z,t) = Real\{A(z,t)e^{iw_0 t - ik_0 z}\} \tag{1.19}$$

Taking a standard approach, we will plug in the entire complex electric field into equation 1.14, knowing that we can always just take the real part at the end to recover the physical electric field. So we write,

$$E(z,t) = A(z,t)e^{iw_0 t - ik_0 z} \tag{1.20}$$

And its Fourier transform, which is a single sided spectrum containing only the positive frequency components,

$$E(z,\omega) = A(z,\omega - \omega_0)e^{-ik_0 z} \tag{1.21}$$

Defining a relative frequency grid $\Omega = \omega - \omega_0$ we write the trial solution we will plug into equation 1.14

$$E_\omega = A(z,\Omega)e^{-ik_0 z} \tag{1.22}$$

Similarly, the polarization envelope can be defined as,

$$P_{NL_\omega} = A_p(z,\Omega)e^{-ik_0 z} \tag{1.23}$$

Note that the envelopes defined here contain only positive frequencies if we are considering the absolute frequency grid, and on the relative frequency grid Ω the envelope has support in the domain $[-\omega_0, \infty]$. Plugging 1.22 and 1.23 into equation 1.14 yields an envelope equation given by 1.24,

$$\frac{\partial A(z,\Omega)}{\partial z} - ik(\omega_0)A(z,\Omega) + ik(\omega)A(z,\Omega) = \frac{-i\omega^2}{2\varepsilon_0 c^2 k(\omega)} A_p(z,\Omega) \tag{1.24}$$

This equation can be simplified by Taylor expanding the dispersion curve according to 1.25 and canceling the constant phase offset term $k(\omega_0)$.

$$k(\omega) = k(\omega_0) + \frac{\partial k}{\partial \omega}\Big|_{w_0} \Omega + \frac{1}{2}\frac{\partial^2 k}{\partial \omega^2}\Big|_{w_0} \Omega^2 + \frac{1}{6}\frac{\partial^3 k}{\partial \omega^3}\Big|_{w_0} \Omega^3 + \dots \tag{1.25}$$

Adopting the standard notation where, $\beta(\omega) = Re[k(\omega)]$, and $\beta_m = \frac{\partial^m \beta(\omega)}{\partial \omega^m}\Big|_{\omega_0}$, equation 1.24 can be re-written in the following way,

$$\frac{\partial A(z,\Omega)}{\partial z} + \Big(i \sum_{m=1}^{\infty} \frac{1}{m!} \beta_m \Omega^m\Big) A(z,\Omega) = \frac{-i\omega^2}{2\varepsilon_0 c^2 k(\omega)} A_p(z,\Omega) \tag{1.26}$$

Note that by choosing to discard the imaginary part of $k(\omega)$ we are neglecting absorption, but this is reasonable in the regions where the material is transparent because the propagation lengths are short. And where the material absorbs strongly, like above the band gap in PPLN, absorption is manually added back in. Using the approximation $k(\omega) \approx \frac{\omega}{c} n_0$, which is valid if $\frac{\partial n(\omega)}{\partial \omega}\Big|_{\omega_0} \cdot \omega_0 << n(\omega_0)$ (which in words says the index of refraction doesn't vary dramatically with frequency), the right hand side of equation 1.26 can be rewritten as,

$$\frac{\partial A(z,\Omega)}{\partial z} + \Big(i \sum_{m=1}^{\infty} \frac{1}{m!} \beta_m \Omega^m\Big) A(z,\Omega) = \frac{-i\omega}{2 n_0 c \varepsilon_0} A_p(z,\Omega) \tag{1.27}$$

Inverse Fourier transforming equation 1.27 yields the time domain representation. Performing the inverse transform of the right hand side proceeds in the following manor.

$$\mathscr{F}^{-1}\Big\{\frac{-i\omega}{2n_0c\varepsilon_0}A_p(z,\Omega)\Big\} = \frac{-i}{2n_0c\varepsilon_0}\int_{-\infty}^{\infty}\omega A_p(z,\omega-\omega_0)e^{-i\omega t}d\omega \tag{1.28}$$

$$= \frac{-i}{2n_0c\varepsilon_0}\int_{-\infty}^{\infty}(\Omega+\omega_0)A_p(z,\Omega)e^{-i(\Omega+\omega_0)t}d\Omega \tag{1.29}$$

$$= \frac{-i}{2n_0c\varepsilon_0}e^{-i\omega_0 t}\int_{-\infty}^{\infty}(\Omega+\omega_0)A_p(z,\Omega)e^{-i\Omega t}d\Omega \tag{1.30}$$

$$= \frac{-i}{2n_0c\varepsilon_0}e^{-i\omega_0 t}\Big[-i\frac{\partial}{\partial t}A_p(z,t)+\omega_0 A_p(z,t)\Big] \tag{1.31}$$

$$= \frac{-ie^{-i\omega_0 t}}{2n_0c\varepsilon_0}\omega_0\Big[1-\frac{i}{\omega_0}\frac{\partial}{\partial t}\Big]A_p(z,t) \tag{1.32}$$

The inverse transform of the left hand side is simpler, and putting it all together yields,

$$\frac{\partial A(z,t)}{\partial z} + \Big(i\sum_{m=1}^{\infty}\frac{1}{m!}\beta_m\Big(-i\frac{\partial}{\partial t}\Big)^m\Big)A(z,t) = \frac{-i}{2n_0c\varepsilon_0}\omega_0\Big[1-\frac{i}{\omega_0}\frac{\partial}{\partial t}\Big]A_p(z,t) \tag{1.33}$$

Equation 1.33 is currently in a lab reference frame defined by time t, but can be shifted in time into a frame τ which is moving at the group velocity of the pump pulse, $\tau = t - \beta_1 z$, by subtracting off the tilt of the dispersion curve (i.e. the linear term in the Taylor expansion). Then equation 1.33 becomes 1.34 in the co-moving frame.

$$\frac{\partial A(z,\tau)}{\partial z}+\Big(i\sum_{m=2}^{\infty}\frac{1}{m!}\beta_m\Big(-i\frac{\partial}{\partial\tau}\Big)^m\Big)A(z,\tau)=\frac{-i}{2n_0c\varepsilon_0}\omega_0\Big[1-\frac{i}{\omega_0}\frac{\partial}{\partial\tau}\Big]A_p(z,\tau) \tag{1.34}$$

Equation 1.34 is the Master Nonlinear Wave Equation, and is also known as the Generalized Nonlinear Schrodinger Equation (GNLSE) [18]. To illustrate how this formula works I will use it to derive the coupled equations for Difference Frequency Generation (DFG) which are used to model the OPA we built; then extend this formula to the continuum to model high harmonic generation (HHG) in Periodically Polled lithium niobate (PPLN) waveguides; and finally formulate the equation which is applicable to ultra short pulses in optical fibers, which I used to generate the high fidelity model of an Erbuim Doped Fiber Amplifier (EFDA) in the final section of this thesis.

1.3.1 Derivation of the Coupled DFG Equations From the Master Nonlinear Wave Equation

For non-centrosymmetric [5] materials like lithium niobate, with a $\chi^{(2)}$ response, the nonlinear polarization coupling between three light fields, $\omega_1, \omega_2, \omega_3$

---

[5] Non-centrosymmetric means the material lacks inversion symmetry, which means when the sign of the electric field is flipped $E \rightarrow -E$ the sign of the polarization stays the same.

is expanded according to equation 1.35

$$\begin{aligned} P_{NL}(z,t) = \varepsilon_0\chi^{(2)}E(z,t)^2 = \varepsilon_0\chi^{(2)}[A_1(z,t)e^{i\omega_1 t-ik_1 z}+A_2(z,t)e^{i\omega_2 t-ik_2 z} \\ +A_3(z,t)e^{i\omega_3 t-ik_3 z}+cc]^2. \end{aligned} \tag{1.35}$$

This mixture of frequencies corresponding to the following processes: second harmonic generation (SHG) $2\omega_1, 2\omega_3, 2\omega_3$, sum frequency generation (SFG) $\omega_1 + \omega_2,\ \omega_2+\omega_3,\ \omega_3+\omega_1$, and difference frequency generation (DFG) $\omega_3-\omega_1,\ \omega_3-\omega_2,\ \omega_2-\omega_1$. In the case of difference frequency generation (DFG) one considers mixing a high energy pump ω_3, signal frequency ω_2 and idler frequency ω_1. From energy conservation, $\omega_3 = \omega_2+\omega_1$, which can be rearranged into $\omega_1 = \omega_3-\omega_2$ and $\omega_2 = \omega_3-\omega_1$, and the expressions corresponding to these frequency combinations can be pulled out of the expansion of P_{NL}.

The choice to use only the positive frequency components is consistent with our formulation of equation 1.34, where we plugged in a single sided spectrum for the electric field (equation 1.20). The form of $P_{NL}(z,t)$ for DFG is given in equation 1.36. Our choice to neglect the processes which are not intended to be phase matched is justified because the light generated by these processes will be down by an order of magnitude. [6].

$$P_{NL}(z,t) = \varepsilon_0\chi^{(2)}(A_2^*A_3e^{i(\omega_3-\omega_2)t-i(k_3-k_2)z} + A_1^*A_3e^{i(\omega_3-\omega_1)t-i(k_3-k_1)z} \\ + A_1A_2e^{i(\omega_1+\omega_2)t-i(k_1-k_2)z}) \tag{1.36}$$

Because of the superposition principle we can split equation 1.33 into three coupled equations for each light field. Using equation 1.23 we define the idler polarization envelope as,

$$A_p^1(z,t) = \varepsilon_0\chi^2e^{-i\omega_1t+ik_1z}(A_2^*A_3e^{i\omega_1t-i(k_3-k_2)z}) = \varepsilon_0\chi^{(2)}A_2^*A_3e^{-i(k_3-k_2-k_1)z} \tag{1.37}$$

Plugging this into equation 1.33 yields,

$$\frac{\partial A_1(z,t)}{\partial z} + iD'A_1(z,t) = \frac{-i}{2n_0c\varepsilon_0}\omega_0\left[1 - \frac{i}{\omega_0}\frac{\partial}{\partial t}\right]\varepsilon_0\chi^{(2)}A_2^*A_3e^{-i(k_3-k_2-k_1)z} \tag{1.38}$$

Where the dispersion operator $D' = \sum_{m=1}^{\infty}\frac{1}{m!}\beta_m\left(-i\frac{\partial}{\partial t}\right)^m\Big)$. If the pulse duration is greater than 100 fs we can safely drop the self steepening term and equation 1.38 becomes,

$$\frac{\partial A_1(z,t)}{\partial z} + iD'A_1(z,t) = \frac{-i\chi^{(2)}}{2n_0c}\omega_0A_2^*A_3e^{-i(k_3-k_2-k_1)z} \tag{1.39}$$

---

[6] But in reality when one hits a crystal with 50 W of 1035 nm pump light focused down to a 100 μm spot ($\sim 10\ GW/cm^2$), there's a nontrivial amount of SHG (green) and SFG (red) generated

Now we are free to choose what reference frame the system of equations will propagate in, and traditionally the frame is set to the pump. Defining $\delta_{13} = \beta_1^1 - \beta_1^3$ as the group velocity mismatch between the idler and pump, and $\Delta k = k_3 - k_2 - k_1$ as the phase mismatch, and keeping only the group velocity dispersion (GVD) term, we find,

$$\frac{\partial A_1(z,\tau)}{\partial z} + \delta_{13}\frac{\partial A_1(z,\tau)}{\partial \tau} - \frac{i}{2}GVD_1\frac{\partial^2 A_1(z,\tau)}{\partial^2 \tau} = \frac{-id_{eff}\omega_1}{n_1 c}A_2^* A_3 e^{-i\Delta kz} \tag{1.40}$$

Where $\chi^{(2)} = 2d_{eff}$. Using this same approach the final two coupled differential equations can be written out for the signal ω_2 and pump ω_3,

$$\frac{\partial A_2(z,\tau)}{\partial z} + \delta_{23}\frac{\partial A_2(z,\tau)}{\partial \tau} - \frac{i}{2}GVD_2\frac{\partial^2 A_2(z,\tau)}{\partial^2 \tau} = \frac{-id_{eff}\omega_2}{n_2 c}A_1^* A_3 e^{-i\Delta kz} \tag{1.41}$$

$$\frac{\partial A_3(z,\tau)}{\partial z} - \frac{i}{2}GVD_3\frac{\partial^2 A_3(z,\tau)}{\partial^2 \tau} = \frac{-id_{eff}\omega_3}{n_3 c}A_1 A_2 e^{-i\Delta kz} \tag{1.42}$$

In the section which describes the design of the OPA these equations are solved, and the solutions are used to optimize the design of the OPA and predict the power output.

1.3.2 Extension to The Broadband Envelope Equation For $\chi^{(2)}$ nonlinearity

The previous section showed how to derive the DFG equations for three discrete coupled modes, $\omega_1, \omega_2, \omega_3$ using the master equation. We could only do that because we could separate the equations for each of the normal modes frequencies. When we move to a continuous spectrum we must treat the entire envelope accordingly. This section follows the remainder of the derivation in [18].

Beginning with the $\chi^{(2)}$ response we write,

$$P_{NL} = \varepsilon_0 \chi^{(2)} [Re\{A(z,t)e^{i\omega_0 t - i\beta_0 z}\}]^2 \tag{1.43}$$

Where,

$$Re\{A(z,t)e^{i\omega_0 t - i\beta_0 z}\} = \frac{1}{2}A(z,t)e^{i\omega_0 t - ik_0 z} + \frac{1}{2}A^*(z,t)e^{-i\omega_0 t + ik_0 z} \tag{1.44}$$

So we find,

$$P_{NL}(z,t) = \frac{\varepsilon_0 \chi^{(2)}}{4}[A^2 e^{2i\omega_0 t - 2ik_0 z} + A^{*2} e^{-2i\omega_0 t + 2ik_0 z} + 2|A|^2] \tag{1.45}$$

Because the envelope was defined as containing positive frequency components (equation 1.22), the first term in equation 1.45 contains positive frequencies, and is responsible for SFG. The second term contains negative frequencies. And the third term $2|A|^2$ contains a mixture of both, and is responsible for DFG. Also because of this convention , $P_{NL}(z,t)$ must be transformed into an object containing only positive frequency elements. This is done by throwing away the second term in 1.45 and taking the Hilbert transformation, or the analytic signal representation, of the DFG term [18]. This is performed by Fourier transforming into the frequency domain, applying the recipe given in equation 1.46, and then inverse Fourier transforming back into the time domain.

$$AS\{X(\omega)\} = \begin{cases} 2X(\omega), & \text{if } \omega > 0 \\ X(\omega), & \text{if } \omega = 0 \\ 0, & \text{if } \omega < 0 \end{cases} \tag{1.46}$$

Where $AS\{X(\omega)\}$ represents the analytic signal representation. In order to draw a connection between objects consider,

$$A(z,t)e^{i\omega_0 t} \equiv AS[\frac{1}{2}A(z,t)e^{i\omega_0 t - ik_0 z} + \frac{1}{2}A^*(z,t)e^{-i\omega_0 t + ik_0 z}] \tag{1.47}$$

Applying the analytic signal transformation to equation 1.45 yields the correct form of the nonlinear polarization.

$$P_{NL}(z,t) = \frac{\varepsilon_0 \chi^{(2)}}{2}[A^2 e^{2i\omega_0 t - 2ik_0 z} + AS[|A|^2]] \tag{1.48}$$

And calculating the envelope according to the inverse Fourier transform of equation 1.23 which is,

$$A_p(z,t) = P_{NL}(z,t)e^{-i\omega_0 t + ik_0 z} \tag{1.49}$$

The final form of the nonlinear polarization envelope is,

$$A_p(z,t) = \frac{\varepsilon_0 \chi^{(2)}}{2}[A^2 e^{i\omega_0 t - ik_0 z} + AS[|A|^2]e^{-i\omega_0 t + ik_0 z}] \tag{1.50}$$

All that is left to do is cast this equation in a frame which moves with the fundamental frequency by recalling $\tau = t - \beta_1 z$. Plugging this into 1.50 and the entire polarization envelope into the master equation 1.34 yields,

$$\frac{\partial A(z,\tau)}{\partial z} + iDA(z,\tau) = \frac{-i\chi^2}{4n_0 c}\omega_0\left[1 - \frac{i}{\omega_0}\frac{\partial}{\partial \tau}\right][A^2 e^{i\omega_0 t - ik_0 z} + AS[|A|^2]e^{-i\omega_0 t + ik_0 z}] \tag{1.51}$$

Where $D = \sum_{m=2}^{\infty} \frac{1}{m!}\beta_m \left(-i\frac{\partial}{\partial \tau}\right)^m$. In the section of this thesis which describes our experiment to generate high harmonics in chirped PPLN waveguides we solve this equation numerically and compare it to the experimental results.

1.3.3 Derivation of the GNLSE with $\chi^{(3)}$ nonlinearity

In centrosymmetric materials which lack inversion symmetry $\chi^{(2)}$ must identically vanish. This is easy to illustrate with the following example. If $P_{NL} \propto E^2$ and the direction of the electric field is inverted, $E \rightarrow -E$, then the nonlinear polarization clearly remains in the same direction, which contradicts the characteristic of centrosymmetric material. Therefore, $\chi^{(2)}$ must vanish. Many materials including Fused Silica, which is used to make optical fibers, are centrosymmetric, and as a result the next leading order in the expansion of the nonlinear polarization $\chi^{(3)}$

dominates. As usual, the starting point is the general form of the master equation in the frame co-moving at the group velocity of the pump (equation 1.34), which is repeated here,

$$\frac{\partial A}{\partial z} + iDA = \frac{-i}{2n_0 c\varepsilon_0}\omega_0\left[1 - \frac{i}{\omega_0}\frac{\partial}{\partial \tau}\right]A_p \tag{1.52}$$

The nonlinear polarization envelope A_p for cubic media is given by the following equation [3],

$$A_p(z,\tau) = \frac{3}{4}\varepsilon_0\chi^{(3)}A(z,\tau)\int_0^{\infty} R(t\prime)|A(z,\ \tau - t\prime)|^2 dt\prime \tag{1.53}$$

Where the $|A|^2$ under the integral is due to the intensity dependent ($I \propto |A|^2$) index of refraction, and the response function is a sum of Kerr (instantaneous) and Raman (delayed) nonlinearity, which is given by the following formula,

$$R(t) = (1 - fr)\delta(t) + f_R h_R(t) \tag{1.54}$$

Where f_R is the fractional contribution from the Raman response, and $h_R(t)$ is the Raman response function. The exact form of the Raman function h_R depends on the medium and is formulated from experimentally derived quantities. But for illustrative purposes the Raman response $h_R(t)$ resembles a damped harmonic oscillator response with $\sim 50\ fs$ time constant. Plugging equation 1.53 into the right hand side of 1.52 yields,

$$\frac{\partial A}{\partial z} + iDA = -i\frac{3Re\{\chi^{(3)}\}}{8n_0 c}\omega_0\left[1 - \frac{i}{\omega_0}\frac{\partial}{\partial \tau}\right]A\int_0^{\infty} R(t\prime)|A(\tau - t\prime)|^2 dt\prime \tag{1.55}$$

Where I have considered absorption, due to $Im\{\chi^{(3)}\}$ to be negligible, which is reasonable given the relatively short propagation lengths I simulate. It is informative to pause here in order to evaluate units. The units of $\chi^{(3)}$ are $[V/m]^3$, and the electric field is in units $[V/m]$, which makes the left and right hand side units of equation 1.55 consistent in units of $[V/m^2]$. It is a commonly accepted standard to transform equation 1.55 into a form where the electric field has units $\sqrt{W}$ and represents the peak power in the pulse. This can be done using the equivalency $|A\prime|^2[W] = 1/2\varepsilon_0 n_0 c A_{eff}|A|^2[V/m]^2$, in which case the nonlinear scale factor becomes γ $[1/(W\cdot m)]$ and can be calculated by, [3],

$$\gamma(\omega_0) = \frac{\omega_0 n_2}{cA_{\text{eff}}} \tag{1.56}$$

Where n_2 is an experimentally derived quantity known as the Kerr coefficient. But in practice, when working with optical fibers, γ is a parameter supplied by the manufacturer. Putting this all together yields,

$$\frac{\partial A}{\partial z} + iDA = -i\gamma(\omega_0)\left[1 - \frac{i}{\omega_0}\frac{\partial}{\partial \tau}\right]\left((1-f_R)A|A|^2 + A\int_0^{\infty} f_R h_R(t\prime)|A(\tau - t\prime)|^2 dt\prime\right) \tag{1.57}$$

Which is applicable to broadband pulse envelopes that contain few optical cycles, and in the in the case of 1000 nm light this is $>$ 10 fs pulse durations.

It is worth while to point out that this form of the GNLSE is the complex conjugate of the form which appears in a widely accepted standard text "Nonlinear Fiber Optics" by Agrawal. Physically this is inconsequential because the electric field has Hermitian symmetry, so one can solve for the envelope or its complex conjugate. However, when it comes to numerically solving this equation (1.57) it's important to use the following Fourier transform convention, $A_\omega = \mathrm{fft}\{\mathrm{A_t}\}$ and $A_t = \mathrm{ifft}\{\mathrm{A}_\omega\}$, and the derivative is given by $\frac{dA_t}{dt} = \mathrm{ifft}(\mathrm{i}\omega\mathrm{fft}(\mathrm{A_t}))$ If the opposite Fourier transform convention is used then take the complex conjugate of equation 1.57

Equation 1.57 is the final result, and in the section where I model the Erbium Doped Fiber Amplifier (EFDA) I solve this form of the equation numerically using the Matlab code which is in the appendix of this thesis.

2. OPA Simulation

2.1 Numerical Solution to the Coupled Wave Equations for DFG

Optical parametric amplification was modeled in one spatial dimension as a $\chi^{(2)}$, three-wave, mixing of Gaussian pulses using the equations in [49]. These equations are the same as the ones which were derived in the section 1.3.1 of this thesis. Using input pulse parameters supplied by our measurements, and dispersion and nonlinear parameters computed from reported PPLN properties [20], we applied the Fourier split-step method to solve for the power and spectrum in 2 stages of PPLN crystals. These simulations helped determine ideal specifications of stage 1 and 2 for maximum gain and bandwidth support.

The DFG interaction is governed by a system of three coupled partial differential equations [49] for the envelopes of the electric field for idler A_1, signal

A_2, and pump A_3. They are,

$$\frac{\partial A_1}{\partial z} + \frac{1}{2i}\beta_2^1 \frac{\partial^2 A_1}{\partial \tau^2} + \delta_{13}\frac{\partial A_1}{\partial \tau} = -i\sigma_1 A_2^* A_3 e^{-i\Delta k z} \tag{2.1}$$

$$\frac{\partial A_2}{\partial z} + \frac{1}{2i}\beta_2^2 \frac{\partial^2 A_2}{\partial \tau^2} + \delta_{23}\frac{\partial A_2}{\partial \tau} = -i\sigma_2 A_1^* A_3 e^{-i\Delta k z} \tag{2.2}$$

$$\frac{\partial A_3}{\partial z} + \frac{1}{2i}\beta_2^3 \frac{\partial^2 A_3}{\partial \tau^2} = -i\sigma_3 A_1 A_2 e^{i\Delta k z} \tag{2.3}$$

where i is the imaginary unit, β_2^i is the group velocity dispersion (GVD) of each pulse (i=1, 2, 3) in the medium, $\sigma_i = \frac{d_{eff}\omega_i}{cn_i}$ is the nonlinear scale factor for each field at angular frequency ω_i with index of refraction n_i, $d_{eff} = 2/\pi\ d_{33}$ where $d_{33} = \chi^{(2)}/2$ is the dielectric tensor element [34], $\Delta k = k_3 - k_2 - k_1$ is the wavevector mismatch between fields, $\delta_{i3} = \frac{1}{v_{gi}} - \frac{1}{v_{g3}} = \beta_1^i - \beta_1^3$ is the group velocity mismatch (GVM) of either idler or signal relative to the pump field, and L is the crystal length.

In order to calculate the initial electric field envelopes for the idler A_1, signal A_2, and pump A_3 we need to specify the average power P_{ave}, repition rate of the laser f_{rep}, pulse duration τ, and beam waist w. [1] Then we calculate the energy per pulse E_{pp},

$$E_{\text{pp}} = \frac{P_{\text{ave}}}{f_{\text{rep}}} \tag{2.4}$$

---

[1] The convention we use for a Gaussian pulse is $\tau = \frac{FWHM}{2\sqrt{ln(2)}}$, and the beam waist w is the radius at the $1/e^2$ height.

The peak power in a pulse P_{pk},

$$P_{\mathrm{pk}} = \frac{E_{\mathrm{pp}}}{FWHM} * 0.9394 \tag{2.5}$$

Where the factor of 0.9394 is a correction for the peak power of a square pulse to a Gaussian pulse with the same FWHM which contains the same total energy. And finally the peak intensity of the pulse I_0 given by,

$$I_0 = \frac{2P_{\mathrm{pk}}}{\pi w^2} \tag{2.6}$$

Then the pulse intensity envelope as a function of time, with an offset t_0 included to allow a delay between the pump and signal pulses, is given by,

$$I = I_0 e^{\frac{-(t-t_0)^2}{\tau^2}} \tag{2.7}$$

Which can then be converted from intensity $[W/m^2]$ to electric field $[V/m]$ according to,

$$I = \frac{1}{2} n \varepsilon_0 c |A|^2 \tag{2.8}$$

Where c is the speed of light, ε_0 is the permittivity of free space, and n is the index of refraction. Since we are simulating DFG between the pump and signal pulses A_2 and A_3 are calculated according to the previous equations, and A_1 (idler) is initialized to zero.

Looking at the differential equations 2.1 2.2 2.3 there are four parameters which still need to be calculated for each pulse. They are, the group velocity dispersion (GVD) for each pulse β_2^i, nonlinear scale σ_i, the wavevector mismatch Δk, and the group velocity mismatch δ_{i3} of the idler and signal relative to the pump. In order to calculate these parameters we begin with the temperature dependent index of refraction for 5% MgO Lithium Niobate. This is given by the Sellmeier equation and its coefficients which are available from Covesion's website [20]. In order to take advantage of the higher non-linear coefficient all the incident beams must be polarized along the extraordinary axis, which is parallel the thickness of the crystal. The wavenumber is calculated according to,

$$k = \frac{2\pi n(\lambda)}{\lambda} \equiv \frac{\omega}{c} n(\omega) \tag{2.9}$$

Then the group velocity dispersion can be calculated by,

$$\beta_2^i = \left.\frac{\partial^2 k}{\partial \omega^2}\right|_{\omega_i} \tag{2.10}$$

Followed by the nonlinear response,

$$\sigma_i = \frac{d_{\text{eff}} \omega_i}{c n_i} \tag{2.11}$$

Where $d_{\text{eff}} = 14 \times 10^{-6}$[um/V] for PPLN. The group velocity,

$$v_{gi} = \left.\frac{\partial \omega}{\partial k}\right|_{\omega_i} \tag{2.12}$$

And the group velocity mismatch between the signal or idler relative to the pump,

$$\delta_{i3} = \frac{1}{v_{gi}} - \frac{1}{v_{g3}} \tag{2.13}$$

Finally, we calculate the wavevector mismatch between the pulses Δk according to,

$$\Delta k = k_3 - k_2 - k_1 \tag{2.14}$$

Looking at equation 2.1, 2.2, 2.3, it is apparent that the magnitude of the RHS is spatially modulated with a period,

$$\Lambda = \frac{2\pi}{\Delta k} \tag{2.15}$$

Since the RHS governs the gain of the idler, signal, and pump in the OPA, this would suggest that the gain is modulated with a spatial period of Λ. Additionally, since $\Lambda \approx 30\ \mu m$ for idler, signal, and pump wavelengths of 3.11, 1.55, 1.035 μm, and typical PPLN crystal lengths are $\sim 1000\ \mu m$, this would suggest that the idler gain would just oscillate over many cycles, averaging to zero, and the OPA would not be an effective amplifier. However, if we were to subtract another wavevector $2\pi/\Lambda$ such that Δk_{eff} becomes,

$$\Delta k_{\text{eff}} = k_3 - k_2 - k_1 - 2\pi/\Lambda = 0 \tag{2.16}$$

Then the gain of the idler no longer oscillates and becomes $\propto A_2^* A_3$. From an engineering perspective "perfect phase matching" described by this condition is not possible in Lithium Niobate, but Quasi Phase Matching (QPM) is an effective alternative. In OPM the sign of d_{eff} is flipped every half polling period ($\Lambda/2$) by applying a strong electric field to the Lithium Niobate crystal during manufacturing. This gives the electric fields a $-\pi$ phase shift every time they get π out of phase which causes the gain to increase monotonically [11]. This is illustrated in figure 2.1. The curves showing no phase matching, ideal phase matching, and QPM were generated using the solutions to equations (2.1, 2.2, 2.3).

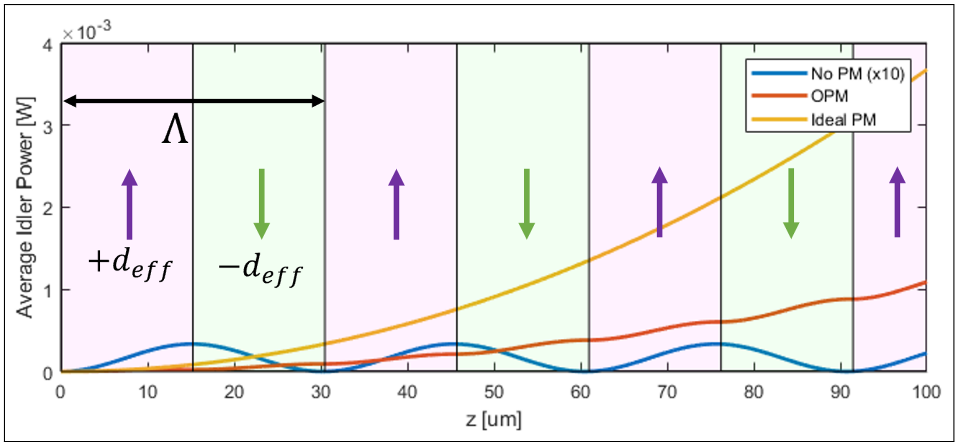

Figure 2.1: Idler power vs. propagation distance z for the first 3 polling periods Λ using the simulation. The effect of no phase matching is shown in blue, ideal phase matching in yellow and quasi phase matching in red.

Note the QPM curve's characteristic "scalloped" gain which is a result of imperfect phase matching throughout the polling period. Having solved for all the simulation parameters, the differential equations can be solved using the Split Step Fourier Method (SSFM).

The SSFM is a numeric procedure used to solve nonlinear partial differential equations of Fourier transform pairs. It involves splitting up the equations into a nonlinear and a linear part and then propagating the nonlinear part in the time domain, Fourier transforming, and then propagating the linear part in the frequency domain. In order to explain the implementation of the method, it's simplest to use the pump envelope A_3 as an example. The differential equation which governs the evolution of the pump envelope is,

$$\frac{\partial A_3}{\partial z} + \frac{1}{2i}\beta_2^3\frac{\partial^2 A_3}{\partial \tau^2} = -i\sigma_3 A_1 A_2 e^{i\Delta k z} \tag{2.17}$$

We begin by splitting this into a nonlinear part.

$$\frac{\partial A_3}{\partial z} = -i\sigma_3 A_1 A_2 e^{i\Delta k z} \tag{2.18}$$

And a linear part which includes the dispersion terms,

$$\frac{\partial A_3}{\partial z} = -\frac{1}{2i}\beta_2^3\frac{\partial^2 A_3}{\partial \tau^2} \tag{2.19}$$

The nonlinear part is exactly solvable if we assume that A_1 and A_2 are constant. Of course they aren't really constant, but if the step in z (which we will denote as h) is small then it is reasonable to treat A_1 and A_2 as constant for this step. Then the equation is separable and the solution is,

$$A_3(z+h) = A_3(z) - \frac{\sigma_3 A_1 A_2}{\Delta k}(e^{i\Delta k(z+h)} - e^{i\Delta k(z)}) \tag{2.20}$$

The simulation can tolerate relatively course steps in z, when the electric field envelopes do not change rapidly. We found that 4 steps per polling period ($h =$

7.6 μm) resulted in a fractional error of only 0.012, after 2 mm of propagation, when compared to 256 steps per polling period ($h = 0.12\ \mu m$), and gave the simulation approximately two orders of magnitude boost in speed.

The linear part is naturally solved in the Fourier domain where we can use the differentiation properties of Fourier transforms. Let A^3_ω and A^3_t be transform pairs of the pump pulse envelope A_3. Then,

$$\frac{d^2A^3_t}{dt^2} \longleftarrow \mathscr{F} \longrightarrow -\omega^2 A^3_\omega \tag{2.21}$$

And the dispersion equation can be Fourier transformed and written as,

$$\frac{\partial A^3_\omega}{\partial z} = \frac{1}{2i}\beta^3_2\omega^2 A^3_\omega \tag{2.22}$$

Which is separable and the solution is,

$$A^3_\omega = A^3_\omega(z=0)e^{-\frac{i}{2}\beta^3_2\omega^2 z} \tag{2.23}$$

This represents the rotation of A^3_ω by a phase angle $\phi = -\frac{1}{2}\beta^3_2\omega^2 z$. Therefore, if we want to propagate A^3_ω by a small step h we compute,

$$A^3_\omega(\omega, z+h) = e^{-\frac{i}{2}\beta^3_2\omega^2 h}A^3_\omega(\omega, z) \tag{2.24}$$

Note that we can easily add a third order dispersion term β^3_3 by adding it to the propagator,

$$A^3_\omega(\omega, z+h) = e^{-\frac{i}{2}\beta^3_2\omega^2 h - \frac{i}{6}\beta^3_3\omega^3 h} A^3_\omega(\omega, z) \tag{2.25}$$

Writing down the dispersion operators for the idler and signal pulses proceed in the same manor, and for completeness the propagation equation for the signal A_2 (including the 3^{rd} order dispersion term) is,

$$A^2_\omega(\omega, z+h) = exp\{-i\omega\delta_{23}h - \frac{i}{2}\beta^2_2\omega^2 h - \frac{i}{6}\beta^2_3\omega^3 h\} A^2_\omega(\omega, z) \tag{2.26}$$

And for the idler A_1,

$$A^1_\omega(\omega, z+h) = exp\{-i\omega\delta_{13}h - \frac{i}{2}\beta^1_2\omega^2 h - \frac{i}{6}\beta^1_3\omega^3 h\} A^1_\omega(\omega, z) \tag{2.27}$$

Finally, we can put together the entire split step method in pseudo code.

```
for j=1:length(z)-1

% Apply the nonlinear operator in the time domain
$At_1 = At_1 + \frac{\sigma_1 At_2^* At_3}{\Delta k}\left(e^{-i\Delta kz[j+1]} - e^{-i\Delta kz[j]}\right)$
$At_2 = At_2 + \frac{\sigma_2 At_1^* At_3}{\Delta k}\left(e^{-i\Delta kz[j+1]} - e^{-i\Delta kz[j]}\right)$
$At_3 = At_3 - \frac{\sigma_3 At_1 At_2}{\Delta k}\left(e^{i\Delta kz[j+1]} - e^{i\Delta kz[j]}\right)$

% Fourier transform to the frequency domain
$A\omega_1 = \mathscr{F} At_1$
$A\omega_2 = \mathscr{F} At_2$
$A\omega_3 = \mathscr{F} At_3$

% Apply the dispersion operator in the frequency domain
$A\omega_1 = exp\{-i\omega\delta_{13}h - \frac{i}{2}\beta_2^1\omega^2 h - \frac{i}{6}\beta_3^1\omega^3 h\}\ A\omega_1$
$A\omega_2 = exp\{-i\omega\delta_{23}h - \frac{i}{2}\beta_2^2\omega^2 h - \frac{i}{6}\beta_3^2\omega^3 h\}\ A\omega_2$
$A\omega_3 = exp\{-\frac{i}{2}\beta_2^3\omega^2 h - \frac{i}{6}\beta_3^3\omega^3 h\}\ A\omega_3$

% Inverse Fourier transform back to the time domain
$At_1 = \mathscr{F}^{-1} A\omega_1$
$At_2 = \mathscr{F}^{-1} A\omega_2$
$At_3 = \mathscr{F}^{-1} A\omega_3$

end
```

By storing the electric field values $At_i(t,z)$ and $A\omega_i(\omega,z)$ at every step in z we have obtained all the simulation data necessary to understand the evolution of the idler, signal, and pump pulses thorough the crystal. Since we are most interested in power buildup in the amplifier, we begin by calculating optical intensity $I(t)$ $[W/m^2]$ given by,

$$I(t) = \frac{1}{2}c\varepsilon_0 n|A(t)|^2 \tag{2.28}$$

Integrating $I(t)$ over time yields the total energy delivered per unit area per pulse (energy density per pulse), which is called the pulse fluence F $[J/m^2]$

$$F = \int_{-\infty}^{\infty} dt I(t) \tag{2.29}$$

Then by multiplying the fluence by the pulse area and the repetition rate we can calculate the average power in the pulse $P_{ave}[W]$.

$$P_{ave} = \frac{1}{2}F\pi w^2 f_{rep} \tag{2.30}$$

Where w is the Gaussian beam waist.

2.2 Results of the OPA Simulation

Two sequential stages of periodically polled Lithium niobate (PPLN) were simulated in order to predict the performance of the OPA. A drawing of this is shown in figure 2.2. Stage 1 was simulated as a 2 mm thick PPLN crystal, and the

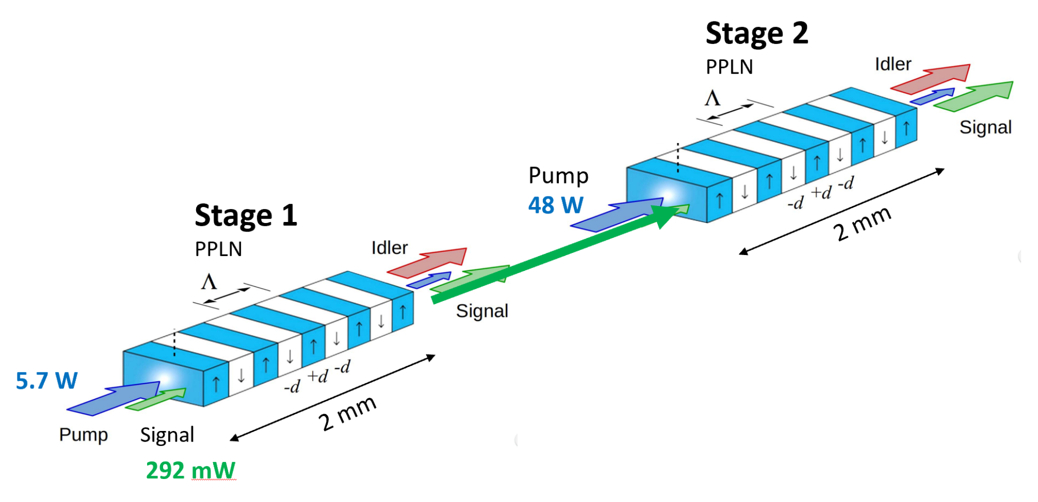

Figure 2.2: Two stages of PPLN were simulated. **Stage 1**, is 2 mm thick, pumped with 5.7 W of 1035 nm (focus waist $w = 67\ \mu m$, $\approx 10\ GW/cm^2$), and seeded with 292 mW of 1550 nm signal (focus waist $w = 60\ \mu m$). After stage 1 the 3 μm idler and the pump is discarded and the amplified signal proceeds to stage 2. **Stage 2**, is 2 mm thick, pumped with 48 W ($w = 137\ \mu m$, $\approx 10\ GW/cm^2$), and seeded with the 1550 nm signal from stage 1 ($w = 137\ \mu m$). This figure is from [49].

input parameters were the following. The signal seed was a Gaussian pulse with a center wavelength of 1.55 μm, 292 mW average power, 100 fs pulse duration, and focused to a spot size of 60 μm. The stage 1 pump was also a Gaussian pulse with a center wavelength of 1.035 μm, 5.7 W average power, 180 fs pulse duration, and 67 μm spot size.

This is followed by stage 2 which was seeded using the signal output of stage 1, and pumped with 48 W, with a focal spot size of 137 μm [2]. The simulation of stage 2 was run for a 2 mm or 1 mm crystal. Both crystals had a polling period of 30.49 μm and were at a temperature of 80 C. In both stages the signal-pump delay

---

[2] These are measured spot sizes at the site of the crystal, and are the result of our best effort to meet the design criteria of 10 GW/cm^2.

was optimized in order to minimize group velocity walk off and thus maximize the power output of the OPA. This optimization was performed in the simulation by scanning the signal-pump time delay parameter until the final idler power was maximized. This is equivalent to scanning the signal-pump delay stage manually in the experiment.

We ran the simulation for a number of different input configurations and I have chosen to present the results from the configuration we finally settled on, which is a 2 mm thick PPLN crystal in both stage 1 and stage 2, and we chose to discard the idler between stage 1 and stage 2. The simulation results indicated that 1.9 W of signal and 0.8 W of idler would be generated in stage 1, and 18.7 W of signal and 8.3 W of idler would be generated in stage 2. The power build up vs. z in both stages of the OPA is shown in figure 2.3

We estimated that approximately 365 nm of idler bandwidth can be supported by a 2 mm thick PPLN crystal according to formula 2.31 from [49].

$$\Delta\nu = \frac{2\sqrt{\ln 2}}{\pi}\sqrt{\frac{\Gamma}{L}}\frac{1}{\left|\frac{1}{v_{gs}} - \frac{1}{v_{gp}}\right|} \tag{2.31}$$

where,

$$\Gamma^2 = \frac{2d_{eff}^2\omega_1\omega_2}{c^3\varepsilon_0 n_1 n_2 n_3}I_3 \tag{2.32}$$

and the pump intensity I_3 was taken to be the damage threshold of the crystal 10 GW/cm^2. For QPM $d_{eff} = 2/\pi\ d_{33}$ where d_{33} is the dielectric tensor element [34]. From this formula, which is plotted in figure 2.4, it is evident that the crystal

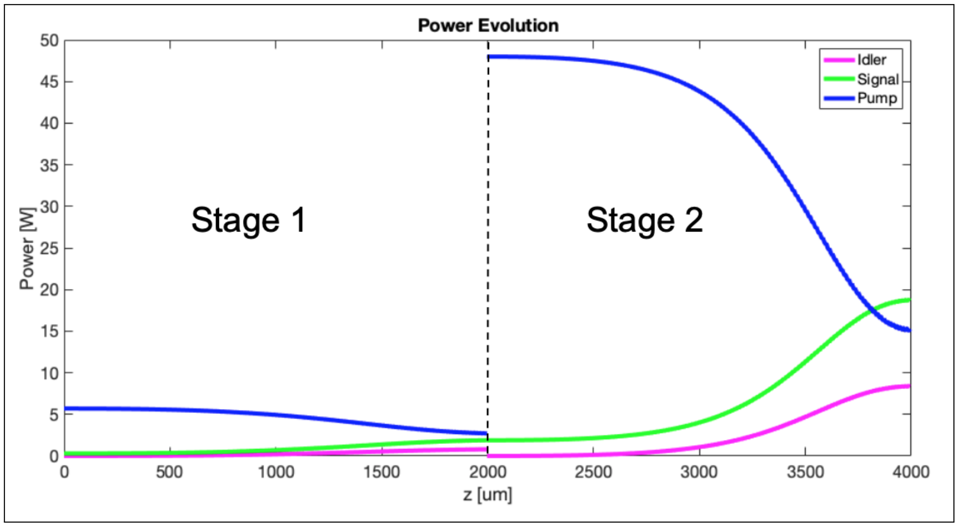

Figure 2.3: Simulation of the power build up in the pump, signal, and idler vs. crystal propagation length z, for stage 1 and stage 2 of the OPA, with 2 mm crystals in both stages. The signal-pump time delay was optimized independently for each stage in order to maximize the idler power output at the end of stage 2. In between stage 1 and stage 2 (dashed line) the idler is dumped and the pump is increased to 48 W.

length and group velocity mismatch (GVM) are the chief limiters of attainable bandwidth. This is why two crystal thicknesses, 1 mm and 2 mm, were considered in order to find a balance between large bandwidth and obtainable power. However, in the end we discovered that the limitation on the idler bandwidth is not due to GVM, but rather caused by the signal seed pulse not entirely temporally overlapped with the pump within the PPLN crystal. Therefore we ultimately decided to use a 2 mm thick crystal in stage 2, which maximized the power output of the OPA.

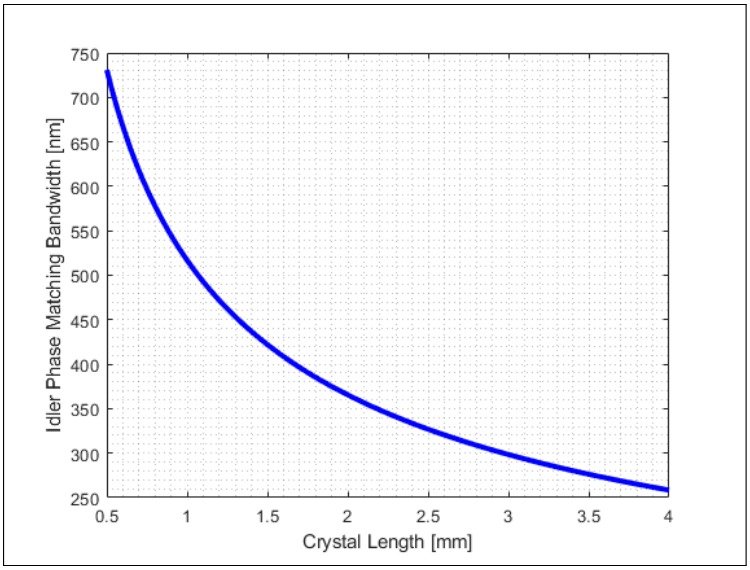

Figure 2.4: Estimated idler phase matching bandwidth vs. crystal length, which indicates that the 2 mm thick crystal can support 365 nm of idler bandwidth.

3. OPA

3.0.1 Design and Performance

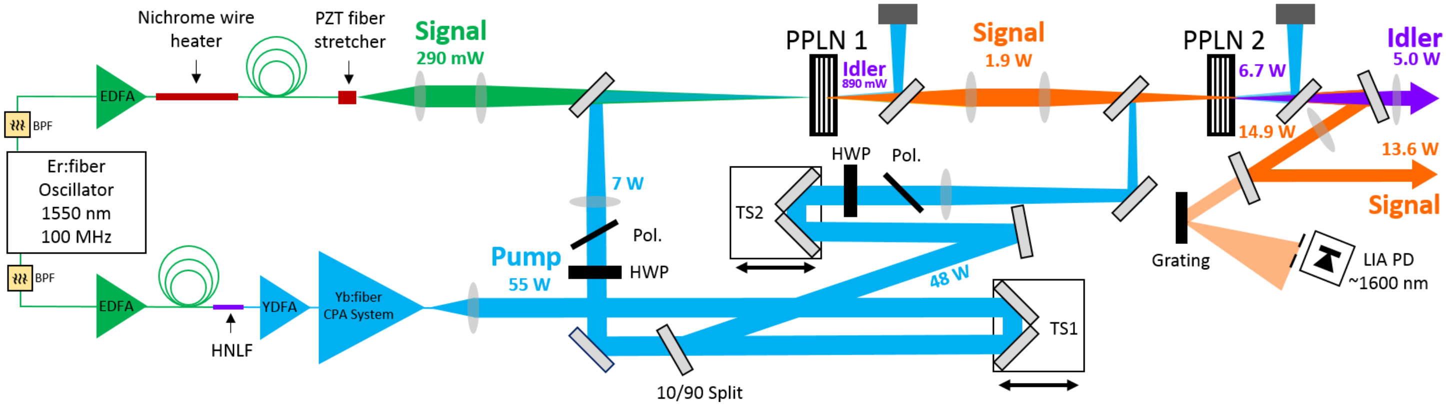

Figure 3.1: Schematic of the two stage OPA. Pump and signal branches are derived from an Er:fiber oscillator are amplified in separate Er:fiber (EDFA) and Yb:fiber (YDFA) amplifiers. Difference frequency generation in two periodically-poled lithium niobate crystals (PPLN1 and PPLN2) generates the high power signal and idler combs. Path-length stabilization is achieved by heating the fiber in the signal branch with a nichrome heater wire. Translation stage TS1 controls the pump/signal delay in both OPA stages, with TS2 changing only stage 2. More details in the text.

In this section, we present a 2.9 μm frequency comb based on high-power DFG in a two-stage OPA, operating at 100 MHz repetition rate with 6.7 W average power and 100 fs pulse duration. To our knowledge, this is the highest power mid-IR optical frequency comb reported to date and among the highest average power ultrafast mid-IR light sources in general. Furthermore, we demonstrate that this OPA can generate sufficient bandwidth to support few-cycle mid-IR pulses with further refinement of the seeding signal branch.

A schematic of our design is shown in figure 3.1. The pump (1035 nm) and signal (1500-1650 nm) are both derived from an all polarization-maintaining (PM) fiber Er:fiber oscillator (Menlo Systems M-comb ultralow noise variant) with a center wavelength of 1560 nm. In addition to convenient pulse synchronization, deriving both pump and signal combs from the same oscillator ensures the idler comb generated via DFG has $f_0 = 0$.

The pump branch uses an intricate yet robust chain of nonlinear fiber optics to shift the Er:fiber comb from 1560 nm to 1035 nm [75]. From the Er:fiber oscillator, the light is bandpass-filtered (10 nm, BPF) and amplified in a nonlinear Erbium-doped fiber amplifier (EDFA) incorporating normal-dispersion Er-doped fiber (1.5 m Er80-4/125-HD-PM, D $\approx$ -22 ps/nm/km, 80 dB/m absorption at 1530 nm) pumped by four 750 mW, 976 nm pump diodes. After a length of the anomalous dispersion fiber after the EDFA (30 cm, D $\approx$ 18 ps/nm/km), sub-50 fs pulses with 350 mW average power enter a 3 cm long piece of anomalous dispersion (D = 5.6 ps/nm/km, $\gamma = 10.5$ W^{-1}km^{-1}, OFS Specialty Photonics) highly nonlinear fiber (HNLF) directly spliced to the anomalous dispersion fiber. Dispersive wave generation in the HNLF gives a comb with $\sim$15 mW of power between 1000 and 1100 nm. All components of this fiber assembly are polarization maintaining (PM) for excellent long-term stability. The output of the HNLF is subsequently amplified to 200 mW in a nonlinear, single-mode fiber, core-pumped, Yb-doped fiber amplifier (YDFA) and stretched to ∼100 ps using an anomalous third-order dispersion fiber stretcher [43]. This light is then used to seed a two stage high-power chirped-pulse YDFA system previously described in [43], giving up to 55 W and 180 fs pulses after grating-pair compression.

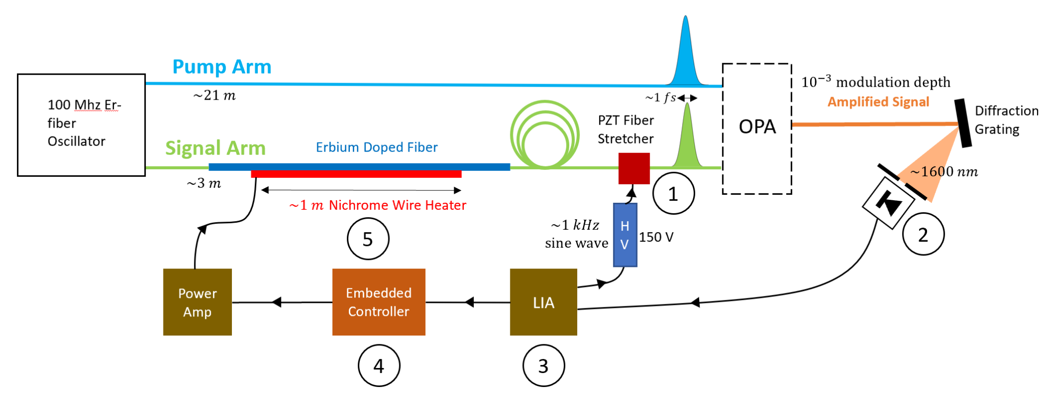

Figure 3.2: OPA path length stabilization mechanism which corrects for the thermal drift in the high power pump arm. **1)** Homemade PZT fiber stretcher, driven by a lock in amplifier (LIA) via a high voltage PZT amplifier, modulates the signal pulse in time a at rate of 1 kHz. **2)** Photodiode detects the power modulation in the amplified signal light. **3)** LIA generates an error signal. **4)** Embedded controller integrates the error signal and sends a control voltage to a power amplifier. **5)** 1 m of Nichrome wire tapped directly to the Erbium doped gain fiber increases the signal delay to compensate for the thermal drift of the pump arm.

The signal branch is comparatively much simpler. A similar nonlinear EDFA is used, but with a longer 75 cm single-mode anomalous-dispersion fiber spliced to its output. This provides 290 mW and the complicated spectrum shown as the green curve of figure 3.3c) for seeding the OPA. The total optical path length difference of ∼20 m between the two branches, with high-power fiber amplifiers in both arms of the interferometer, is subject to long-term thermal drift. To stabilize the delay between the pump and signal at the OPA, the signal branch is equipped with two actuators (figure 3.2). A piezoelectric fiber stretcher, driven with a 1071 Hz 20 V amplitude sine wave, modulates the signal seed delay by approximately 1 fs, which results in 0.1% amplitude modulation on the output of the OPA. This amplitude modulation is detected with a photodiode and a lock-in amplifier (LIA PD) to give an error signal. The error signal is integrated using a micro-controller which controls heating current sent to 1 m of nichrome wire kapton-taped directly to the EDFA gain fiber. A current of $\sim$1 A increases the fiber temperature by approximately 30° C, and gives 1.1 ps of delay. With this setup, the path length can be stabilized indefinitely after an initial warm-up period.

Optical Parametric Amplification is done in two stages using 5%-MgO-doped periodically-poled lithium niobate (PPLN). A 2 mm long PPLN crystal, with a poling period of 30.49 μm, was ultimately chosen for both stages, but we report results with both 1 mm and a 2 mm long crystals for PPLN2. The crystals are heated to 80° C to optimize phase matching and avoid photorefractive damage. Two stages offers several advantages for the high-power OPA. First, as discussed by Arisholm et al. [5], it is generally easier to achieve good beam quality in high-gain OPAs with multiple stages. Second, independent control of the pump/signal delay in each stage (via the translation stages shown in figure 3.1) allows partial compensation of the pump/signal group velocity walk-off in stage 1. The pump power of each OPA stage is independently adjustable using a combination of a half wave plate (HWP) and thin film polarizer (Pol.). With 55 W from the YDFA, up to

7 W and 48 W can be used to pump stages 1 and 2 respectively. The pump light is focused to spot sizes of 78 μm and 161 μm (FWHM) in stage 1 and 2, respectively. The signal beam in each stage is focused to the same size as the pump. We have not observed crystal damage over several months of operation. [1]

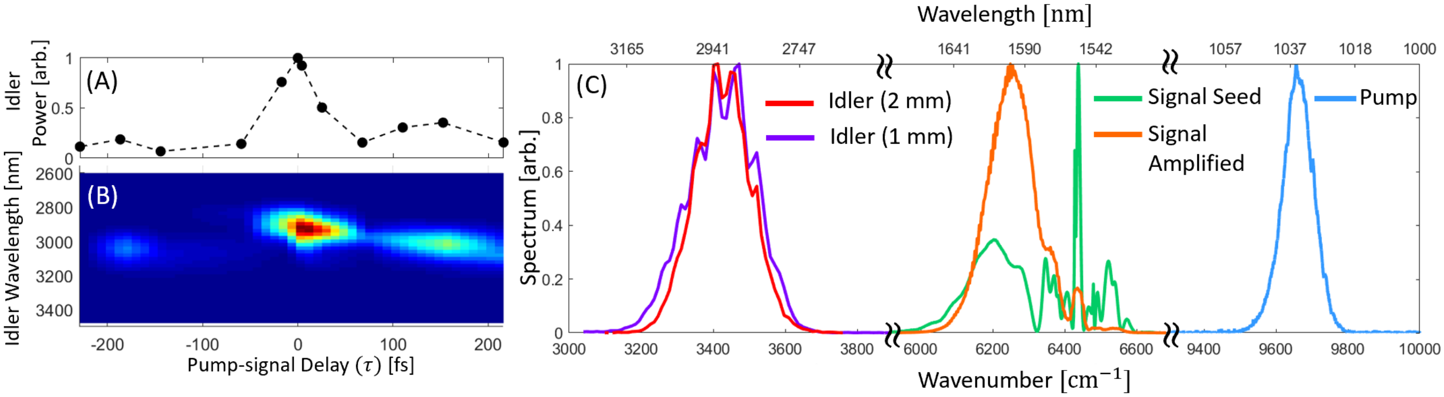

Figure 3.3: a) and b) Normalized stage 2 idler power and idler spectrum vs. pump-signal delay τ. Positive τ indicate that the pump is arriving after the signal. c) Spectrum of the pump, signal seed, signal output, and idler output of the OPA at $\tau = 0$. The two idler spectra shown are for 1 and 2 mm PPLN crystals in stage 2.

Figures 3.3a) and 3.3b) show the OPA output power and idler spectrum as the pump/signal delay, τ, for both OPA stages is varied using translation stage TS1, showing multiple pulses emerging from the anomalous dispersion fiber. $\tau = 0$ is taken to be the delay of highest idler power. Mid-IR spectra were acquired using a scanning 1/3-m Czerny-Turner monochromator and liquid-nitrogen cooled InSb photodetector. The highest output power is observed when the OPA output spectrum is centered at 2900 nm, with the corresponding amplified signal spectrum

---

[1] The reader might notice that the beam sizes here are not exactly the same as reported in the OPA simulation section. This is due to the difference between defining the beam width as FWHM or w ($1/e^2$ radius). The equivalency is $2w = \sqrt{2}/\sqrt{log(2)} * FWHM$ or approximately $FWHM = 1.177w$.

(orange curve of figure 3.3c) centered at 1600 nm. This well isolated pulse at $\tau = 0$, trailing the main 1550 nm pulse at $\tau = -200$ fs corresponds to a Raman-shifted soliton generated in the long anomalous dispersion fiber pigtail of the signal-branch EDFA. Thus, despite the complicated temporal structure emerging from the simple signal branch fiber assembly, clean soliton pulses can be isolated for amplification in the OPA. For the rest of the paper, we present results recorded at $\tau = 0$.

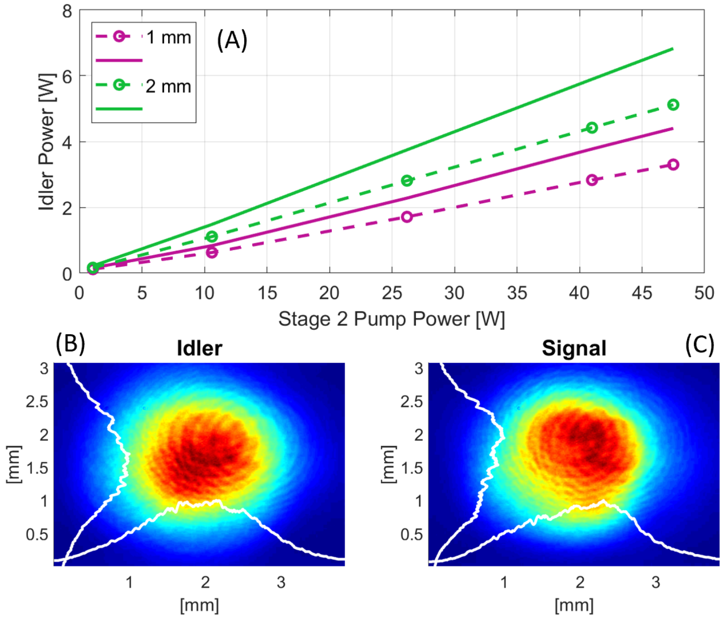

Figure 3.4: a) Stage 2 idler power vs. pump power for both 1 mm and 2 mm long crystals. Dashed lines indicate the measured power after separating and collimating optics. b) Spatial mode profiles of the idler and the signal at full power. Vertical and horizontal profiles along lineouts intersecting the centroid are shown in white.

When pumping the first stage with 7 W, more than 2 W of signal light and 900 mW of idler light emerge from PPLN1. Only the signal is retained between stage 1 and stage 2. With 48 W pump power in stage 2, at the exit of PPLN2 there is 6.7 W of idler and 14.9 W of signal. Figure 3.4a) shows the idler output power vs. stage 2 pump power. Curves are shown for both 1 mm and 2 mm long PPLN crystals. The idler is isolated from the signal and pump via two dichroic mirrors and collimated with an f=25 cm CaF_2 lens. The dashed lines are the measured power after these output optics and represent the usable idler power from the OPA, while the the solid curves represent the output power corrected for the measured 25% losses in the output optics. With the current output optics, the 2 mm (1 mm) long PPLN yields 5 W (3.3 W) usable idler power after the dichroic mirrors. Figure 3.4b) also shows the output spot profiles at high power, measured using an additional 0.5x telescope and a microbolometer array camera. Despite the high powers involved, excellent beam quality is observed in both the signal and idler spatial modes.

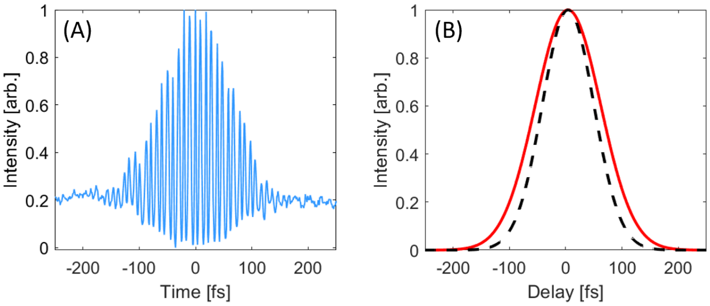

Figure 3.5: a) Idler intereferometric autocorrelation for the PPLN2 = 2 mm thick crystal. b) Intensity autocorrelation from low-pass filtering (red), which assuming a Gaussian pulse shape, corresponds to a measured idler pulse duration of 96 fs. Calculated autocorrelation (black) for a transform limited pulse with the spectrum shown in figure 3.3c).

Figure 5.3a) shows an interferometric autocorrelation of the idler pulse, measured using a Michelson interferometer with a 2-photon InGaAs photodiode detector. Figure 5.3b) shows the intensity autocorrelation obtained from low-pass filtering the data. Assuming a Gaussian pulse shape, the measured idler pulse duration is determined to be 96 fs (FHWM). The transform-limited pulse calculated from the idler spectrum of figure 3.3c) has a FWHM of 78 fs. For comparison with the experimental data, we also calculated the autocorrelation that the transform-limited idler pulses would have produced, and this is shown in dashed black.

Figure 3.6 shows the relative intensity noise (RIN) in units of dBc/Hz for the idler output, signal output, pump, and signal seed, acquired with a multichannel 16-bit digitizer with analog anti-aliasing filters (Picoscope 4262). Analysis of the corresponding time series data indicated that idler and signal noise are strongly correlated, but uncorrelated from the noise of the pump and signal seed. Interestingly, we observed the RIN levels to not depend strongly on the pump/signal delay, in contrast to other recent reports [38, 56].

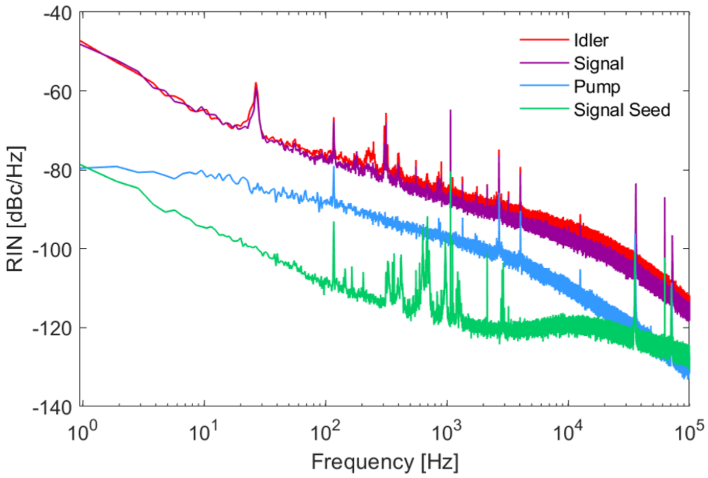

Figure 3.6: RIN for idler, signal output, pump, and signal seed.

Finally, we address the current OPA bandwidth and what is attainable with this platform. Figure 3.3c) shows the idler spectrum for either the 1 and 2 mm PPLN crystals in the second OPA stage. The bandwidth obtained is nearly the same. Similarly, the pulse duration measured with 1 and 2 mm crystals is also the same within experimental error. This indicates that the bandwidth and pulse duration are not limited by the the group velocity walk-off in PPLN2, but instead by the fragmented signal seed pulse. Further evidence that the OPA can support much larger bandwidths is seen in figure 3.3b), where output idler spectra are recorded as the pump/signal delay is varied. Parametric gain is achieved over $\sim$ 400 nm (450 cm^{-1}) of bandwidth with a single poling period and crystal temperature. To further explore this, we modeled the OPA in one spatial dimension as a $\chi^{(2)}$ three-wave mixing of temporally-Gaussian pulses according to [50]. We applied the Fourier split-step method to solve two sequentially and independently pumped stages PPLN, with 25 fs transform-limited input seed pulses and 2 mm PPLN crystals in both stages. The results of the simulation predict that >400 nm phase-matched bandwidths supporting transform-limited pulses of less than 35 fs duration, or less than 3.5 optical cycles, can be attained.

In this section we have presented the design and performance of a high-power mid-IR frequency comb based on difference frequency generation. The system has demonstrated the ability to produce 6.7 W of 2.9 μm idler light and 14.9 W of 1.6 μm signal light with excellent beam quality and measured idler pulse duration of 100 fs. We have also shown that the OPA is capable of supporting larger bandwidths and shorter, even few-cycle pulses, with further refinement of the seed branch. Very short 1550 nm pulses for seeding the OPA can be generated using a similar nonlinear EDFA seed branch by using short normal dispersion HNLFs, as in [71], and we plan to implement this in the future. With few cycle-pulses and intrinsic CEP stability, this source is attractive for driving nonperturbative HHG in solids, with the possibility of generating isolated attosecond VUV pulses at high repetition rate via gating schemes [25]. The high-power signal beam offers additional opportunities. Even with the current usable idler parameters of 5 W of average power and 100 fs pulse duration, focusing to 6 μm (2λ) FWHM would yield peak intensities of 1.6×10^{12} W/cm^2, sufficient to reach the nonperturbative HHG regime in a variety of crystals [25]. We note that solid-state HHG at $\sim$100 MHz rate has recently been achieved using alternative high-power, but not CEP-stable, mid-IR sources [42, 73]. Finally, using this high power DFG comb, we have recently realized cascaded HHG in PPLN waveguides at 100 MHz for the generation of broadband visible frequency combs [37], and in this work we have also verified the coherence of the idler comb via heterodyne characterization of its high harmonics. This OPA platform can also be used for tunable high-power mid-IR comb generation if dispersive-wave generation is implemented in the signal branch and the PPLN poling period tuned as in [50].

4. PPLN Waveguide Experiment

4.1 Introduction

Developing broadband frequency combs, which are robust and fieldable, is important to realizing the numerous applications of comb technology. High harmonic generation (HHG) in periodically polled Lithium Niobate (PPLN) waveguides is one promising means of generating frequency combs which span the spectrum from the MIR to the UV [31]. Lithium Niobate's excellent nonlinear properties are owed to relatively large nonlinear susceptibilities, and further confinement in $\sim 100\ \mu m^2$ waveguides enhances the conversion efficiency to the high harmonics.

However, broadband phase matching is a challenge in Lithium Niobate since the index of refraction varies greatly across the UV-VIS range. A well established practice for phase matching $\chi^{(2)}$ processes (SFG, SHG, DFG) is to flip the d_{eff} vector at a period which has the effect of canceling the wavevector mismatch between the two frequencies (refer to section 2.1 for a detailed discussion of Quasi Phase Matching (QPM)). This principle can be extended to a continuous spectrum of frequencies by chirping the polling period [31, 37] so that all the $\chi^{(2)}$ processes, and all the harmonic central frequencies, are phase matched at some point in the crystal. Because of PPLN's large $\chi^{(2)}$ susceptibility one might expect this leading order of the expansion of the nonlinear polarization to dominate. If this is the predominant HHG mechanism then one would expect the harmonics to be built up from cascaded $\chi^{(2)}$ processes beginning with SHG of ω_0 making $2\omega_0$, then SFG of $2\omega_0$ and ω_0 making $3\omega_0$, and so on and so forth. For a 3 um pump all the possible ways to make harmonics up to the 9^{th} (333 nm) are enumerated in figure 4.1.

However, cascaded $\chi^{(2)}$ processes are not the only physical mechanism known to make harmonics in crystals. Two other pathways which have been offered to explain HHG in crystals stem from perturbative $\chi^{(n>2)}$ and non-perturbative physics [26, 41]. Therefore, in an effort to answer the question "by what mechanism is the light generated in PPLN waveguides?" we offer a comparison of two experiments—Hickstein et al. (4.1 μm pump, 1 MHz rep rate, $<$ 25 nJ pulse energy) [31], and our own (3 μm pump, 100 MHz rep rate, $<$ 12 nJ pulse energy)—to a simulation which solves the broadband nonlinear envelope equation for optical pulses in $\chi^{(2)}$ media [19]. Understanding the harmonic generating mechanism in chirped PPLN waveguides can illuminate pathways for optimizing these waveguides in the future.

We find, in the case of the 4.1 um experiment, cascaded $\chi^{(2)}$ processes explain the experimental spectrum—showing good qualitative agreement, and predominately quantitative agreement in harmonic conversion efficiency and power

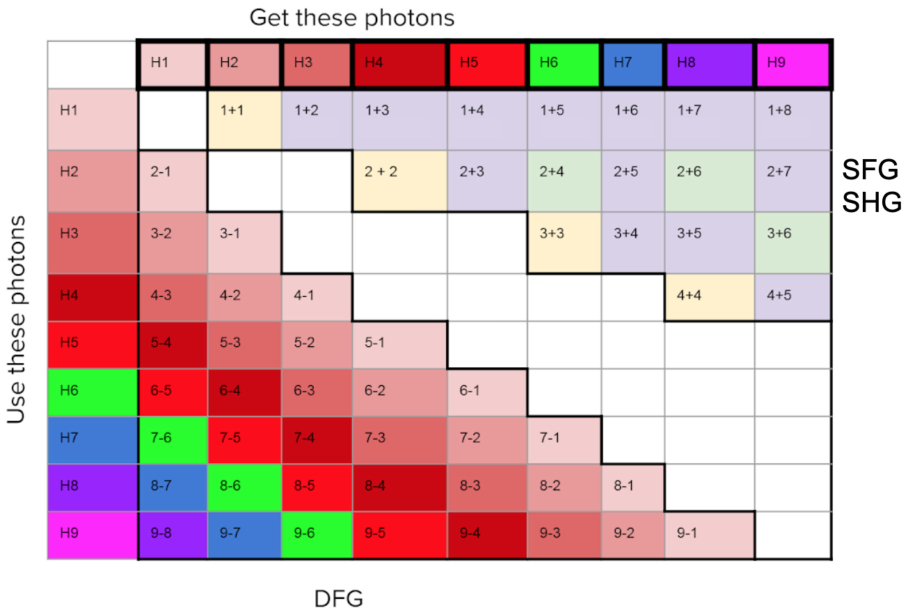

	H1	H2	H3	H4	H5	H6	H7	H8	H9
H1		1+1	1+2	1+3	1+4	1+5	1+6	1+7	1+8
H2	2-1			2 + 2	2+3	2+4	2+5	2+6	2+7
H3	3-2	3-1				3+3	3+4	3+5	3+6
H4	4-3	4-2	4-1					4+4	4+5
H5	5-4	5-3	5-2	5-1					
H6	6-5	6-4	6-3	6-2	6-1				
H7	7-6	7-5	7-4	7-3	7-2	7-1			
H8	8-7	8-6	8-5	8-4	8-3	8-2	8-1		
H9	9-8	9-7	9-6	9-5	9-4	9-3	9-2	9-1	

Figure 4.1: Enumeration of the cascaded $\chi^{(2)}$ effects which illustrate the possible harmonic pathways we are hypothesising dominate HHG in PPLN waveguides.

scaling in the low and high pump power limits, and saturation of the harmonics. The 3 um experiment also shows consistency with a cascaded $\chi^{(2)}$ model, however there remains a discrepancy in the conversion efficiency to the high harmonics.

4.2 Experiment

Figure 4.2 shows the setup for the PPLN waveguide experiment. The elements are a home-built high power mid-infrared OPA frequency comb pump (see section 3), 5 PPLN waveguides with varying chirp profiles, and a scanning monochromator to spectrally resolve the output light. The OPA DFG's 1035 and 1550 nm light in 2 stages of PPLN, and is capable of generating 6.7 W of 3000

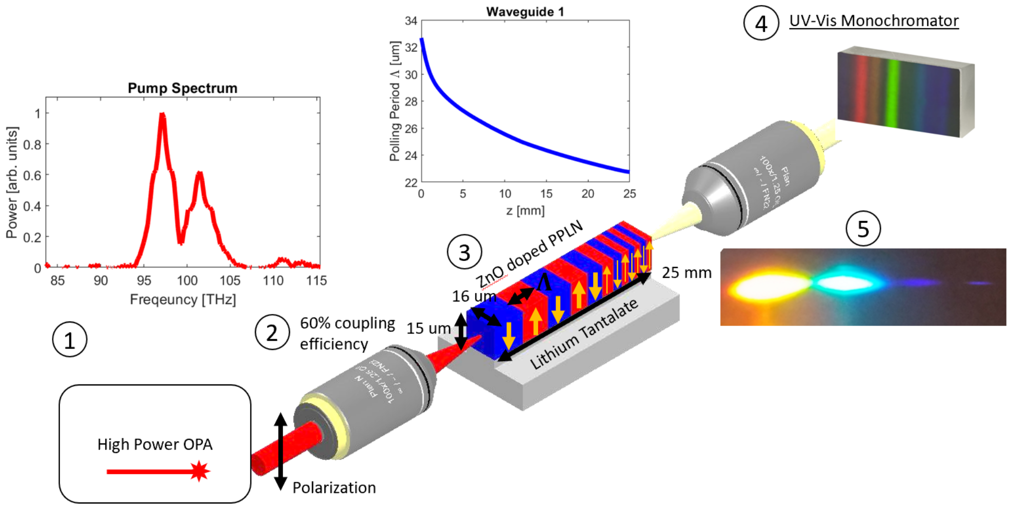

Figure 4.2: 1. High Power OPA is used to pump the waveguide at up to 1.2 W (12 nJ). 2. Microscope objective was used to couple into the waveguide with 60% efficiency. 3. Periodically polled Lithium Niobate waveguide (PPLN), with a chirped polling period, on top of a Lithium Tantalate substrate. UV-VIS Monochromator calibrated to absolute power. 5. White light from the waveguide sent through a prism and onto a screen makes the harmonics clearly visible.

nm light at a repetition rate of 100 MHz with 100 fs pulse duration. The pump is coupled into the waveguide via a chalcogenide (industry name Black Diamond) microscope objective. Due to losses in the optics form the OPA to the waveguide the maximum power that could be coupled into the waveguide is 1.2 W (12 nJ pulse energy) [1]. The waveguides are manufactured by NTT Electronics America from ZnO doped Lithium Niobate, are approximately square 15 x 16 μm x 25 mm long, and are ridged atop Lithium Tantalate. The ZnO provides a resistance to photorefractive damage [53]. Five waveguides were tested with up-chirp polling

---

[1] 1.2 W was figured by measuring 2 W before the waveguide coupling optics and then assuming a 60% coupling efficiency. 60% coupling efficiency measured by the transmitted power through the waveguide at low power. Since the beam quality remains good at high power, it's reasonable to assume the coupling efficiency at low power can be extrapolated to high power.

(decreasing period) in the "forward" direction, and their profiles are given in figure 4.17 in the methods section of this report. The polarization of the incident light was set to vertical to be along the extraordinary axes of the crystal, this gave a $d_{eff} = 19.6$ pm/V. The output light of the waveguide was spectrally resolved using a McPherson 0.3 m, Czerny–Turner style, UV-VIS monochromator with a UV enhanced Aluminium grating blazed for 300 nm. The monochromator was actuated via a stepper motor with a microcontroller, and the wavelength axis was calibrated using the spectral lines from a Mercury lamp. The detector is a silicon photodiode (adequate, but not ideal, for 9th harmonic at 333 nm) which is amplified via a Stanford Research Systems (SRS) transimpedance amplifier. Typical photocurrents were in the range of 500 nA. The response vs. wavelength of the entire system was calibrated using the broadband spectrum from a Xenon-Meurucry lamp, and the dynamic range of the systems was determined to be 23 dB. The absolute response was calibrated by comparing the integrated power in the 6^{th} harmonic to a power meter measurement of the absolute power in the 6^{th} harmonic spectrally filtered using a prism.

4.3 Results

We measured the spectrum from each of the five waveguides when pumped with 1200 mW (12 nJ pulse energy) in the forwards direction for waveguides 1, 2, 4 and 5, and backwards for waveguide 3. We also did a power scan of waveguide 5, and recorded the spectrum at various powers ranging from 1.8 mW to 12 mW.

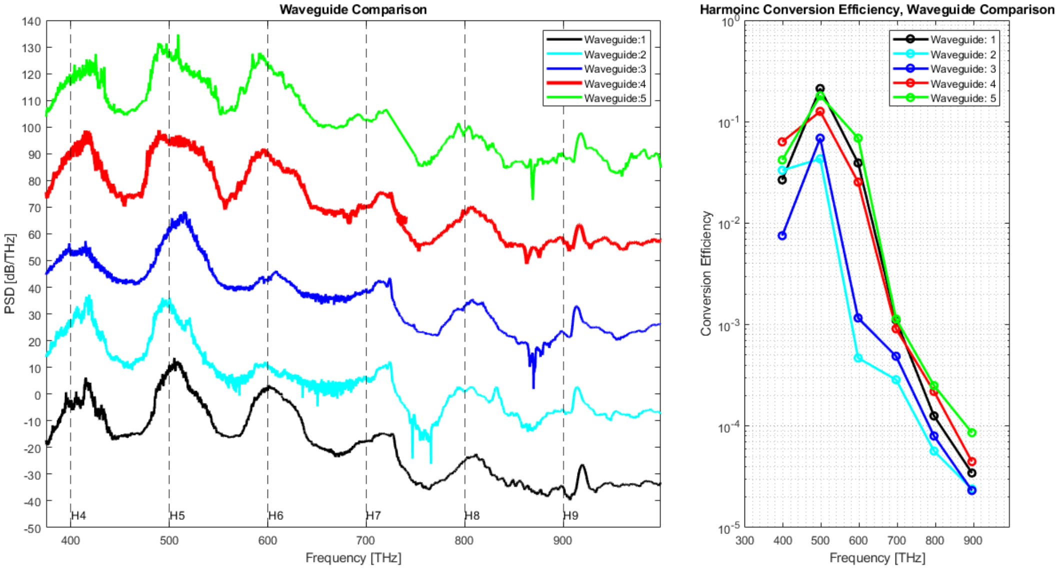

Figure 4.3: Power spectral density vs. frequency comparison between all five of the waveguides when pumped at 1200 mW. All waveguides were pumped in the forward direction (decreasing polling period) except for waveguide 3 which was pumped backwards (increasing polling period). Each spectrum has been separated by 15 dB for clarity. Conversion efficiency to the harmonics vs. frequency with the dots giving the integrated power in the harmonics which has been normalized by dividing by the pump power.

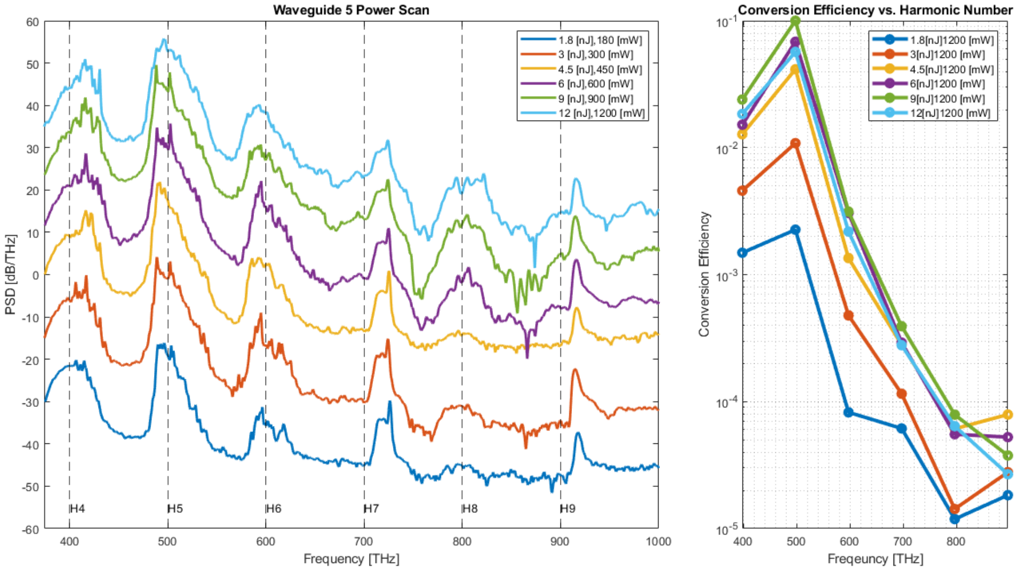

Figure 4.4: Waveguide 5 power spectral density vs. frequency, conditioned on 6 pumping powers ranging from 180 mW to 1200 mW. Each spectrum has been separated vertically by 20 dB for clarity. Conversion efficiency as a function of frequency is shown for the harmonics

The results are shown in figures 4.3 and 4.4 respectively. For specific details about the calibration of the measurement apparatus refer to the methods section. In both cases approximately 23% total conversion efficiency to the harmonics was achieved. We measured this power by using a fused silica window (with approximately 2 μm cutoff) to filter out the 3 μm pump light. In the waveguide scan (figure 4.3) it would appear that there is little variation between waveguides, with the exception of the reduced amplitudes of harmonics 6 and 7 in waveguide 2 and 3. The similarity between the spectra recorded when pumping the waveguides in the forward direction is consistent with the results from Hickstein et al. [31], where it was observed that only in the backwards pumping direction the waveguides showed a prominent difference. The cause of the missing harmonics 6 and 7 remains unknown. Perhaps a more detailed harmonic pathway analysis than what is covered in this thesis could track down the source of the missing harmonics.

The power scan of waveguide 5 is shown in figure 4.4 for power levels from 180 mW to 1200 mW. Each spectrum has been separated vertically by 20 dB for clarity. The spectral line shapes show some difference between high and low power scans, and this is confirmed by the conversion efficiencies plot. Specifically, the odd harmonics are more pronounced at low power, and the even harmonics fill in as the power is increased. Furthermore, as the power is increased, the harmonics appear to broaden and fill in, and harmonic 5 shows significant enhancement over the other harmonics.

4.3.1 $4.1\mu m$ Pump Experiment Analysis

We simulated $\chi^{(2)}$ interactions using the broadband nonlinear envelope equation in quadratic media given in [19]. A detailed discussion of this is given at the end of this section. The input to the simulation is the transform limited 3 μm pump, or a 200 fs sech^2 pulse in the case of the 4100 nm simulation. The dispersion curve was calculated via COMSOL [52], which shows small variation from bulk PPLN in the IR due to waveguide dispersion, and the UV and IR absorption of Lithium Niobate was added. The nonlinear scale terms were calculated using the material properties of Lithium Niobate. The simulation was run at various pulse energies for all five waveguides and in both waveguide directions. Additionally, simulations were run to explore the effect of removing $\chi^{(3)}$ from the model, and varying the chirp of the input pulse. In order to account for uncertainty in the nonlinear scale factors, all the comparisons between the simulation and experiment have been normalized to focus on the relevant physical parameter—conversion efficiency. For a more a more rigorous justification concerning why it is important to compare conversion efficiencies see the methods section at the end of this chapter.

This discussion will begin with a comparison of the simulation to the Hickstein experiment, which pumped waveguides 1-3 at 4100 nm, 1 MHz, and 25 nJ max pulse energy. Figure 4.5 overlays two experimental waveguide 2 spectra (forward polling direction) pumped at high power (25 mW, 25 nJ pulse energy) and low power (5 mW, 5 nJ pulse energy), overlaid with their respective simulation runs nearest the conversion efficiency observed in the experiment. The y-axis has been

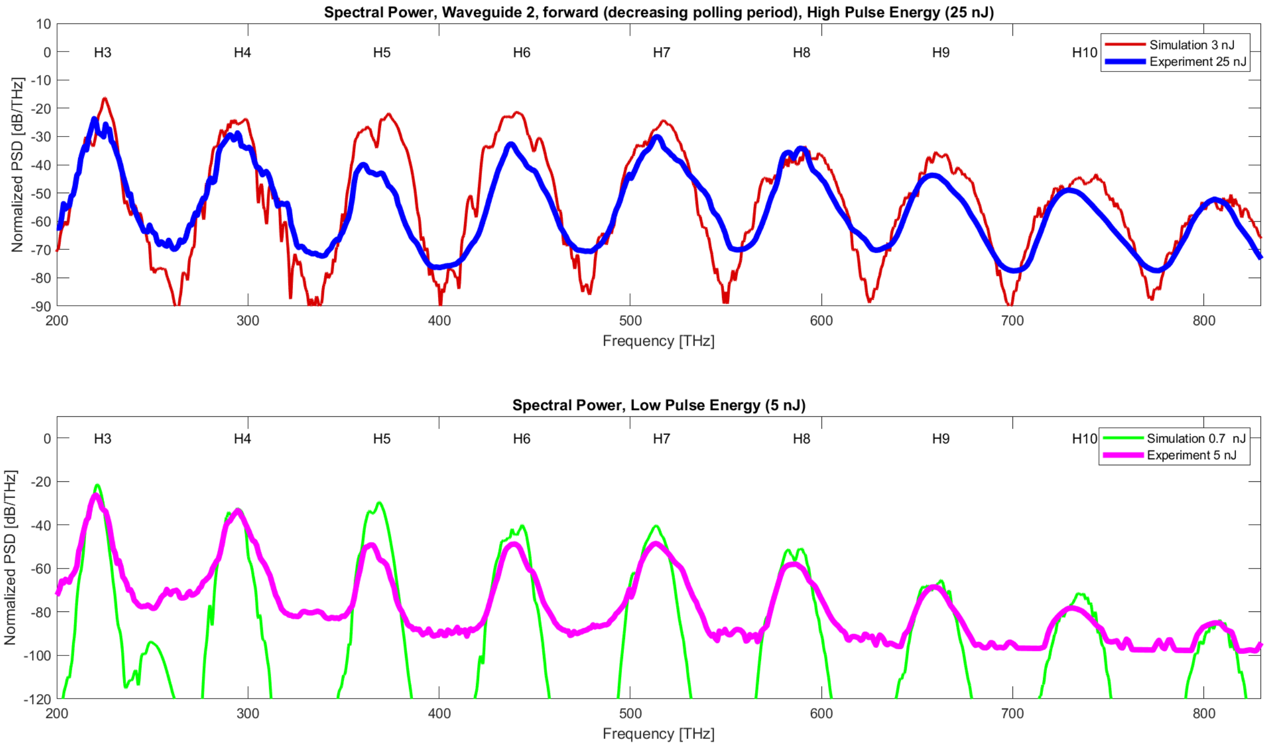

Figure 4.5: Plots of normalized power spectral density (PSD) comparing the 4100 nm experimental spectrum, from waveguide 2 (forward polling direction), recorded by Hickstein et al. at two pulse energies—25 nJ (upper) and 5 nJ (lower)—vs. our simulation. The y-axis was normalized by dividing by the input pump peak power, therefore the plot shows harmonic conversion efficiency. The simulation pulse energy was chosen to be closest to the experimental conversion efficiency.

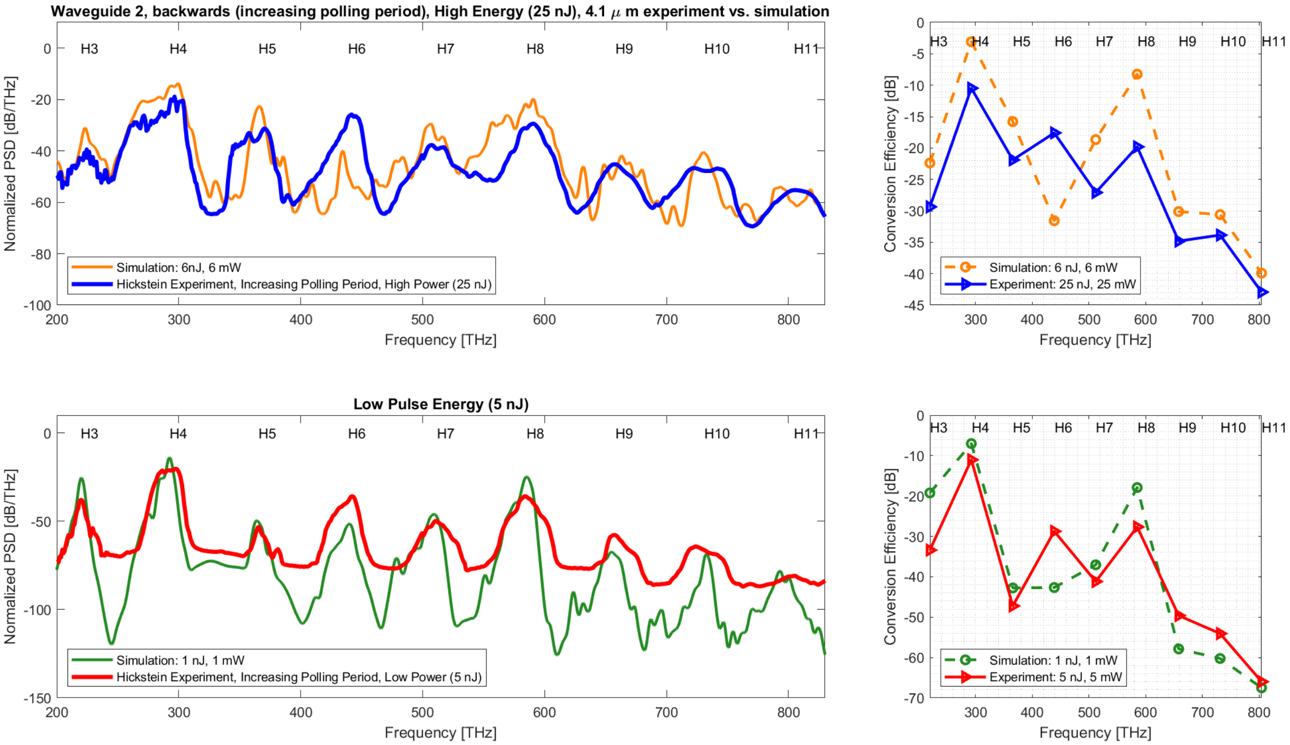

Waveguide 2, backwards (increasing polling period), High Energy (25 nJ), 4.1 μ m experiment vs. simulation

Low Pulse Energy (5 nJ)

Figure 4.6: Comparison between the 4100 nm experiment performed by Hickstein et al. and the simulation for waveguide 2 in the backward polling configuration. The normalization of the y-axis was performed in the same way as in figure 4.5. Evidently pumping waveguide 2 in the backward direction results in a dramatically different spectrum than the forward direction, which was shown in figure 4.5 The cascaded $\chi^{(2)}$ model shows agreement with the features of the experimental spectrum. The conversion efficiency plots show a discrepancy between the simulation and experiment most prominently for harmonic 6.

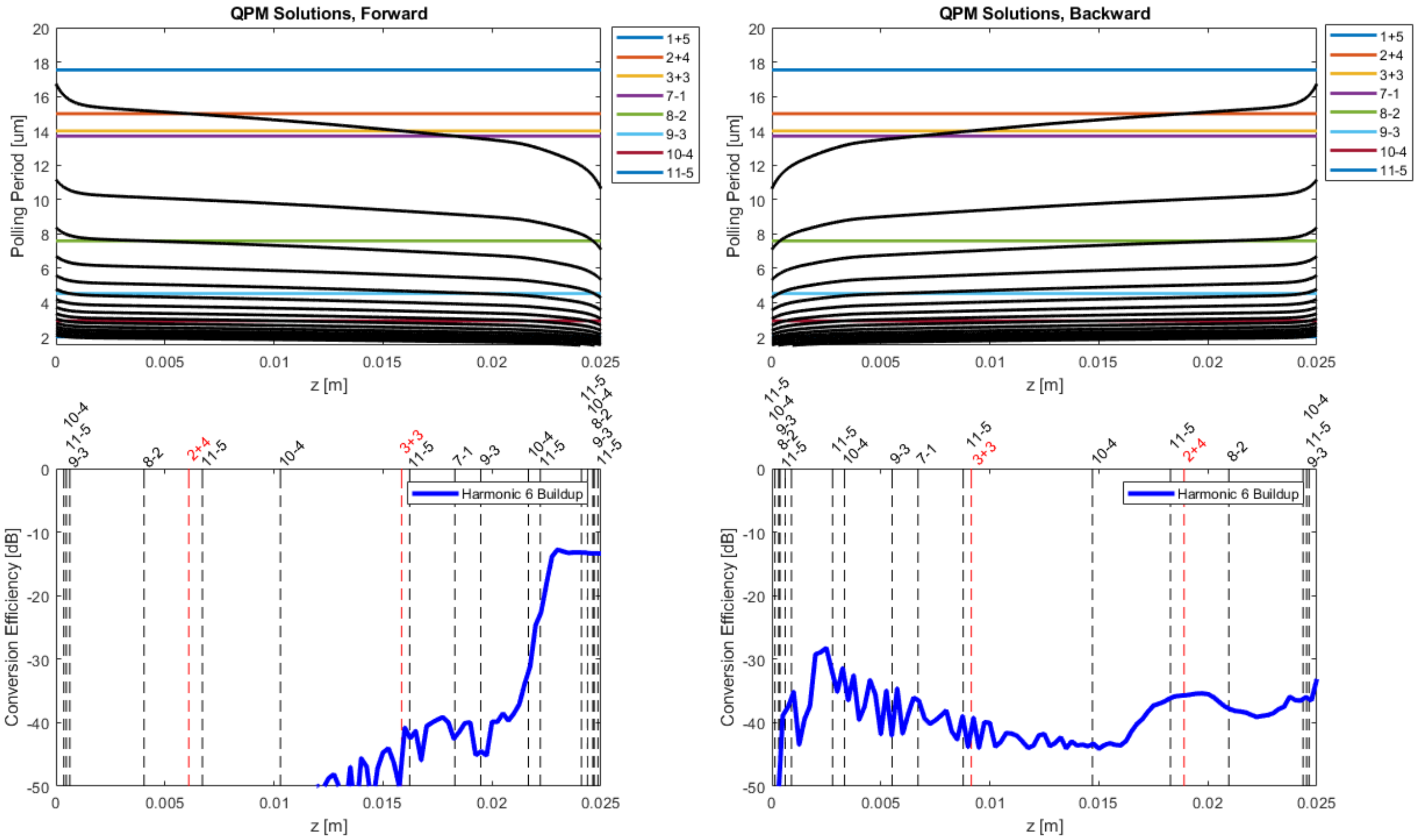

Figure 4.7: Waveguide 2, 4100 nm simulation, exploration into the harmonic 6 pathways. The top plots show the higher orders of the waveguide 2 polling period vs propagation axis z, in the forwards and backwards direction (bold black), with the phase matching polling periods for DFG and SFG which generate harmonic 6, overlaid (colored horizontal lines). The bottom plots show the normalized integrated power in harmonic 6 vs. z, and the vertical dashed lines show the locations of the phase matching solutions (SFG (red), and DFG (black)). There are locations where we would expect there to be buildup in harmonic 6.

normalized by dividing by the input pump peak power (i.e. the input fundamental peak value would be "0" on this plot), therefore the spectra show conversion efficiency to each harmonic. This normalization is necessary to directly compare the simulation to the experiment. It is apparent that there is good qualitative agreement between the simulation and the experiment. In both the high and low power limits, the simulated spectra follow the smooth experimental spectrum of even and odd harmonics, showing similar buildups and peaks and valleys of harmonics. The fact that it is possible to generate a smooth, and relatively flat (i.e. not "jagged"), harmonic spectra with a cascaded $\chi^{(2)}$ mechanism is contrary to the suggestion made in Hickstein et al. They argue that a smooth spectrum, of even and odd harmonics is indicative of a phase-mismatched perturbative $\chi^{(n>2)}$ generating mechanism, which has been shown to be numerically consistent with the observed HHG spectra from ZnO and ZnSe. The conversion efficiency to harmonics 5 and 6 are enhanced in the simulation relative to the experiment. While the source of this is unknown, a possible explanation could be the chirp of the input pulse. The sensitivity of simulation runs to spectral phase suggest the experiment is dependent upon the exact chirp of the pump. We did attempt to explore this parameter by applying the spectral phase which would be accumulated by an initially unchirped pulse propagating though 3 mm CaF2 and 1 mm Black Diamond ($-726\ fs^2$ total). However, the chirp accumulated by these optics alone could not explain the source of the discrepancy.

The argument that our cascaded $\chi^{(2)}$ model qualitatively matches the experiment is made stronger when one compares the waveguide 2 forward polling

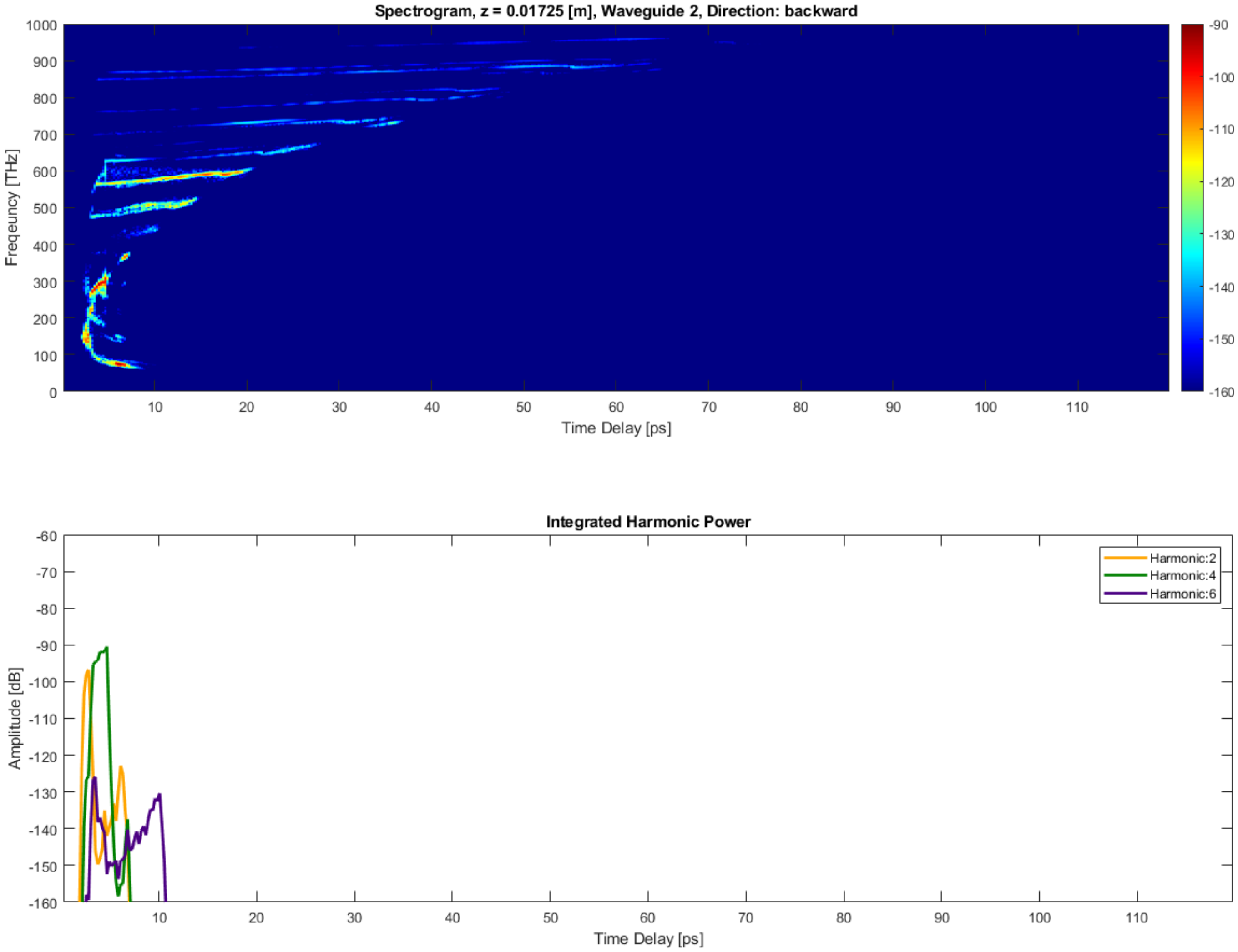

Figure 4.8: Frequency vs. time delay spectrogram of the 4100 nm experiment, waveguide 2 backwards direction, in a reference from moving at the group velocity of the pump, and taken at $z = 17.25\ mm$. Positive time delays indicate events which happened in the past. The entire frame is moving to the left in the window at the group velocity of the pump. The bottom plot shows the harmonic power in dB vs. time for the SFG of harmonics $2+4=6$, and was constructed by integrating the spectrogram. A clear spike is evident in harmonic 6 where harmonics 2 and 4 overlap in time.

direction to the backwards pumped direction (figure 4.6). The backwards pumped waveguide spectrum shows an enhancement of the even harmonics when compared to the smooth spectrum of even and odd harmonics, which was observed in the forwards pumping direction. The simulation captures this change well. However, the integrated conversion efficiency plots indicate that in both pumping power regimes (enhanced at high pump power) the simulation over overestimates the conversion efficiency to harmonics 8, and underestimates harmonic 6.

It is interesting to examine the curious case of harmonic 6. One could ask the following question, why does QPM cause a dramatic difference in the conversion efficiency of harmonic 6, simply from flipping the waveguide direction? One might expect the harmonic buildups in the forwards and backwards waveguide direction to be a mirror images of one another, and ultimately resulting in the same power in harmonic 6 by the end of the waveguide. Understanding the answer to this requires correlating the buildup of harmonic 6 to the phase matching of SFG and DFG processes which generate it. Figure 4.7 (top plots) show the higher orders of the polling period profile vs. the crystal propagation length z, in both the forwards and backwards orientation. Horizontal lines indicate the polling period at which the SFG and DFG processes are phase matched. In other words, the horizontal lines are the values of the polling period Λ which solve $\Delta k = k_1 + k_2 - k_3 + n2\pi/\Lambda = 0$ (SFG) and $\Delta k = k_3 - k_2 - k_1 + n2\pi/\Lambda = 0$ (DFG). Where n is an integer indicating the polling period order. The intersections between the horizontal lines and the waveguide polling profile are locations in z where that process is phase matched. These intersections are projected on the bottom plots and shown as vertical dashed lines. They have been labeled with their process, and color coded according to DFG (black) and SFG (red). Overlaid is the integrated power in harmonic 6 (normalized to the initial pump).

It's immediately clear that the buildup of harmonic 6 in the forward vs backward waveguide direction are not mirror images of each other. In the forward waveguide direction harmonic 6 blows up by 30 dB in the last 5 mm of the crystal, while in backward direction harmonic 6 builds up at first and then trades its energy to the other harmonics in the middle of the crystal, and then builds up again at the end. The phase matching solutions show that there are many more DFG pathways to make harmonic 6 than SFG, but in order for these DFG pathways to contribute there must be adequate power in the higher harmonics. Because the majority of the DFG solutions occur late in forward waveguide direction, there is adequate propagation for the higher harmonics to build up power, and thus when the DFG processes are phase matched at the end of the crystal the buildup of harmonic 6 is dramatic. Compare this to the backward waveguide direction which shows mediocre buildup of harmonic 6 at the start of the crystal because the power in the higher harmonics is low. Consequently, any power which has build up in 6 is traded back to the other harmonics midway thorough the crystal and finally toward the end harmonic 6 gets a big boost from the SFG of harmonics 2+4.

There is another key element which must be considered, the temporal overlap of the harmonics at the location where the process are phase matched. Let's start with the backwards waveguide direction case, and consider the location in z where SFG of harmonic's 2+4 are phase matched. Obviously 2 and 4 will only

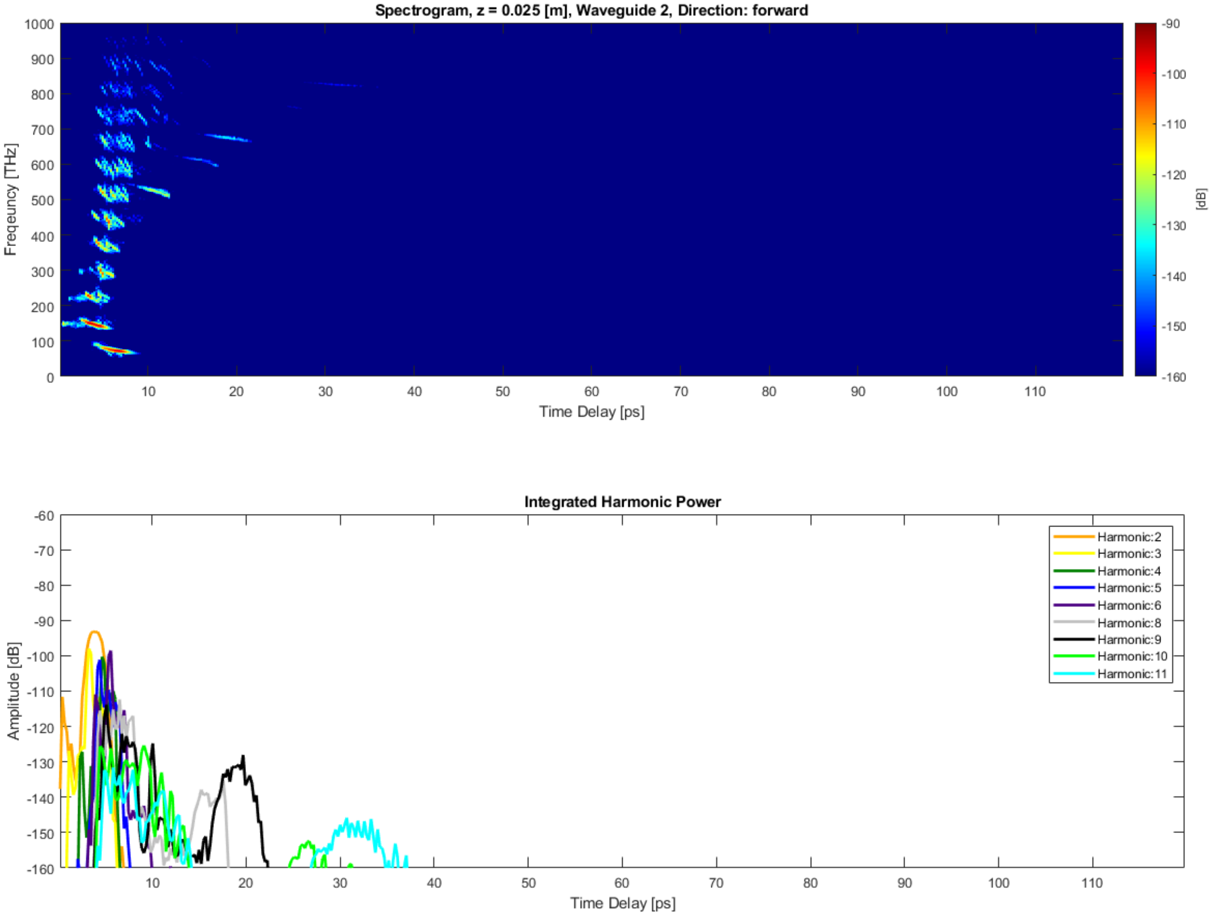

Figure 4.9: Frequency vs. time delay spectrogram of the 4100 nm experiment, waveguide 2 forwards direction, at $z = 25\ mm$. In this case the majority of the power in the harmonics is generated at the end of the waveguide. Using this fact, combined with the knowledge that only DFG processes are phase matched at the end of the waveguide (figure 4.7) we can infer that in the forward polling direction harmonic 6 is generated via DFG.

SFG to 6 when they're temporally overlapped. In order to investigate the time domain picture we construct a spectrogram which plots frequency vs. time delay, and shows the temporal delay between the harmonics at a location in $z \approx 18$ *mm* (which I chose by noting the z location where 2+4 were phase matched in figure 4.7). The spectrogram was constructed by Short-time Fourier transform (STFT) filtering with a Blackman-Harris windowing function (500 fs window) which gives approximately 100 dB of dynamic range. The spectrogram and the integrated harmonic powers are plotted in figure 4.8. The time axis can be interpreted as positive delay are in the past, and all the harmonics are moving to the left in the frame at the group velocity of the fundamental. Examining the integrated harmonic power, we notice that there is a spike in buildup of harmonic 6 (purple curve) right where there is the strongest overlap between harmonics 2 and 4. This is expected. The same logic can be applied to the forward propagation direction, which is shown in figure 4.9. In this case I chose to show the spectrogram at the end of the crystal ($z = 25$ *mm*) because this is where the strongest buildup in harmonic 6 occurs. From the integrated harmonic power plot we notice that the majority of the power in all the harmonics is generated at the end of the crystal, which means they don't have time to walk off because of group velocity mismatch. Hence they're temporally overlapped, and simultaneously phase matched for DFG, resulting in the expected buildup of harmonic 6 at the end of the crystal.

With an interest in designing a waveguide in mind, we can think about what feature in the polling profile leads to strong buildups of the harmonics. What the "curious case of harmonic 6" suggests is that it's the "hook" in the waveguide polling (i.e. where the polling period varies rapidly, like at the end of waveguide 2, forward direction), which generates all the harmonics at once. And that would make sense, because the rapid variation in the polling means more SFG and DFG processes are phase matched within the temporal overlap window, before group velocity walk off separates the harmonics in time.

While one could proceed with the pathway analysis, and granted there is some physical intuition to be gained, there is not always a clear way to decouple the simulation into individual harmonic pathways. Therefore, the focus of this analysis will return to macroscopically comparing the simulation to the 4100 nm pump experiment and then the 3000 nm pump experiment. In figures 4.5 and 4.6 I chose to overlay the 4100 nm experiment with the simulation run which most closely matched the harmonic conversion efficiency. However, there are many level curves corresponding to all combinations of simulation and experimental pump powers and it's potentially interesting to look for trends. Figure 4.10 shows the conversion efficiency to harmonics 3 – 11, for experimental pump powers ranging from 0.4 mW to 22 mW, with simulations (dashed lines) ranging from 0.1 mW to 14 mW overlaid. We observe the simulation conversion efficiencies match some of the experimental harmonics, but not all simultaneously. Specifically, the simulation and experiment agree best for harmonics 3, 5, 7, 9 (odd), than for the even harmonics. For the even harmonics, the simulation conversion efficiencies are slightly high for harmonic 4 and extremely high for harmonic 8, and extremely low for harmonic 6. Furthermore, the experiment shows an enhancement of the even harmonics at low power, but this tends to wash out at high power. The simulation does not capture this washing out feature and still shows an enhancement of harmonic 4 and harmonic 8, and a reduction in harmonic 6 even at high pump powers.

Another way to view the parameter space is to project the conversion efficiency of each harmonic onto the pump-power axis. Figure 4.11 plots the experiment vs. simulation conversion efficiency to harmonics 3 - 11 as a function of pump power. The simulation had to be run with lower pump powers in order to match the conversion efficiency of the experiment. Therefore, to compare simulation to experiment on the same power axis (x-axis) the simulated pump powers need to be scaled up. In this case we scaled the simulated pump power up to a $P_{sim}^{equiv} = 2.0P_{sim}$ (i.e. x-axis transform) and then calculated the conversion efficiency according to the formula P_{harm}/P_{sim}^{equiv} (y-axis transform). The scale factor was determined to be 2.0 by optimizing the numeric agreement between the experimental and simulation slopes in the low pump power regime. This is the metric that I chose to optimize. For a justification of this scaling see the methods section at the end of this chapter.

We observe agreement between the slopes of the simulation curves and the experimental data in the low pumping power regime for harmonics 3, 4, 5, 7, 8, 9, and 11. But harmonics 6 and 10 have a Camel back feature, which steepens the local power scaling law, and diverge from the simulation. The slope of the experiment data is shown as dashed lines. In the high pumping power limits harmonics 3, 4, 5, 7, 8, 9, and 10 show consistent power scaling slopes with the simulation. Harmonics 4, 5, 7, 9, 10, and 11 show consistent saturation profiles, while harmonics 6 is predicted to be an order of magnitude lower by

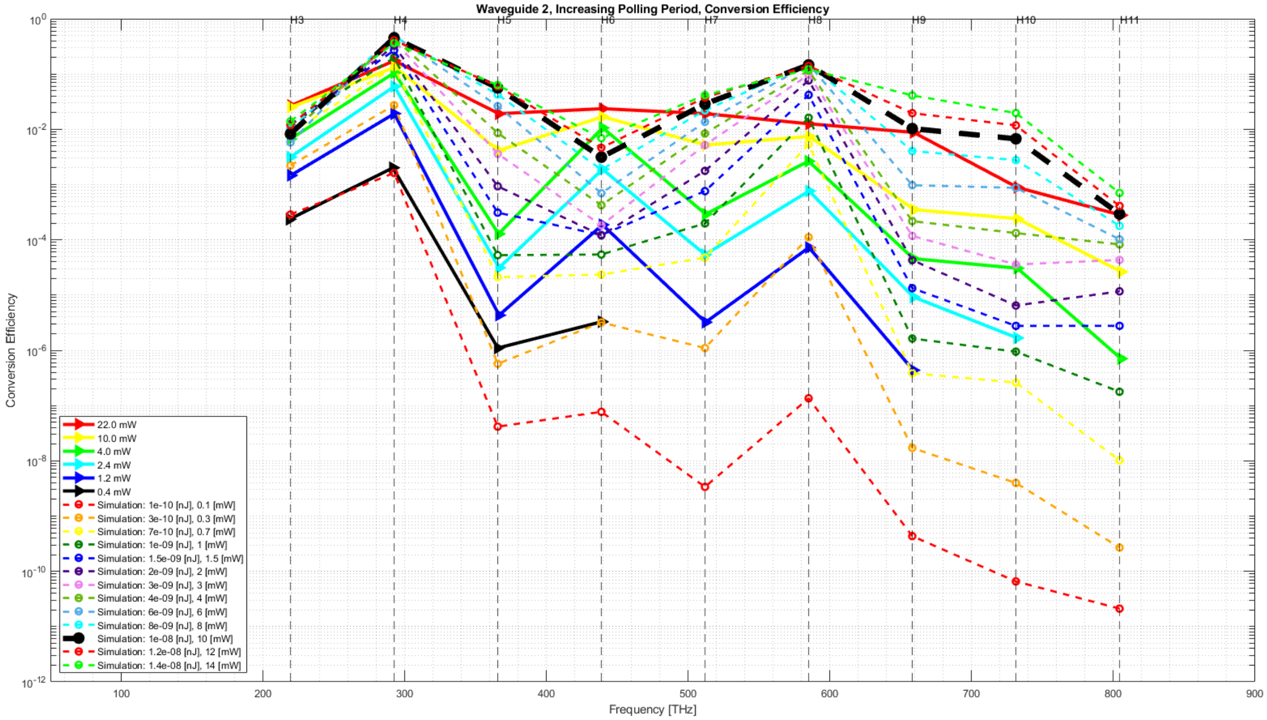

Figure 4.10: 4.1 μm conversion efficiency to harmonics 3 – 11 vs. frequency for waveguide 2, backwards polling direction. The experimental power scans are shown in solid lines and range from 0.4 mW to 22 mW of coupled pump power and were taken from [31]. Overlaid (dashed) are simulations which range in power from 0.1 mW to 14 mW. The bold black simulation curve at 10 mW is meant to show that this power gives approximately the same conversion efficiency as 22 mW of experiment pump power.

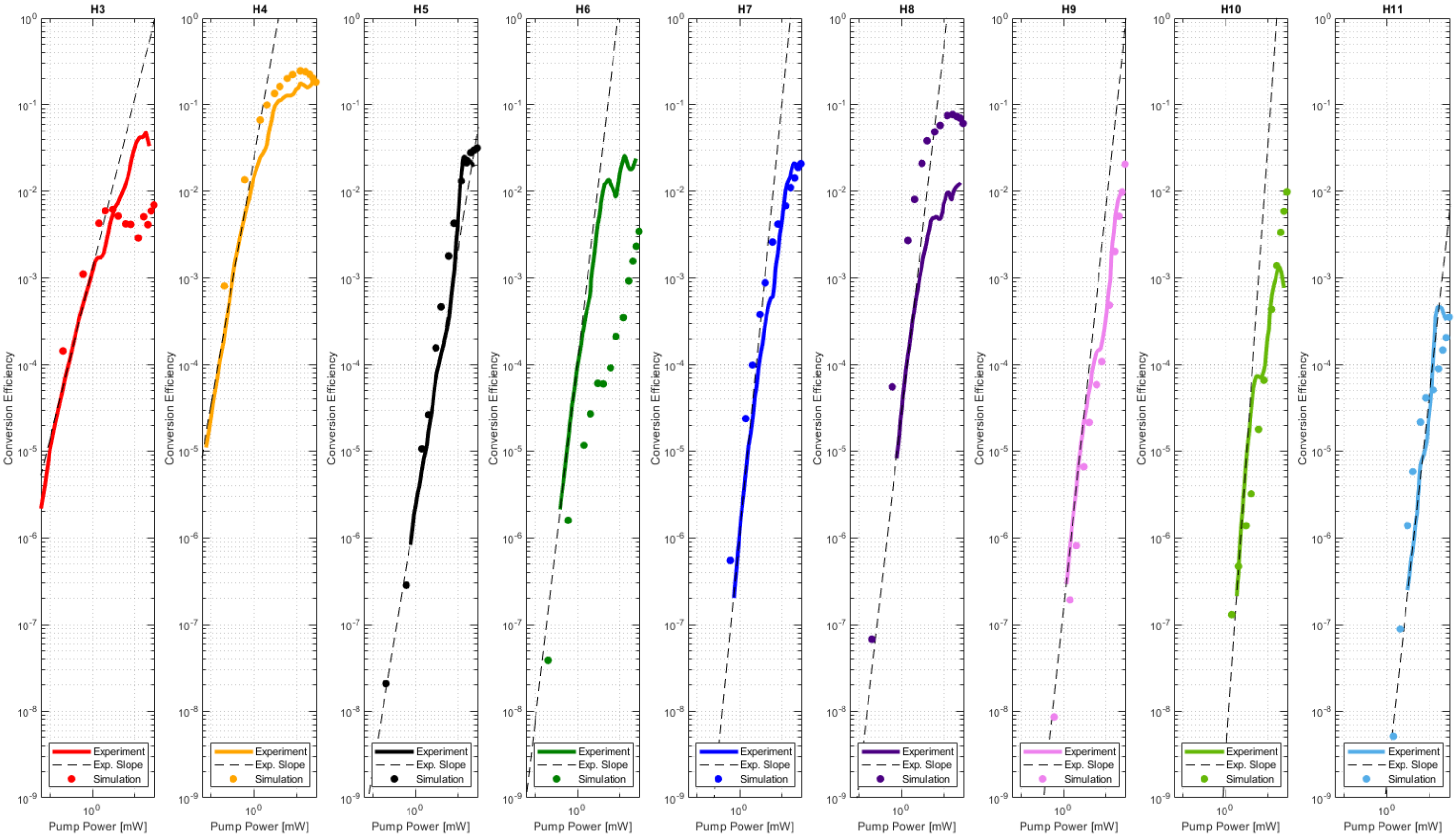

Figure 4.11: Conversion efficiency vs pump power for waveguide 2, backwards polling. The 4.1 um experiment data is shown as solid lines and the overlaid dots are the results of the simulation. Slopes have been fit to the experimental data in the low power regime and show quantitative agreement with the simulation for the majority of the harmonics. Additionally, the high pump power limit slopes, and conversion efficiency saturation values are predominately consistent between the experiment and the simulation. For the simulation the pump powers were multiplied by 2.0.

the simulation than we observe in the experiment, which is consistent with our analysis of figure 4.10. Also, consistent with the analysis of figure 4.10 is that the simulation overestimates the power build up in harmonic 8.

4.3.2 3 μm Pump Experiment Analysis

I chose to focus on analyzing the 4.1 μm experiment, because it is easier to show consistency between that data and the simulation as compared to our own 3 μm experiment. But we would expect that if cascaded $\chi^{(2)}$ processes can explain HHG in PPLN waveguides at 4.1 μm, then we would be able to also show correlation between the 3 μm data and the simulation. Figure 4.12 plots waveguide 5 conversion efficiency vs. frequency, for the 3 μm experiment, at pump powers ranging from 150 mW to 1200 mW. Overlaid are simulation runs at powers from 10 mW to 850 mW. The most apparent difference is that the experimental conversion efficiencies shift vertically together with increasing pump power, while the simulation shows a spreading out of the higher order harmonics. Consequently, the simulation over predicts the conversion efficiency to harmonics 5-9. We have thought that some of the power in the high harmonics has been generated into higher order spatial modes of the waveguide, which could reduce the effectiveness of QPM in the experiment. However, an examination into this possibility has shown that the coupling strength into the higher order modes is weak. Combined with the knowledge that the light output from the waveguide, when viewed on a camera, appears to be a clean fundamental mode, it seems unlikely that higher order spatial modes can account for the reduction in conversion efficiency to harmonics

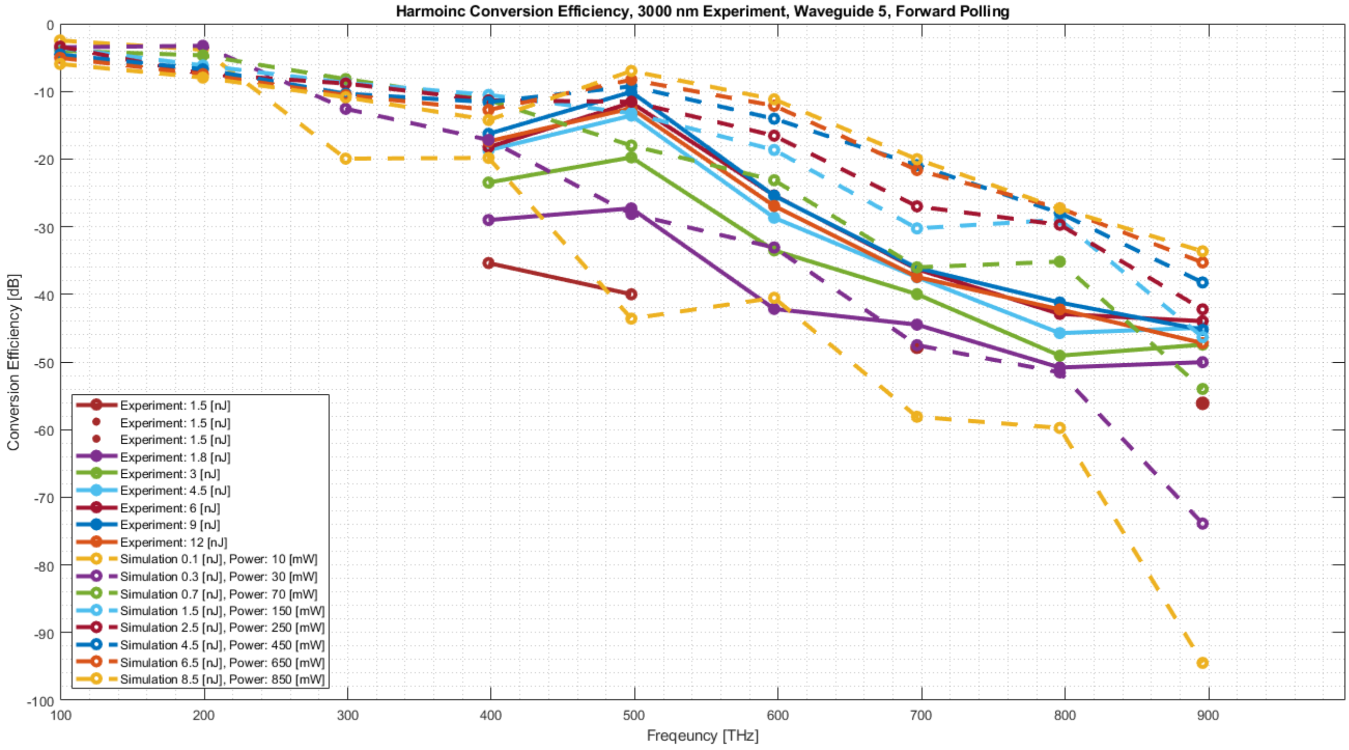

Figure 4.12: 3 μm, waveguide 5, forward direction polling, experimental conversion efficiency (solid lines) vs. frequency, at power levels ranging from 150 mW (1.5 nJ) to 1200 mW (12 nJ), with simulation data (10 mW - 850 mW) overlaid. The 1.5 nJ experimental data line is segmented because some of the harmonic peaks were bellow the noise floor of the detector. The simulation shows a spreading out of the harmonic conversion efficiency with increasing order which is not evident in the experimental data.

5 through 9.

Exactly the same as we did for the 4.1 um, we look toward the power scaling of the harmonics vs. pump power for clues. Figure 4.13 plots the experiment harmonic power scaling vs. pump power with the simulation data overlaid. The same as in the case of the 4.1 um analysis, a scale factor was applied to the simulation data in order to plot the conversion efficiency at an equivalent pump power. However, in this case determining a single scale factor by which to transform the x-axis is not straight forward as in the 4.1 um case, because there is less of an agreement between the slopes of the experimental data and the simulation. I chose a scale factor of 4 by attempting to align the slopes at the midpoint of the curve. There is no expectation for this scale factor to be the same as in the case of the 4.1 um experiment, because it includes biases like coupling efficiency into the waveguide, which we measured for only 1 attempt at waveguide coupling[2]. In figure 4.13 we observe that the slopes in the low pump power roughly agree for harmonics 5-9. Additionally, the simulated conversion efficiency is consistent with the experiment for harmonics 4 and 5, but the simulation overestimates the conversion efficiencies to harmonics 5-9.

Attempting to explain these observation, we decided to explore the effect of adding $\chi^{(3)}$ to the simulation. The details of this new model are explained in the methods section. Adding $\chi^{(3)}$, including delayed Raman response and instantaneous Kerr effect, can transfer energy from the light into vibrations of the

---

[2] We have observed discrepancies in the 3 μm and 4.1 μm data which suggest that coupling into the waveguides may not be exceptionally repeatable. At this time I have not quantified this potential source of error.

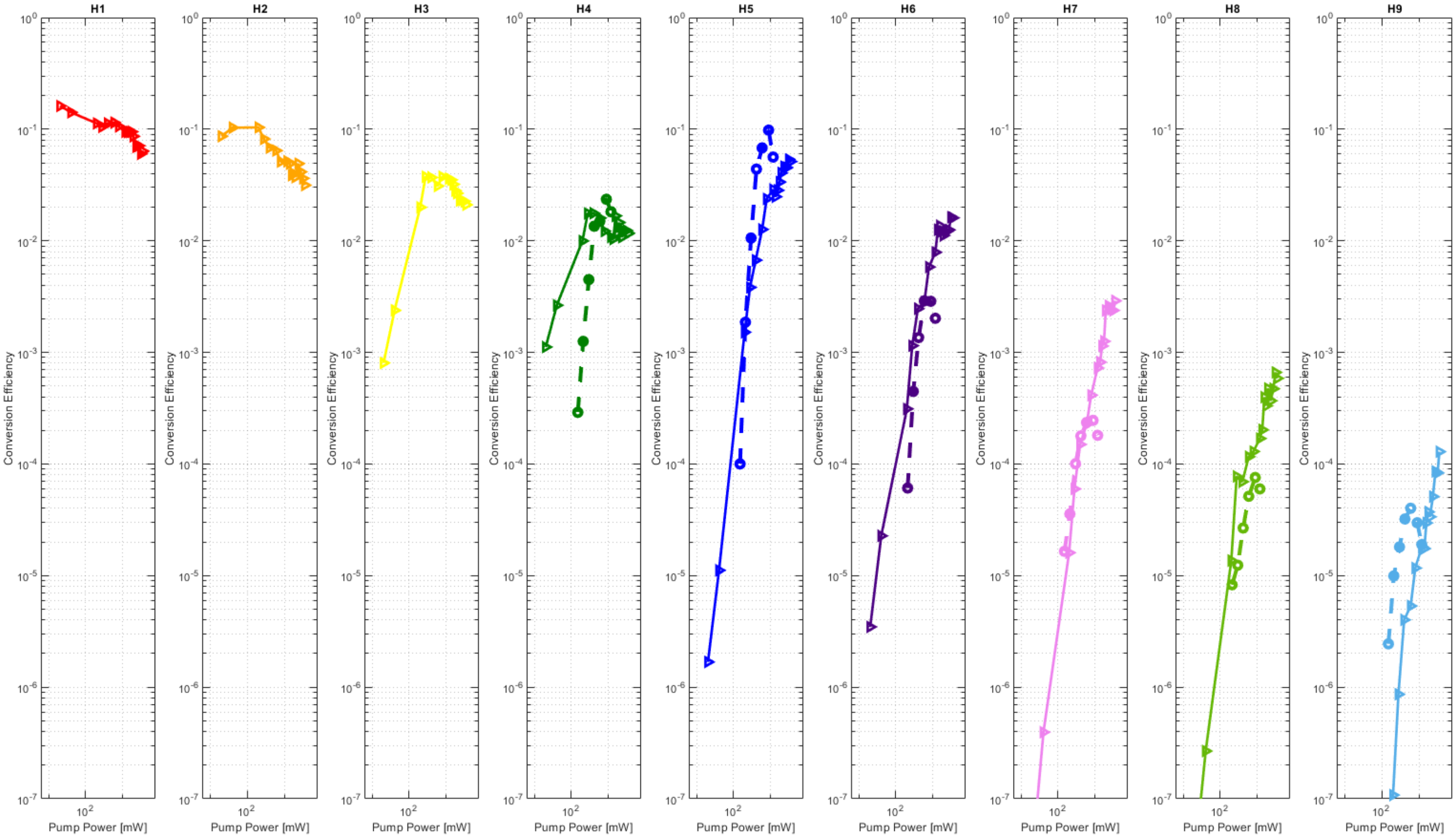

Figure 4.13: Harmonic power scaling vs. pump power for the 3 um experiment, compared to the simulation. Even though there is no experimental data for harmonics 1-3 the simulation results are still plotted as to illustrate the predicted saturation of harmonics 1-3. Harmonics 6, 7, 8, and 9 show a "convex profile" which is not as pronounced in the simulation. Additionally, the simulation overestimates the conversion efficiency to these harmonics

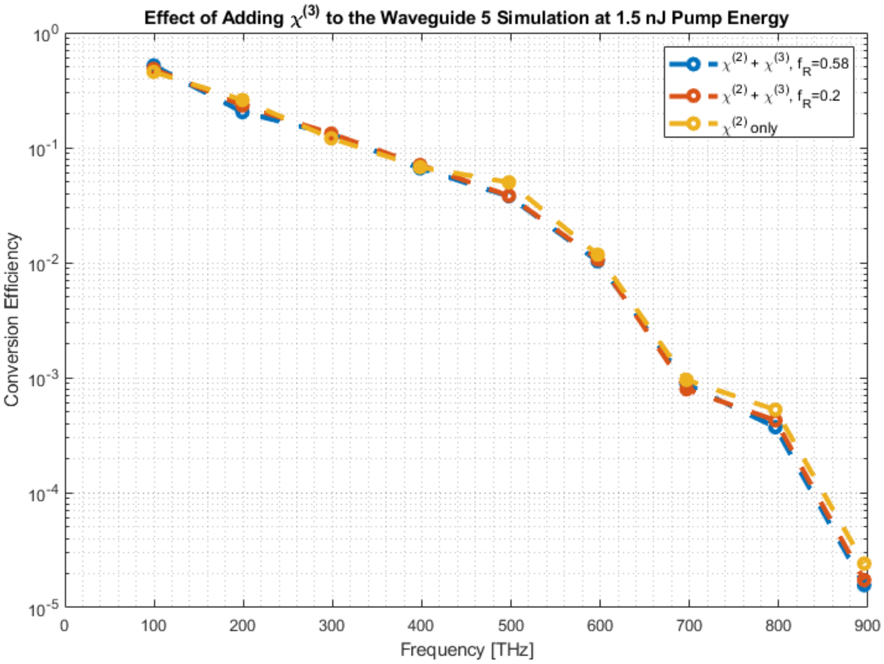

Figure 4.14: Simulated conversion efficiency vs. frequency for waveguide 5, pumped with 1.5 nJ, in the forward direction, for 3 different simulation models. The first is $\chi^{(2)}+\chi^{(3)}$ effects with a Raman fraction $f_R = 0.58$. The second is $\chi^{(2)}+\chi^{(3)}$ with a Raman fraction $f_R = 0.2$. And finally the "control" is shown which only included $\chi^{(2)}$ effects. While a minor reduction in the conversion efficiency to the high harmonics is observed with the addition of $\chi^{(3)}$ effects, this phenomenon does not explain the overestimation of conversion efficiency observed in 4.12.

crystal lattice (phonons) thus reducing the conversion efficiency to the harmonics; and also in general influence the cascaded $\chi^{(2)}$ mechanism. Figure 4.14 shows the effect of adding $\chi^{(3)}$ to the simulation by plotting harmonic conversion efficiency for $\chi^{(2)} + \chi^{(3)}$ effects with a Raman fraction $f_R = 0.58$, $\chi^{(2)} + \chi^{(3)}$ with $f_R = 0.2$, and $\chi^{(2)}$ only. While the addition of $\chi^{(3)}$ in the model does cause a slight reduction in the harmonic conversion efficiency it is not significant enough to explain the discrepancy observed between the simulation and experimental data. Most likely this is due to the magnitude of the $\chi^{(3)}$ term being significantly smaller than the $\chi^{(2)}$ term.

Despite what might not be considered strong numerical agreement there still exists qualitative agreement. As a final cases in point, figure 4.15 overlays of the experimental spectra from waveguide 5 with its simulation run. One final interesting feature to observe in both cases is the simulation seems to favor the larger lobe of the double peak input spectrum (see figure 4.16 in the Methods section), and the resulting harmonics are shifted slightly left of multiples of the 99.5 THz fundamental center.

4.4 PPLN Waveguide Conclusion

This study attempted to answer the question, "by what physical mechanism are high harmonics generated in chirped periodically polled Lithium niobate (PPLN) waveguides?" Because of Lithium niobate’s strong $\chi^{(2)}$ nonlinear response, one would expect cascaded $\chi^{(2)}$ process to dominate, however groups have reported

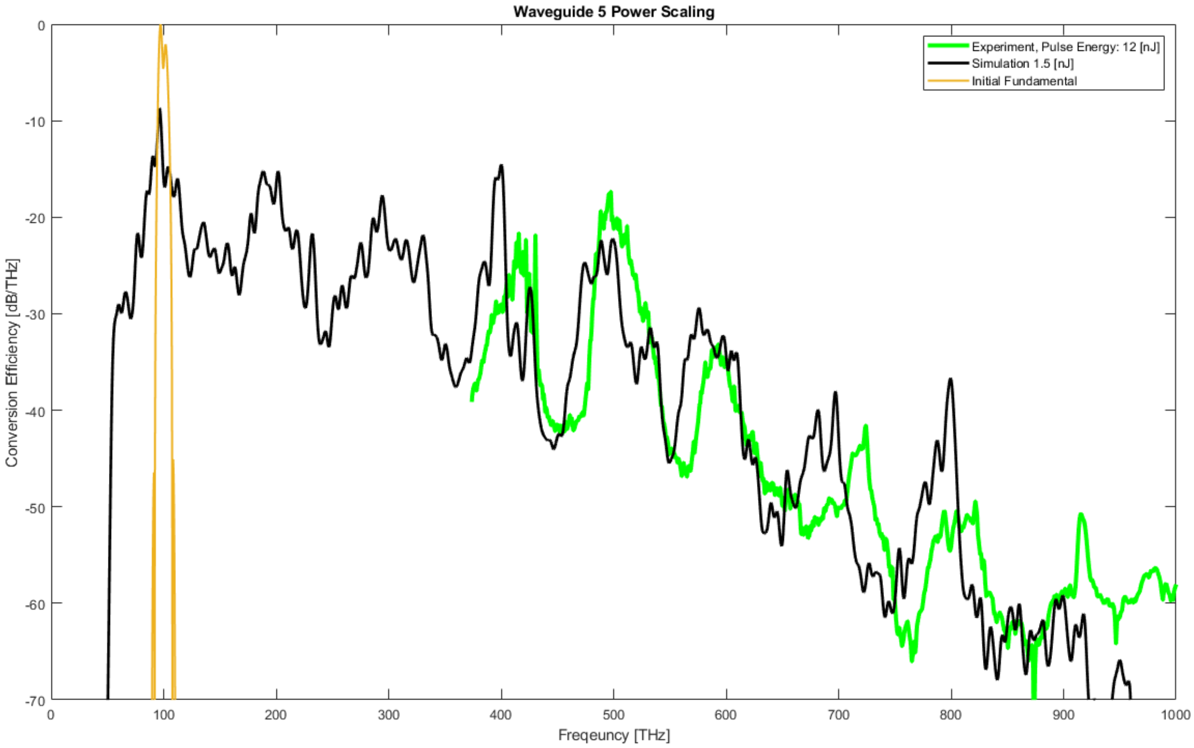

Figure 4.15: 3 um experimental spectrum from waveguide 5, overlaid with the simulation result illustrates qualitative agreement.

characteristics in the spectrum, and the nature of the power scaling, to be indicative of higher order perturbative process and non-perturbative physics. In order to shed light on this subject, we performed our own experiment pumping at 3 μm, 100 Mhz, and 1.5 nJ to 12 nJ pulse energy. This section presented the results of that experiment along with a re-creation of the data from a previous experiment on the same waveguides pumped at 4.1 μm and 1 MHz, and compared them both to a simulation which solves the generalized nonlinear Schrodinger equation with $\chi^{(2)}$ nonlinearity. We find agreement between the experiment and the simulation, and conclude that cascaded $\chi^{(2)}$ processes can explain the nature of the high harmonics generated by PPLN waveguides.

4.5 Methods

4.5.1 The Simulation

In order to model the nonlinear interaction in this PPLN waveguide we simulated $\chi^{(2)}$ and $\chi^{(3)}$ interactions using the broadband envelope equation given in Conforti [19]. This equation was solved with an adaptive embedded Runge-Kutta algorithm described in [7] and each run takes approximately 48 hours on a 4 core processor.

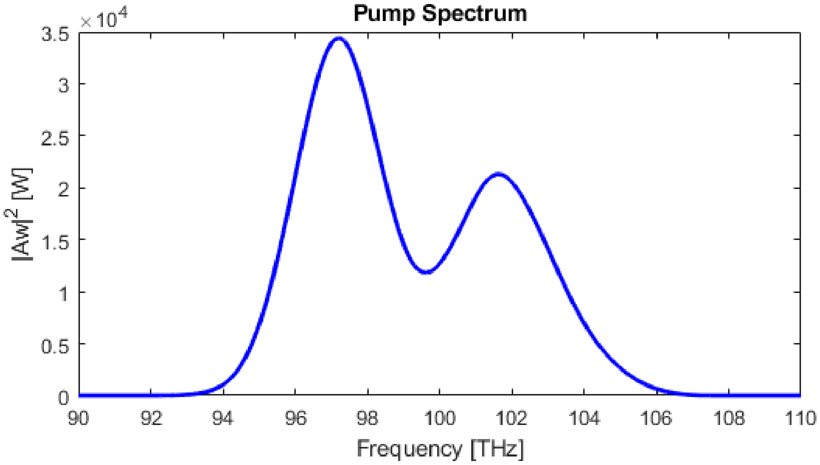

Figure 4.16: Pump peak power vs. frequency. The centroid of the spectrum is 99.5 THz, and has a double lobe feature.

Input Parameters

The simulation is set up with the following initialization and input parameters. The time grid is 2^{18} points, 120 ps wide, and has a resolution of 0.46 fs. This gives a sampling rate of 2185 samples/ps and a frequency grid which extends from minus to plus Nyquest frequency of 1092 THz, which is greater than the 9th harmonic, and into the UV absorption edge of Lithium Niobate. The input time domain envelope is constructed from the transform limited spectrum (figure 4.16) measured at the time of the experiment, which is centered around 3012 nm. A flat spectral phase is assumed. This pump pulse is normalized to units of $\sqrt{W}$ so that the envelope squared integrates to the pulse energy in [J]. The input pulse is also shifted in time to -56 ps (advance in time) to allow for the group delay of the harmonics.

The frequency dispersion model was constructed by fitting a Sellmeier

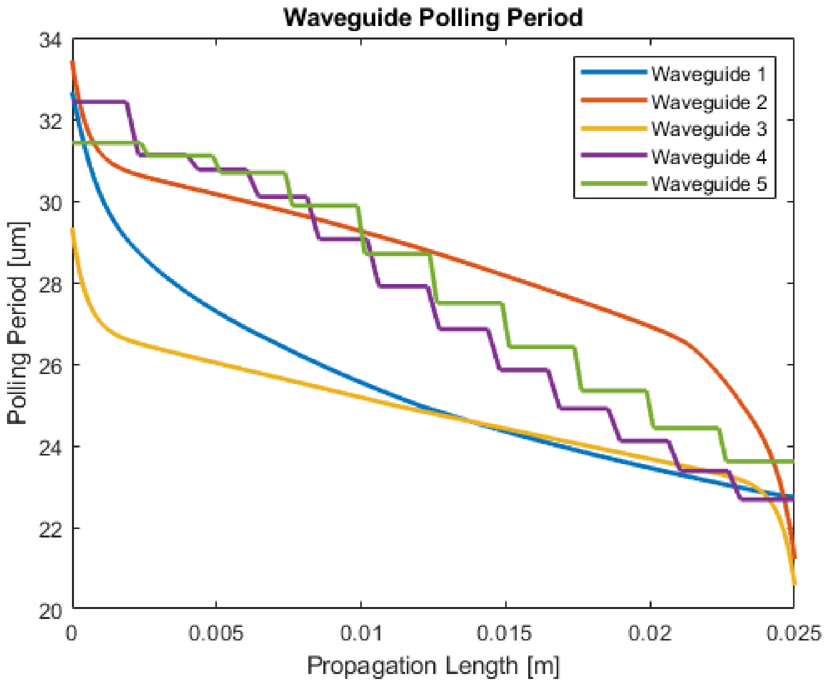

Figure 4.17: Polling period for each waveguide as a function of the propagation coordinate z [m]. Waveguides 1, 2 and 3 are smooth with hook like features at the start and end, while waveguides 4 and 5 have a stair-step profile with sections of constant polling.

equation to the real part of the index of refraction data calculated by COMSOL, which adds in the effect of waveguide dispersion. This dispersion model showed only slight differences from the bulk Lithium Niobate curve in the IR, which is where we would expect the waveguide dispersion to have a stronger effect. Absorption is accounted for in the simulation by manually entering the absorption edges of Lithium Niobate in the IR and the UV at 310 nm, and the edges were modeled as error functions 10 nm wide. The UV absorption edge is slightly bluer than the the 9th harmonic at 334 nm.

The nonlinear scaling terms for the $\chi^{(2)}$ and $\chi^{(3)}$ process are calculated using Lithium Niobate's $d_{eff} = 19.6\ pm/V$, intensity dependent index of refraction $n_2 = 83.3e-20\ m^2/W$ [6], an effective waveguide area of 108 μm^2 (calculated using COMSOL), and the central frequency of the pump pulse, $f_0 = 99.5\ THz$.

The poling period function of the propagation coordinate z [m], for each of the five 25 mm long chirped waveguides, are interpolated from 4096 points supplied by the manufacturer. These profiles are shown in figure 4.17. It is noteworthy that there are two distinct styles of polling profile. Waveguides 1, 2, and 3 are smooth but the polling period varies rapidly at the start and end of the waveguide. Compare this to waveguide 4 and 5, which have flat sections of constant polling, and generate harmonics more evenly throughout the crystal.

The initialization function returns the following parameters to the main simulation application, the time t [ps] and frequency grids ω [rad/ps], initial time domain electric field $At[\sqrt{W}]$, the nonlinear scaling values χ^2_{scale} $[1/(m\sqrt{W})]$ and γ [1/(m W)], the dispersion operator D [1/m] and the absorption profile α [1/m], the waveguide polling period [m], and β_0 [1/m] and β_1 [ps/m].

ERK4(5) Solver

The main application calls the adaptive Embedded Runge-Kutta ERK4(5) [7] function and passes it the initialization parameters. The ERK4(5) algorithm propagates the differential equation and saves the frequency domain electric field at 101 save points.

The ERK4(5) algorithm embeds a Split Step Fourier Methods (SSFM) into the coefficients of a 5th order Runge-Kutta solver with a 4th method embedded within which is used to adapt the step size. The RK coefficients are solved in the frequency domain by first applying the dispersion operator, inverse Fourier transforming to the time domain and applying the nonlinear operator, then Fourier transforming back to the frequency domain and applying dispersion operator again. The 4th and 5th order solutions are inverse transformed into the time domain and the absolute value of the difference between them is used to reject (accept) steps, while decreasing (increasing) the step size until this difference is within some error tolerance. The exact value of the error tolerance is unimportant, since the algorithm independently monitors accumulated fractional error in the power in each of the harmonics. We choose to accept total fractional errors $<= 0.1$. In order to achieve this the algorithm must takes steps $< 1e-7\ m$ (400000 total steps on average). Since the algorithm must perform 28 Fourier transforms of 2^{18} points at each step, the simulation is computationally costly to run.

The nonlinear operator is derived from the broadband envelope equation for $\chi^{(2)}$ media given in [19], with additional terms to account for the periodic polling period of the waveguide, and $\chi^{(3)}$ effects including instantaneous Kerr effect, and delayed Raman scattering. The broadband envelope equation for $\chi^{(2)}$ media, given by Conforti, which I showed how to derive in the introduction, is given in equation

4.1.

$$\frac{\partial A(z,t)}{\partial z} + iDA(z,t) = \frac{-i\chi^2}{4n_0c}\omega_0\left[1-\frac{i}{\omega_0}\frac{\partial}{\partial t}\right][A^2e^{i\omega_0t-ik_0z}+AS(|A|^2)e^{-i\omega_0t+ik_0z}] \tag{4.1}$$

Where the dispersion operator $D=\sum_{m=2}^{\infty}\frac{1}{m!}\beta_m\Big(-i\frac{\partial}{\partial\tau}\Big)^m$. And AS is the analytic signal representation, which is used to filter the negative frequency components so that an envelope, containing only positive frequencies , can be used to represent a real electric field. However, this operation is not strictly necessary because the negative frequency components cannot be phase matched, and consequently they are suppressed by orders of magnitude. Therefore, calculating the analytic signal in the frequency domain, which would require 14 more Fourier transforms for every step of the algorithm, is unnecessary and the following approximation can be made, $AS(|A|^2)\approx 2|A|^2$ Using this approximation, carrying out the derivatives, and moving to a reference frame which travels at the group velocity of the pump, yields the form of the equation which is propagated in the simulation of the 3 μm and the 4 μm experiment,

$$\begin{aligned}\frac{\partial A}{\partial z}+iDA=-i\,gP\,\chi^{(2)}_{scale}(\omega_0)\Big[\big(2A^2-\frac{2i}{\omega_0}A\frac{\partial A}{\partial\tau}\big)e^{i\omega_0\tau-i(\beta_0-\beta_1\omega_0)z}-\\ \frac{4i}{\omega_0}Re\big(A^*\frac{\partial A}{\partial\tau}\big)e^{-i\omega_0\tau+i(\beta_0-\beta_1\omega_0)z}\Big]\end{aligned} \tag{4.2}$$

And for the 3 μm data analysis, shown in figure 4.14, I chose to explore the effects of adding $\chi^{(3)}$ nonlinearity to the model by simulating,

$$\begin{aligned}\frac{\partial A}{\partial z}+iDA=-i\,gP\,\chi^{(2)}_{scale}(\omega_0)\Big[\big(2A^2-\frac{2i}{\omega_0}A\frac{\partial A}{\partial \tau}\big)e^{i\omega_0\tau-i(\beta_0-\beta_1\omega_0)z}-\\ \frac{4i}{\omega_0}Re\big(A^*\frac{\partial A}{\partial \tau}\big)e^{-i\omega_0\tau+i(\beta_0-\beta_1\omega_0)z}\Big]-i\gamma(\omega_0)\Big[1-\frac{i}{\omega_0}\frac{\partial}{\partial \tau}\Big]\Big((1-f_R)A|A|^2+\\ A\int_0^\infty f_R h_R(t\prime)|A(\ \tau-t\prime)|^2dt\prime\Big)\end{aligned} \tag{4.3}$$

Where the $\chi^{(2)}_{scale}(\omega_0)=\frac{1}{2}\frac{d_{eff}\omega_0}{n_0^{3/2}c}\sqrt{\frac{2}{\varepsilon_0 cA_{eff}}}$ which is consistent with this simulation's units of the electric field $\sqrt{W}$, and was transformed using the relation $|A'|^2 = 1/2\varepsilon_0 n_0 cA_{eff}|A|^2$ [3]. And the polling sign $gP = sign(cos(\frac{2\pi}{\Lambda}z))$ where Λ is the polling period. And the $\chi^{(3)}$ scale term $\gamma = \omega_0 n_2/(cA_{eff})$ [3], with Raman fraction $f_R = 0.58$ or $f_R = 0.2$ and the Lithium Niobate Raman response function $h_R(t)$ given by experimental measurement [6]. In the ERK4(5) solver the nonlinear function returns the right hand side of equation 4.2 or equation 4.3.

Making this simulation a computationally tractable problem requires parallel computing. This was done in 2 different ways depending on the goal. For single instances of the simulation the best course of action was to allow Matlab's inherent parallelization of Fast Fourier transforms to spread the computing load to all the cores in a CPU. On a 4 core I7 processor, a single instance takes about 40 hours to run. Alternatively, if a parameter search is required, many instances can be run in parallel, while allocating 1 core in the CPU for each instance. This method was utilized on a 16 core computer, and the run time is approximately 1 week.

The Return Values of the Simulation

The simulation saves the frequency domain electric field envelope A_ω $[\sqrt{W}]$, its location along the propagation coordinate z [m], and the accumulated fractional error in each of the harmonics, at 101 save points between 0 and 25 mm. The full frequency grid is saved meaning the size of A_ω array is $(101, 2^{18})$. The units of the frequency domain envelope are $\sqrt{W}$, which is the same as the time domain envelope A_t because the Fast Fourier Transform, $A_\omega = FFT(A_t)$, doesn't multiply by dt. The working units of the remainder of this analysis are [dBm/THz], so in order to convert A_ω the following operations are carried out. Assuming time and frequency units of ps and THz, and the repetition rate of the laser is f_{rep} [Hz], the spectral energy density E [J/Hz] is calculated from the raw simulation output by,

$$E = |A_\omega * dt * 1 \times 10^{-12}|^2 \tag{4.4}$$

so that the pulse energy Epp $[J]$

$$Epp = \int_{-\infty}^{\infty} E * df * 1 \times 10^{-12} \tag{4.5}$$

and the power spectral density PSD $[mW/THz]$ is

$$PSD = f_{rep} * E \; [J/THz] * 1000 \tag{4.6}$$

which can be integrated to obtain the total optical power $PW\ [mW]$

$$PW = \int_{-\infty}^{\infty} PSD * df \tag{4.7}$$

or used as the y axis units for the plots which will be shown in the following analysis of the results in the form $PSD\ [dBm/THz]$ according to,

$$PSD\ [dBm/THz] = 10 * log10(PSD\ [mW/THz]) \tag{4.8}$$

The ERK4(5) solver also returns the accumulated fractional error in each of the harmonics, at each save point in z, which is calculated according to the formula,

$$\text{Fractional Error} = \left| \sum_{steps} \frac{\int_n |A_\omega^{(5)}|^2 - |A_\omega^{(4)}|^2}{\int_n |A_\omega^{(5)}|^2} \right| \tag{4.9}$$

Where $A_\omega^{(5)}$ represents the 5^{th} order Runge Kutta solution, and the integration is performed over the bandwidth of the n^{th} harmonic. For example, a simulation run for waveguide 3 returned fractional errors which are mostly $< 10^{-2}$, and are shown in figure 4.18. Three elements are immediately noticeable. One, the error get significantly worse as the harmonic order increases, because the harmonics are generated by a cascaded process and so is the error. Second, the error appears to be constant for harmonics 6, 7, and 8, which means all the error was accumulated in the first few steps of the algorithm. Third, some of the errors decrease, which is because $|A_\omega^{(5)}|^2 - |A_\omega^{(4)}|^2$ can be negative.

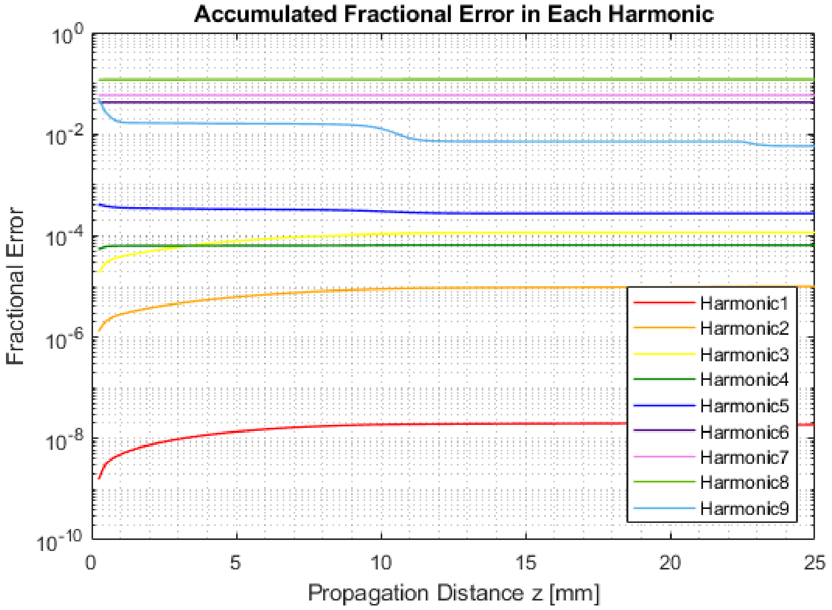

Figure 4.18: Accumulated fractional error in the power in each harmonic as a function of the propagation coordinate z.

4.5.2 Justification for Scaling the Pump Power axis in the Simulation

Figures 4.11 and 4.13 plotted conversion efficiency vs. pump power and figures 4.5, 4.6, and 4.15 show agreement between the simulation run at one pump power, and the experiment pumped at a different power. I offered argument without proof that it's acceptable to re-scale the simulation pump power in this manor to match the experiment. However, I feel compelled to rigorously justify this.

Rewriting the envelope equation 4.2, we get an alternate form of the equation being solved by the simulation,

$$\frac{\partial A}{\partial z} + iDA = -i\chi^{(2)}_{scale}(\omega_0)\left[1 - \frac{i}{\omega_0}\frac{\partial}{\partial \tau}\right][A^2 e^{i\phi} + 2|A|^2 e^{-i\phi}] - i\gamma|A|^2 A \tag{4.10}$$

Where $-i\gamma|A|^2 A$ term can be considered a proxy for the entire cubic nonlinear terms in the right hand side of 4.3, which has been left out of the explanation which follows for the purpose of brevity. Defining a unit-less normalized electric field by dividing by $\sqrt{P_0}$, where P_0 is the peak power in units W,

$$U = \frac{A}{\sqrt{P_0}} \tag{4.11}$$

And plugging this into equation 4.10 we find a differential equation for harmonic conversion efficiency,

$$\frac{\partial U}{\partial z} + iDU = -i\chi^{(2)}_{scale}(\omega_0)\sqrt{P_0}\left[1 - \frac{i}{\omega_0}\frac{\partial}{\partial \tau}\right][U^2 e^{i\phi} + 2|U|^2 e^{-i\phi}] - i\gamma P_0|U|^2 U \tag{4.12}$$

This indicates that scanning the simulation pump power is equivalent to scanning the nonlinear scale factor. We chose to parameter search by scanning pump power, but we could have also conditioned on one pump power and scanned $\chi^{(2)}_{scale}(\omega_0)$. Both approaches to calculating the harmonic conversion efficiency are mathematically equivalent.

However, the conversion efficiencies to the second the third order processes don't scale the same way with power. The conversion efficiency to the $\chi^{(2)}$ process is linear in $\sqrt{P_0}$ and the conversion efficiency to the $\chi^{(3)}$ term scales with $(\sqrt{P_0})^2$. For all of the analysis presented this point inconsequential because we only simulated $\chi^{(2)}$. Except for the analysis presented in figure 4.12, where we explicitly compare the effects of adding $\chi^{(3)}$ to the model with different Raman fractions. But in that figure we intentionally do not to include any experimental data because "technically" it would not be correct to scale the simulation pump power. I use "technically" in quotes because we have shown that the effect of adding $\chi^{(3)}$ is small, which is due to the fact that the magnitude of the cubic term is orders smaller than the quadratic term.

Another way to compare the relative strength of $\chi^{(2)}$ and $\chi^{(3)}$ is by parameterizing the differential equation in terms of a characteristic length scale $z' = z/L$, where $L =$ crystal length, we obtain,

$$\frac{\partial U}{\partial z'} = -iLDU - i\frac{L}{L_{NL}^{(2)}}\left[1 - \frac{i}{\omega_0}\frac{\partial}{\partial \tau}\right][U^2 e^{i\phi} + 2|U|^2 e^{-i\phi}] - i\frac{L}{L_{NL}^{(3)}}|U|^2 U \tag{4.13}$$

where we have defined separate nonlinear lengths for the $\chi^{(2)}$ and $\chi^{(3)}$ process, given by equations 4.14 and 4.15, which is simply an alternate parameterization to quantify the relative significance of the two factors,

$$L_{NL}^{(2)} = \frac{1}{\chi_{scale}^{(2)}(\omega_0)\sqrt{P_0}} \tag{4.14}$$

and,

$$L_{NL}^{(3)} = \frac{1}{\gamma(\omega_0)P_0} \tag{4.15}$$

Plugging the numbers in for a 3 μm, 3 nJ, pulse, we find $L_{NL}^{(2)} = 190\ \mu m$ and $L_{NL}^{(3)} = 1.8$ mm. Since $L_{NL}^{(2)} << L_{NL}^{(3)}$. This is consistent with our simulation data that shows $\chi^{(3)}$ effects play a small role in HHG in PPLN waveguides.

4.5.3 Detector Details

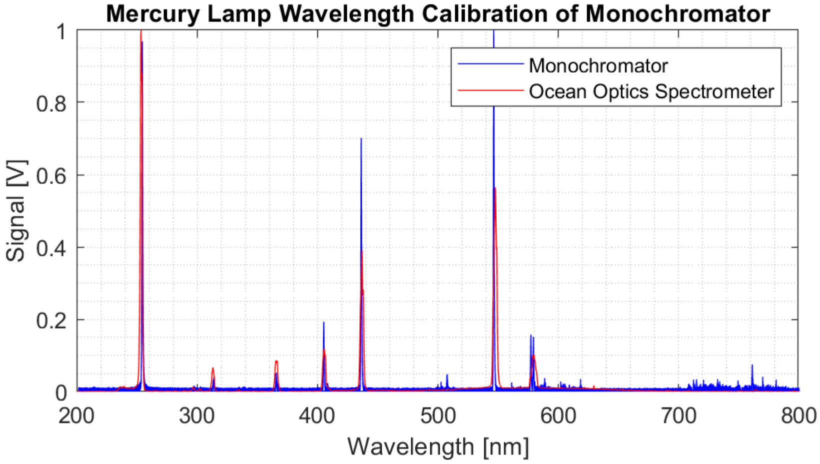

Figure 4.19: Spectrum from the Monochromator and the Ocean Optics Spectrometer vs. Wavelength when viewing a Mercury Lamp, which was used to calibrate the wavelength axis.

The monochromator used to spectrally resolve the harmonics is McPherson 0.3 m, Czerny–Turner style, UV-VIS monochromator with a UV enhanced Aluminium grating blazed for 300 nm. The sine drive is actuated via a stepper motor, which is controlled using an Arduino microcontroller that reports to a computer every time the motor steps. The position of the mechanism is tracked by recording the starting position manually and then the software will count steps from that known location. The monochromator has a wavelength indicator, which was calibrated using a HeNe, for the purpose of knowing approximately the wavelength being measured and returning the instrument to its known starting location. The monochromator drive proved to be extremely consistent, and the accumulated error from running the instrument 500k steps forward and backwards was less than 1 nm. The detector was a silicon photodiode, which was amplified by a Stanford Research Systems (SRS) transimpedance amplifier and typical gain settings were 200 nA/V. The resolving power is $\lambda/\Delta\lambda = 840$ at 546 nm. The dynamic range was determined to be 23 dB by measuring a HeNe laser with Monochromator and the SRS amplifier gain set to typical values.

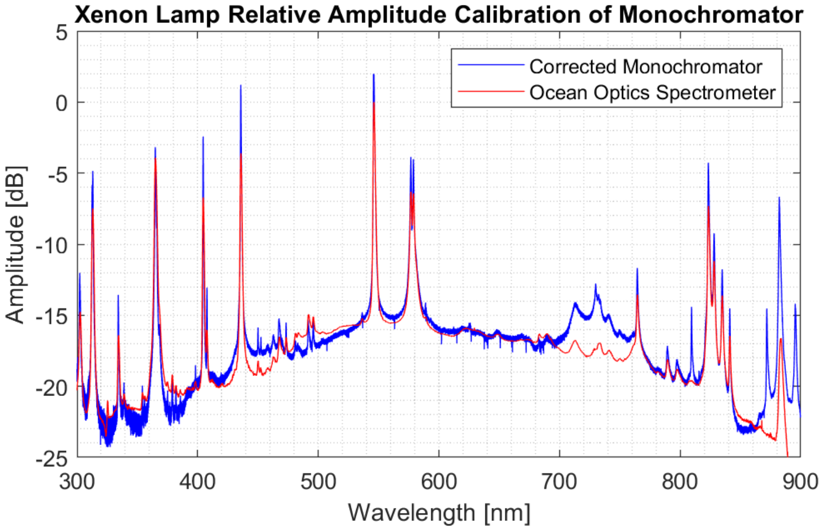

Figure 4.20: Spectrum from the Monochromator and the Ocean Optics Spectrometer vs. Wavelength when viewing a Xenon-Mercury Lamp, which was used to calibrate the relative amplitudes between the peaks.

The calibration of the wavelength axis was accomplished by comparing a Mercury lamp spectrum to the same spectrum measured by an Ocean Optics spectrometer, and then scaling the wavelength axis of the monochromator until the peaks lined up. We found the correction needed was only 0.6 nm. An overlay of the Mercury lamp spectrum used for calibration is given in figure 4.20.

The relative (wavelength dependent) response of the grating and the silicon photodiode system was calibrated using the broadband spectrum from a Xenon-Mercury Lamp. Three different calibration methods were tried, which included matching of the peaks between the Ocean Optics Spectrometer and and the monochromator, calibrating to the area under the peaks, and calibrating to the broadband background. We chose to use the broadband background calibration, which is shown in figure 4.20.

The absolute calibration of the monochromator was done by integrating the 6th harmonic in the experimental spectrum, and then scaling the experimental curve by a factor of C [mW/(A*nm)] until there was agreement with the power in the 6th harmonic—as reported by a calibrated photodiode which was observing only the 6th harmonic. This was accomplished by dispersing the waveguide output light via a prism (Fresnel loss was considered), spatially filtering via knife edges, and then focusing the 6th harmonic into the photodiode. Additionally, power scaling of the monochromator was checked by making sure the power in the 6th harmonic curve vs. pump power matched the photodiode. This curve is shown in figure 4.21.

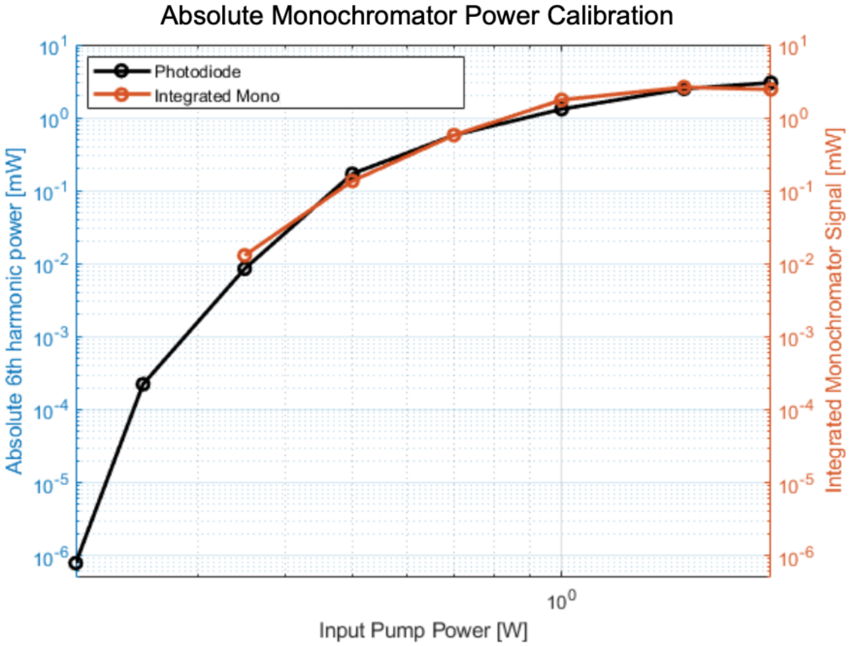

Figure 4.21: Absolute power in the 6th harmonic vs. pump power as measured by a power meter compared to the integrated monochromator signal after a calibration constant of C [mW/(A*nm)] was applied

5. Next Generation OPA Signal Seed

5.1 High Fidelity Modeling of Gain in Erbium Doped Fiber Amplifiers

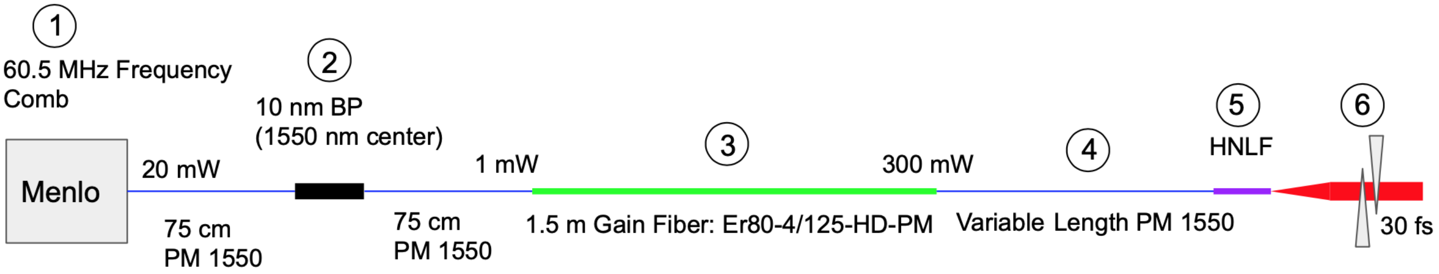

Figure 5.1: Concept drawing of the key elements of the next generation EDFA system intended to generate 30 fs pulses to seed the OPA. **1)** 60.5 MHz Frequency Comb manufactured by Menlo systems. **2)** 10 nm bandpass filter, centered around 1550 nm helps to reduce pulse broadening in the time domain by narrowing the spectrum. **3)** Erbium doped gain fiber is the active amplification element. **4)** A variable length of anomalous dispersion PM 1550 fiber serves as the compression fiber for a normally chirped pulse. **5)** A maximally compressed pulse is launched into a Highly Nonlinear Fiber (HNLF) which generates a broad bandwidth. **6)** The broad bandwidth is compressed via variable thickness, anomalously dispersive fused silica wedges into a ~ 30 fs pulse which seeds the OPA.

One of the key points of the section on the OPA development was that achieving short 3 μm pulses ($\sim$ 30 fs, 3 optical cycles) is currently being limited by the temporal compression of the signal seed. Since MIR pulses are essential for developing the OPA into a light source for generating attosecond pulses, it is a priority that we upgrade the signal to seed the OPA with broadband temporally compressed pulses.

To that goal, the key elements of the next generation EDFA system are illustrated in Figure 5.1. This design is intended to seed the OPA with broadband pulses that are maximally compressed in time, so that the entirety of the bandwidth is co-temporal with the 1035 nm pump light in the OPA. This is crucial to generating broadband $3\mu m$ idler pulses, and realizing the full performance potential of the OPA. It has been shown that this EDFA design can produce pulses as short as 10 fs (FWHM) [71] with 800 nm of bandwidth. And while that is significantly greater bandwidth than can be theoretically phase matched in the OPA, it's interesting to consider (and aim for) seeding the OPA with an ultrabroaband pulse.

In the interest of focusing on the element of the EDFA system with most novel scientific impact, this section reports on a newly developed model for a high rep rate ($\sim MHz$) nonlinear Erbium Doped Fiber Amplifier (EDFA) pumped at 980 nm and seeded at 1550 nm. Specifically, this section focuses on the 1.5 m segment of Erbium doped gain fiber (element 3 in figure 5.1), which is the active component of the signal seed branch of the OPA. Therefore, accurate numerical modeling is important to designing the next generation OPA signal seed. My approach uses a hybrid coupling of the laser rate equations, in the two-level approximation, with the Generalized Nonlinear Schrodinger Equation (GNLSE) in order to capture, in high fidelity, the physics of laser amplifiers plus waveguide effects like dispersion and self phase modulation (SPM). It's important to note that a method similar to this has been proposed for modeling gain in Ytterbium doped fiber [44], where it showed good agreement with experimental results. However, the method published in [44] has not been studied in detail.

There have been various numerical models developed to simulate Fiber Amplifiers (EDFA). They can be broadly categorized into models based on the laser rate equations in the continuous wave (CW) limit [2, 51, 59]; solutions to the Maxwell-Bloch equations in the limit of a limited pulse train of ultrafast pulses [28, 45, 48]; and the modified Nonlinear Schrodinger Equation (NLSE) with a complex Lorentzian gain spectrum and a saturable absorber amplitude function. [39, 40, 58]. Each method has been developed and tailored to simulate the corner of the operating envelope of EDFAs which best address the areas of active research at that time. Consistent with this practice, this study seeks to contribute to a niche in the modeling of EDFAs in an up and coming regime of operation. Specifically, high rep rate ($\sim$ MHz) non-linear EDFAs, pumped at 980 nm and seeded with 1550 nm, which are being used for many applications (in addition to seeding OPA's) such as spectroscopy [70] and generating octave spanning supercontinuum [78].

The model we adopt is the two-level rate equations in the steady state approximation. The two-level approximation is valid in the limit that the pumping rate Ω_{pump} to the 3rd level (980 nm) is slower than the nonradiative decay rate Ω_{decay} from levels 3 $(980\ nm) \rightarrow 2\ (1550)\ nm)$. In this case no significant popu-

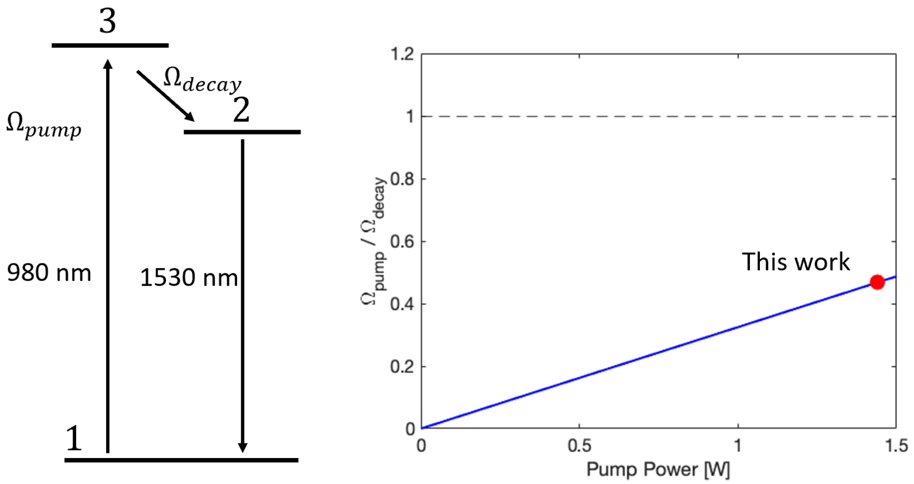

Figure 5.2: (left) energy level diagram identifying the pumping rate Ω_{pump} and nonradiative decay rate Ω_{decay} from the 980 nm level to the 1530 nm level. (right) plot of $\Omega_{pump}/\Omega_{decay}$ for the power ranges applicable to this analysis. Red dot indicates the maximum pumping power. As this ratio approaches 1 the two-level approximation becomes questionable. The energy levels arise from the Stark splitting of the 4f shell in the Er^{3+} ion.

lation accumulates in level 3. Equation 5.1 gives the pumping rate as a function of pump power P_p, pump absorption cross section σ_{ap}, pump frequency ν_p, and effective area A_{eff} [27].

$$\Omega_{pump} = \frac{P_p \sigma_{ap}}{h \nu_p A_{eff}} \tag{5.1}$$

For Er:doped fused silica fiber $\Omega_{decay} = 1/(7\ \mu s) = 143$ kHz [10]. In [27] it was calculated that this limit is satisfied (for typical EDFA configurations) when the average pumping power is $< 1W$. In figure 5.2 we justify this further by plotting $\Omega_{pump}/\Omega_{decay}$ up to the maximum pumping power used in this analysis. It's potentially interesting to explore the validity of the 2 level approximation by way of careful comparison of simulation to experiment, since operational EDFA pumping powers are typically around 1 W. The steady state approximation is reasonable because the depletion of the excited state population fraction from a single ultrafast pulse is insignificant, as reported by [15]. This implies the EDFA responds to a time average of all the pulses.

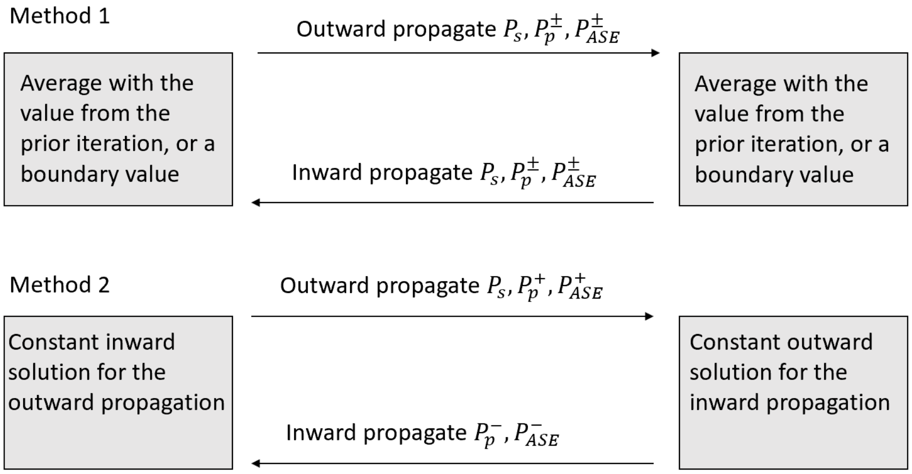

Figure 5.3: Basic flow of the two iterative methods used to converge the coupled differential equations. Method 1 involves propagating all 5 equations outward $(z = 0 \rightarrow z = L)$ and inward $(z = L \rightarrow z = 0)$ simultaneously, and averaging the values at the endpoints with either the value from the previous iteration or a boundary value when known. In method 2 only the equations co-propagating with the signal are solved on the outward leg, and the equations counter-propagating with the signal are solved on the inward leg.

Laser amplifier characteristics, such as pump depletion, gain saturation, and amplified stimulated emission (ASE), were explored both numerically [2, 51] and analytically [59] in the 1990's. However, these studies focused on peak power levels where non-linearity was not a factor. As a result, there was no need to merge these elements of a laser amplifier model with fiber non-linearity. In this section we present an Erbium Doped Fiber Amplifier model designed for a MHz repetition rate, picosecond-pulse duration, non-linear EDFA, which combines elements including pump absorption, amplified stimulated emission, excited-state population depletion, and gain saturation; along with fiber dispersion and non-linearity; and consideration to multiple pumps which are co-propagating and counter propagating with the signal. We also compare the results of our model to a simpler saturable absorber gain model, and discuss their agreement.

The Erbium gain fiber parameters summarized in table 5.1 are for the Er80-4/125-HD-PM gain fiber, and have been given to us by the manufacturer nLIGHT. Where there is an asterisk, the a fiber parameter's value is not well known, and we used general parameters from literature or from correspondence with collaborators. Additionally, we were provided with gain $g(\lambda)$ and absorption $a(\lambda)$ curves by the fiber manufacturer, which we used in this simulation.

The spirit of the simulation is an embedded Split Step Fourier Method (SSFM), which solves the NLSE, inside a 4^{th} order Runge-Kutta (RK4) algorithm that propagates the laser rate equations. At each step of the simulation, the RK4 method evolves the average power contained in each spectral bin, calculates the excited state population fraction N, and informs the NLSE of the gain function $g(N)$ where gain is applied, and dispersion and nonlinear effects are modeled. The steady state rate equations for the power spectrum of signal frequencies $P_s(\nu)$, co-propagating and counter propagating pump $P_p^+(\nu)$ and $P_p^-(\nu)$, and forward propagating and backward propagating ASE $P_A^+(\nu)$ and $P_A^-(\nu)$, are given in equations 5.2 - 5.4. These equations are modified from those given in [10] in order to

Dispersion [ps/(nm*km)]	-22
Dispersion slope $[ps/(nm^2 * km)]$	0.046
GVD (β_2) $[ps^2/km]$	28.06
TOD (β_3) $[ps^3/km]$	0.028
Non-linear parameter (γ) [1/(W*km)]	3.5*
Mode field diameter $[\mu m]$	6.5
Peak core absorption @ 1530 nm [dB/m]	80
Numerical aperture	0.2
Core Radius $[\mu m]$	1.4*
Radius of Erbium distribution $[\mu m]$	1.0*
Erbium doping concentration $[m^{-3}]$	5.9×10^{25}
Excited state lifetime τ [ms]	9.5
Intrinsic fiber loss α [1/m]	0.01*

Table 5.1: Er80-4/125-HD-PM fiber parameters, which were used in this simulation, and obtained from the fiber manufacturer or estimated based on other parameters.

utilize the gain $g(\nu)$ and absorption $a(\nu)$ curves obtained from the fiber manufacturer, instead of cross sections.

$$\frac{dP_p^{\pm}}{dz} = \pm(a+g)NP_p^{\pm} \mp aP_p^{\pm} \mp \alpha P_p^{\pm} \tag{5.2}$$

$$\frac{dP_s}{dz} = (a+g)NP_s - aP_s - \alpha_s P_s \tag{5.3}$$

$$\frac{dP_A^{\pm}}{dz} = \pm(a+g)NP_A^{\pm} \pm gN2h\nu\Delta\nu \mp aP_A^{\pm} - \mp\alpha P_A^{\pm} \tag{5.4}$$

Where N is the excited state population fraction, h is Planck's constant, and α is the intrinsic fiber loss parameter. The excited state population fraction N is be calculated using formula, 5.5

$$N = \frac{\sum_{\nu} \frac{a}{h\nu\xi} P_s \, + \, \sum_{\nu} \frac{a}{h\nu\xi} P_A \, + \sum_{\nu} \frac{a}{h\nu\xi} P_p}{\sum_{\nu} \frac{a+g}{h\nu\xi} P_s \, + \, \sum_{\nu} \frac{a+g}{h\nu\xi} P_A \, + \, \sum_{\nu} \frac{a+g}{h\nu\xi} P_p \, + 1} \tag{5.5}$$

Where the total ASE power P_A is the sum of the forward propagating and backward propagating ASE ($P_A = P_A^+ + P_A^-$), and the total pump power is the sum of the co-propagating and counter propagating pump [10]. The fiber saturation parameter ξ is calculated according to the formula $\xi = E_{sat} * f_{rep}(a+g)/(h\nu)$, where f_{rep} is the repetition rate of the laser, and the saturation energy is estimated to be $E_{sat} = 1\ nJ$ for Erbium doped fiber.

Merging the rate equations with pulse dispersion and non-linearity is accomplished by embedding a SSFM routine within the RK4 loop. The SSFM is the standard way of solving the GNLSE 5.6, which in this form is valid for few cycle ($\sim fs$) pulse durations, and broad bandwidth, [3] where the time domain envelope $U(t,z)$ is assumed to be moving at the group velocity ($t = t' - v_g z$).

$$\begin{aligned} \frac{\partial U}{\partial z} - \frac{i\beta_2}{2}\frac{\partial^2 U}{\partial t^2} - \frac{\beta_3}{6}\frac{\partial^3 U}{\partial t^3} + \frac{igG_\omega}{2}U = -i\gamma\Big[1 - \frac{i}{\omega_0}\frac{\partial}{\partial \tau}\Big] \\ \Big((1-f_R)U|U|^2 + U\int_0^\infty f_R h_R(t')|U(\tau - t')|^2 dt'\Big) \end{aligned} \tag{5.6}$$

The operator $i\frac{g}{2}G_\omega$ has been added to the NLSE to account for signal gain in the amplifier. The coefficient g captures the z dependence of the gain and G_ω is the complex Lorentzian gain envelope given by formula 5.7 [67],

$$G_\omega = \frac{-\omega}{0.5\Delta\omega}\frac{1}{1+\left(\frac{\omega}{0.5\Delta\omega}\right)^2} + \frac{i}{1+\left(\frac{\omega}{0.5\Delta\omega}\right)^2} \tag{5.7}$$

$\Delta\omega$ was calculated using a FWHM $\Delta\lambda = 35$ nm ($\Delta\omega = 27$ rad/ps), which was determined by the gain spectrum bandwidth provided by the fiber manufacturer.

At the start of the simulation, the signal power P_{s0} is initialized by renormalizing $|U_{\omega 0}|^2$ according to formula 5.8

$$P_s = P_{ave}\left(\frac{|U_\omega|^2}{max(|U_\omega|^2)}\right) \tag{5.8}$$

Where P_{ave} is the average power in the beam. We also define a narrow bandwidth pump, both forward and backward $P^{\pm}_{P0}$, centered around 980 nm, and initialize $P^{\pm}_{A0}$ spectrum both to zero. Next the algorithm takes a step along the propagation distance z and the RK4 routine propagates the average power in all the beams using the rate equations. Then the gain parameter g is calculated according to formula 5.9

$$g = (a_{\nu_s} + g_{\nu_s})N - a_{\nu_s} - \alpha_s \tag{5.9}$$

Where the absorption and emission coefficients a and g are evaluated at the central signal frequency $\nu_s = 193\ THz$. This means that the gain spectrum is determined by the Lorentzian model, but the gain amplitude is scaled by g which is a function of the excited state population fraction N. Finally, the algorithm completes the steps of the SSFM. At the end of the SSFM, the power in the signal P_s is calculated from U_ω again using 5.8 and this is fed back to the RK4 solver. One step of the algorithm is summarized in equation 5.10

$$\begin{aligned}
&N \leftarrow \mathit{Propagate\ the\ Rate\ Equations}(P_s, P_p^{\pm}, P_A^{\pm}) \\
&g = (a_{\omega_s} + g_{\omega_s})N - a_{\omega_s} - \alpha_s \\
&U_\omega = U_\omega \exp\left((-1/2 i\beta_2 \omega^2 - 1/6\beta\omega^3 - i\frac{g}{2}G_\omega)dz/2\right) \\
&U_t = IDFT\{U_\omega\} \\
&U_t = U_t \exp\left(NL * dz\right) \\
&U_\omega = DFT\{U_t\} \\
&U_\omega = U_\omega \exp\left((-1/2 i\beta_2 \omega.^2 - 1/6\beta_3\omega^3 - i\frac{g}{2}G_\omega)dz/2\right) \\
&U_t = IDFT\{U_\omega\} \\
&P_s = P_{ave}\left(\frac{|U_\omega|^2}{max(|U_\omega|^2)}\right)
\end{aligned} \tag{5.10}$$

Where NL is the nonlinear operator given by the right hand side of equation 5.6, and P_{ave} is the average power in the beam.

Since this problem is an initial value problem for 5 parameters, but only the initial values of the signal P_s, co-propagating pump P_p^+, and forward ASE P_A^+ are known at the start of the grid, it is necessary to iterate the solver, using the result from the outward solution $(z = 0 \rightarrow z = L)$ as the initial values for the inward solution $(z = L \rightarrow z = 0)$ and until the simulation converges. The simulation does this in two different ways depending on the forward and backward propagating pump powers. For high backward pump powers and low forward pump powers the best method to ensure convergence is to propagate all 5 differential equations for pump, ASE, and signal simultaneously, and average the values at the end points. A depiction of this is titled "Method 1" in figure 5.3. For both low backwards and forwards pump powers, and any forward pump power greater than 0.3 W, the best method is to solve the co-propagating beams only on the outward solution and the counter-propagating beams on the inward solution, while using the results from the previous solution to calculate N. This is "Method 2" in figure 5.3 Both strategies allow the solution to relax to a self consistent one in less than 48 iterations in their respective domains of applicability. To monitor convergence the algorithm calculates the sum of the squared difference between the excited state fraction N curves for the outward and inward solutions, and I have chosen to accept values < 0.001 as criteria for successful convergence.

This model was compared to a saturable absorber gain profile, which is an approximate model for the behavior of a system where amplification is reduced at high optical intensities, e.g. a laser amplifier were absorption of the pump light simultaneously causes, and is dependent on, the depletion of doping ions in the ground state. This model is given by equation 5.11, where g_0 is a free parameter which must be set by the user so that the simulation matches the experimentally measured power output of the amplifier, P_{ave} is the average power, and P_{sat} is the saturation power. The clear shortcoming of this model is that the user must have prior knowledge of the power output of the amplifier in order to manually adjust

g_0.

$$g = \frac{g_0}{1 + \frac{P_{ave}}{P_{sat}}} \tag{5.11}$$

The input time domain electric field for this simulation was obtained by measuring the actual spectrum from our 60.5 MHz frequency comb, manufactured by Menlo Systems. A home built SHG FROG (Frequency Resolved Optical Gating) was used to reconstruct $E(t)$ and determine the spectral phase. Because a Second Harmonic Generation (SHG) FROG trace can only give the magnitude of the chirp and not the sign, the pulse was determined to be anomalously chirped (Group Velocity Dispersion (GVD) < 0) by noting that it broadens monotonically when propagating down anomalously dispersive (PM 1550) fiber. This spectral phase was applied to a super Gaussian spectrum with 10 nm of bandwidth, and an average power of 1 mW, and is the input to the simulation.

The Matlab code for the simulation which utilizes the saturable absorber gain model is included in the appendix. The code uses essentially the same split-step algorithm as in 5.10 except the steps are embedded in a 4th order Runge-Kutta method, with an embedded 3rd order for local error estimation and control. This adaptive ERK3(4) method automatically adjusts the step size to compensate for the local strength of the nonlinear operator and is described in [8]. The full code which solves the coupled rate equation and GNLSE model is significantly more complicated, and too long to put in the appendix.

The results of running this simulation are compared to the saturable ab-

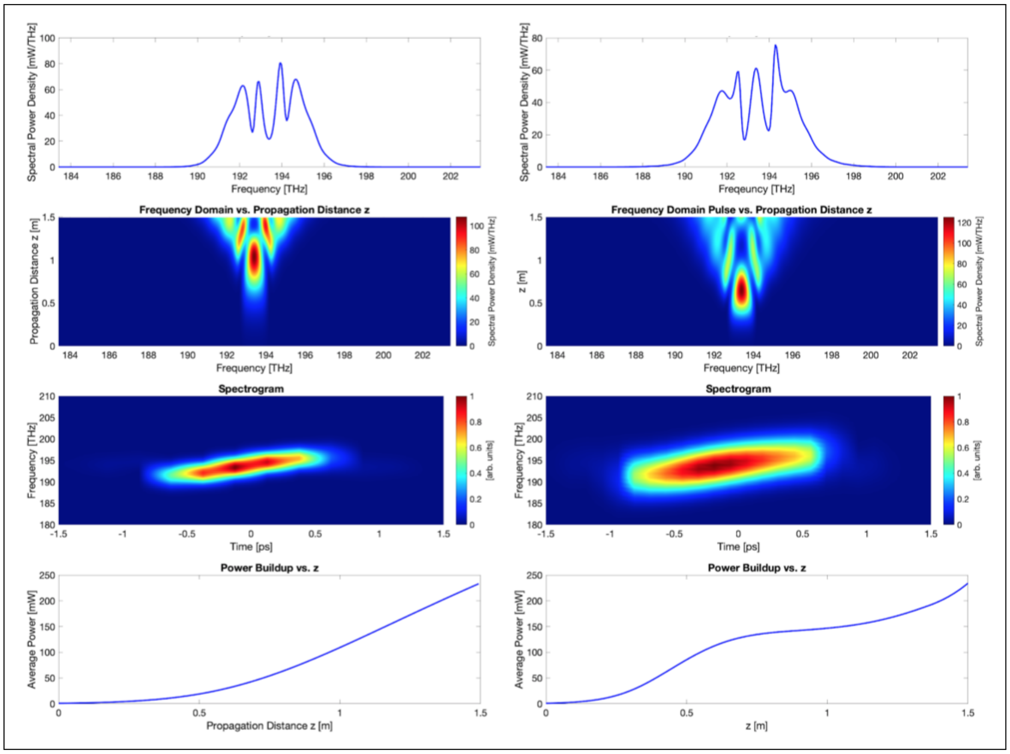

Figure 5.4: Side by side comparison of the saturable absorber gain model (left) vs. this simulation model (right) in the following fields (top to bottom) final pulse spectrum, spectrum vs. propagation length z, frequency vs. time spectrogram, and average power buildup vs. z. This comparison was made in the maximum power pumping configuration of 1 forward (540 mW) and 2 backward pumps (1080 mW total).

sorber model in figure 5.4 for a max power pumping configuration of 1 co-propagating (forward), 540 mW pump, and 2, 1080 mW, counter-propagating (backward) pumps. The coupling efficiency between the pump and the gain fiber was estimated to be 0.9, and all the power levels reported consider the coupling loss. These parameters resulted in simulation output powers of 234 mW, which in our experience is typical for these amplifiers. Our EDFA model has the ability to predict the final power output of the amplifier from fiber properties, and input

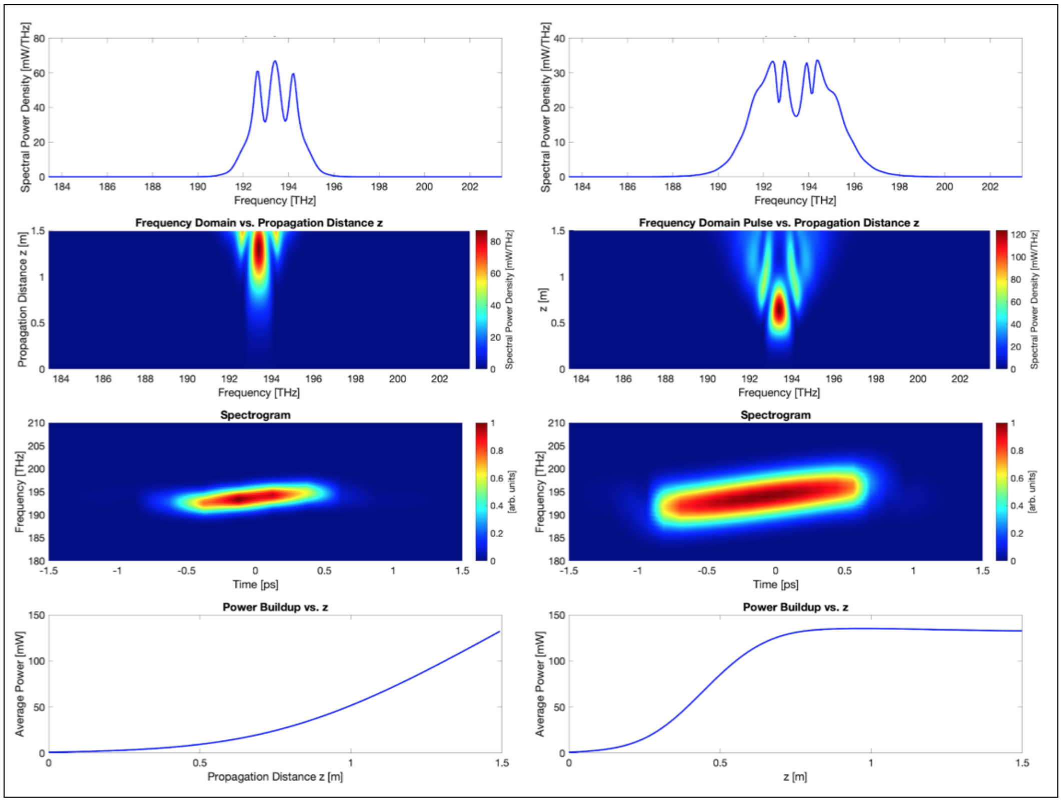

Figure 5.5: Same as figure 5.4 except 1 forward (540 mW) pump only was used in this simulation. Once again our model predicts a stronger built up earlier in the amplifier, which enhances the nonlinear effects in the gain fiber.

pulse parameters. However, in the case of the saturable absorber model the gain factor g_0 is arbitrary and must be manually adjusted. This was done by running our simulation first, noting the 234 mW output power, and then tuning g_0 to match that final power so that the models can be compared on an level plane.

Figure 5.4 shows a side by side comparison of the saturated absorber gain model (left) and the model developed in this study (right) in the 1 forward (540 mW) and 2 backward (1080 mW total) pumping configurations. The most notable difference between the two models is the gain profile (i.e. power vs. z). Our model shows a significant buildup of power early in the amplifier (lower right plot in figure 5.4) while the saturable absorber gain model builds up the majority of the power in the second half of the amplifier. Consequently, nonlinear effects begin to dominate sooner in our model, which in turn generates a broader spectrum by the end of the amplifier. Figure 5.5 shows the same side by side comparison as 5.4, except in this case 1 forward (540 mW) pump was simulated. Here the asymmetric pumping configuration causes the gain to completely saturate down the EDFA, and there is some re-absorption of the 1550 nm signal light. This is caused by a depletion in the excited state population. This effect is clearly not captured in the saturable absorber model which will always show the same gain profile regardless of pumping configurations. In summary, the models tend to be more consistent when the EDFA is pumped with 1 forward and 2 backward pumps, but disagree when pumped with 1 forward pump.

From the time-frequency spectrogram (3rd row of figures 5.4 and 5.5) we observe that the lower frequency components (i.e. "red light") emerges sooner from the amplifier than the higher frequency ("blue") components. Meaning the starting anomalously chirped pulse has passed through the point of maximum temporal compression inside the amplifier and emerges normally chirped. This fact is critical for compressing the pulse in the next stage of the amplifier, which propagates the signal down a length of anomalous PM 1550 fiber. It's easy to adapt the code included at the end of this thesis to do that element of the simulation.

An important factor to consider when solving differential equations is

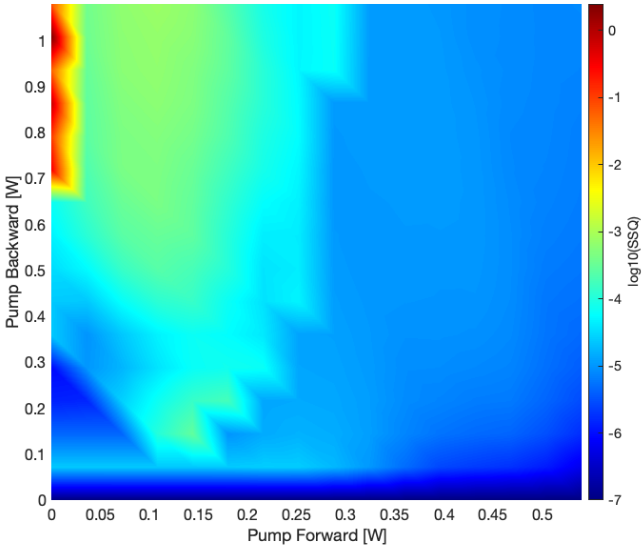

Figure 5.6: Stability landscape as a function of forward and backward pump power. Regions of blue and turquoise show where the algorithm has converged while the orange and red regions indicate lack of convergence.

convergence, especially in this case where it takes many forward and backward iterations of the solver to converge to a self consistent solution. For the set of parameters chosen, the simulation converges within 48 iterations over nearly the entire domain of forward and backward pump powers. This is shown in figure 5.6, which was generated by comparing the excited state population fraction N of the final outward and inward propagation solutions. Specifically, the z scale is calculate according to the formula $log_{10}[\sum(N_{outward}(z) - N_{inward}(z))^2]$, and the blue and turquoise regions represent areas where this value differs by <= 0.1% indicating convergence. The simulation is unstable at high backward pump powers with zero forward pump. For all the results shown in this section the algorithm converged successfully.

In this section we described a hybrid method of simulating a 60.5 MHz, 1550 nm, pulse propagation down an Erbium doped fiber pumped at 980 nm, which uses a SSFM to solve the NLSE embedded in a RK4 algorithm to propagate the laser rate equations. This coupling allows for uncompromising capture of both fundamental laser physics like gain saturation and pump depletion along with fiber dispersion and nonlinear effects. The results of this simulation were compared to a simpler saturable absorber gain model, and it was shown that the two models disagree with regard to the nature of the power buildup in the amplifier as well as the final frequency domain spectrum. At this time we do not have experimental results to directly compare to the models, but this would be a natural next step in designing the next generation EDFA for the OPA. With the ultrafast optics world employing more non linear EDFAs in creative ways, high fidelity modeling will be important in the future.

6. Toward Isolated Attosecond Pulse (IAP) Generation

This thesis described the construction of a high power MIR frequency comb which generates 3 μm, 100 fs pulses, with 6.7 W of average power, and 14.9 W of 1.55 μm light. Also reported is an experiment to generate high harmonics in PPLN waveguides, performed using our frequency comb, and accompanying analysis which has shown consistency between our experiment, and an experiment performed at NIST [30], with a simulation that models cascaded $\chi^{(2)}$ processes. Thus proposing an answer to a question originally asked in their groundbreaking work—"By what mechanism is the light generated [in PPLN Waveguides]?"—cascaded $\chi^{(2)}$ processes.

Although, the PPLN waveguide experiment made a meaningful contribution to the science of high harmonic generation (HHG) in solids, it was not the primary scientific objective of our laser system. Therefore, I would like to return to the original path by discussing three questions. Where are we now? Where do we want to go and why? And, how are we going to get there?

Beginning with where do we want to go? The ultimate objective of this laser systems is to generate phase stable isolated attosecond pulses (IAP) at high repetition rates ($\sim$ MHz), which are a probe for studying light-matter interaction on attosecond time scales. As a point of reference, it takes an electron in the 1s orbital of the hydrogen atom $\sim$ 152 as to orbit the nucleus [17]. The realization of the dream to develop a usable, "turn key", IAP frequency comb would be a major step toward enabling further apparatus. Such as, attosecond time resolved (real space) photo emission microscopy (atto-PEEM), which was first proposed in 2007 and still yet to be realized due to light source limitations (principally the lack of high repetition rate sources) [69]. In addition to being foreseeably rich in fundamental science, exploring light matter interaction on the attosecond time scale has practical applications like raising the efficiency of solar cells through better understanding the photocatalytic process [13].

One possible road to IAPs begins with making high harmonics in crystals like Zinc Oxide (ZnO) [26], or Zinc Selenide ($ZnSe$) [41]. In the experiment to generate high harmonics in PPLN waveguides, we observed bellow band gap harmonics only, and showed that the harmonic generating mechanism is perturbative, cascaded $\chi^{(2)}$. The next focus of this project will be on making non-perturbative above band gap harmonics. At laser induced electric fields on the order of the band gap of the material, thinking of the nonlinear polarization as a small perturbation to the crystal (equation 1.8) is no longer valid. Figure 6.1 illustrates two pathways in momentum space, intra-band and inter-band currents, which can generate high harmonics in solids. In the presence of a strong laser field an electron tunnels to the conduction band where it can either oscillate (intra-band current) and radiate, or recombine with a hole in the valence band (inter-band current) and radiate.

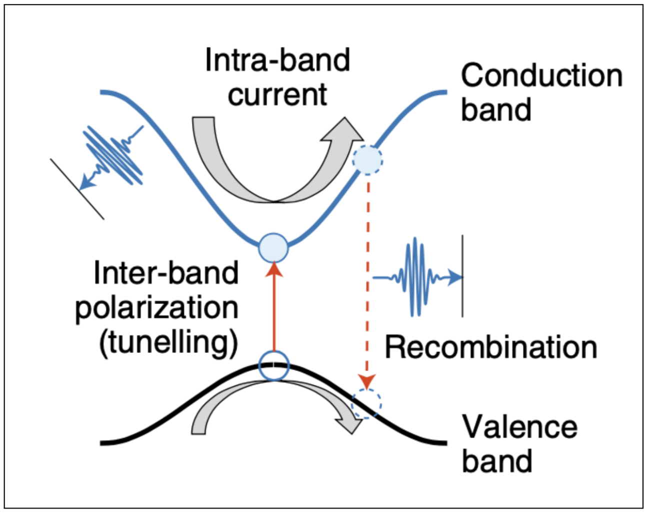

Figure 6.1: Concept drawing depicting 2 generation process for above band gap harmonics, taken from [25]. The electron promoted to the conduction band can oscillate within the conduction band and radiate. This is known as intra-band current. Or the electron can re-combine with the hole in the valance band, or another hole in a nearby lattice site, and radiate. This is known as inter-band current.

There are established methods to model non-perturbative SS-HHG, such as solving the semiconductor Bloch equations, or methods based on time-dependent density-functional theory (TDDFT) [77]. And there are available DFT software packages like "Octopus" which have been recently used by the Max Planck Institute to model SS-HHG [35]. The mathematical treatment and accompanying simulation of this physics is a next possible step in this project.

However, one benchmark we could compare to right now is an intensity of 1 TW/cm^2, which recent experiments have shown to be the order of magnitude needed for MIR drivers to generate non-perturbative above bang gap harmonics in materials like Zn0 and ZnSe [26], [41]. Currently, our OPA generates pulses which are 100 fs, 5 W average power, have a qualitatively good spatial mode (as viewed on a camera), and autocorrelations suggest are relatively unchirped. In the part 3 of this thesis I presented a model for and Erbium Doped Fiber Amplifier (EFDA), and have included simulation code in the appendix which can model the rest of the elements of the design for the phase 2 OPA signal seed branch. If phase 2 signal can seed the OPA with broadband temporally compressed pulses, then our calculations show that approximately 400 nm of idler bandwidth can be generated, which corresponds to about 40 fs transform limited pulse duration. Simulations, indicate that the pulse will be normally chirped and can be compressed to this transform limit in a prism pair compressor. This would yield a 4 optical cycle, 3 μm, pulse with a peak power of 2 MW, and if focused down to a 100 μm^2 spot size ($\sim 3\lambda$ waist, which clean spatial mode suggests is straightforward [1]) this would achieve an intensity of 2 TW/cm^2 And this is consistent with the aforementioned 1 TW/cm^2 need to generate above band gap high harmonics in materials commonly used for this purpose.

So for arguments sake, lets say the OPA is capable of generating harmonics above the band gap in ZnO up to harmonic number 18. In order to motivate how harmonics up to N=18 (160 nm) wavelength could generate and attosecond pulse train, consider the toy model shown in figure 6.2. To generate this plot cosine waves with frequency $n * \omega_0$ (where n is an integer) were added together in phase

---

[1] Also, in order to couple into the PPLN waveguide we already achieved spot sizes of this order

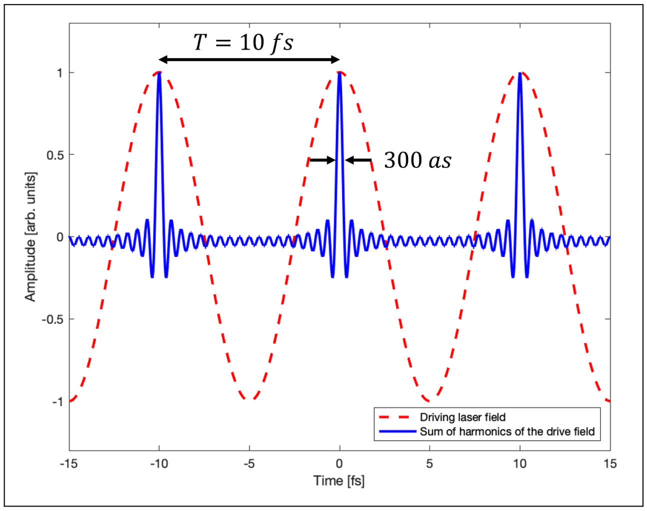

Figure 6.2: Simple model demonstrating how the coherent superposition of 18 harmonics of a 100 THz fundamental can yield attosecond pulse durations. The more harmonics that are added the shorter duration the attosecond burst becomes.

and this results in a pulse train of 300 *as* bursts. However, it is important to note that for intra-band currents the attosecond burst is generated every 1/2 cycle of the optical field, which are the turning points of the electron oscillating in the conduction band (figure 6.1). Fortunately, the OPA will be capable of producing 4 cycle driving fields, but the problem still remains of isolating 1 attosecond pulse from the 8 necessary to generate an attosecond burst which could occur at ever 1/2 cycle [2]

There are a few methods which have been developed to isolate a single attosecond pulse from the pulse train [16]. And the one which I've chosen to explain is two color polarization gating. As previously mentioned, intra-band

---

[2] This is an oversimplification which doesn't consider that not every cycle of the electric field under the envelope will have the strength $\sim 0.5\ V/A$, which is the order of magnitude needed to produce high harmonics.

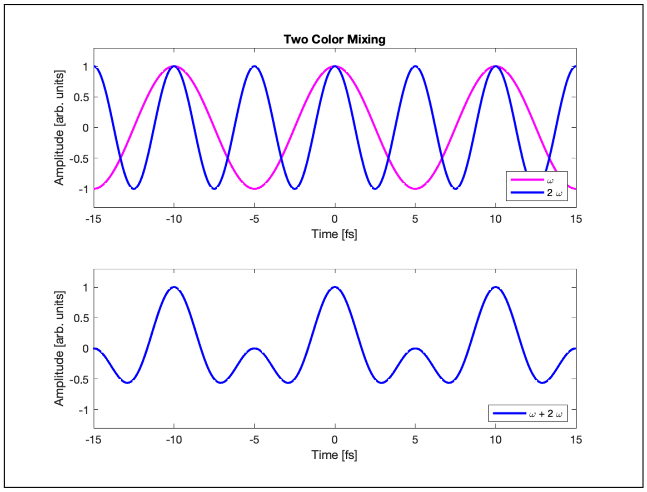

Figure 6.3: Conceptual illustration of two color gating method. Electric fields at frequencies ω and 2ω (top) are mixed in order to break the symmetry of the driving field, which causes the attosecond burst to be generated on every 1 cycle of the field instead of every 1/2 cycle.

currents generate attosecond pulses which occur at every 1/2 cycle of the driving field. Therefore, any method chosen to isolate a single attosecond pulse would need a "pass gate" which is no longer than 5 fs (1/2 cycle). However, by mixing ω and 2ω (in our case that's the 100 THz idler and 200 THz signal) the symmetry of the HHG drive field can be broken, and this is shown in figure 6.3. In this case, the attosecond burst will be generated every 1 cycle which relaxes the gating requirement to 10 fs. Using the two color mixing scheme makes the attosecond pulses easier to gate, but the two color scheme is not itself a gating method.

In order to isolate 1 attosecond pulse, a polarization gate could be employed. Figure 6.4 shows how a polarization gate can be construed by using a superposition of left and right hand circularly polarized light as the driving field for the harmonic generation process. When the pulses with opposite polarization are mixed there is

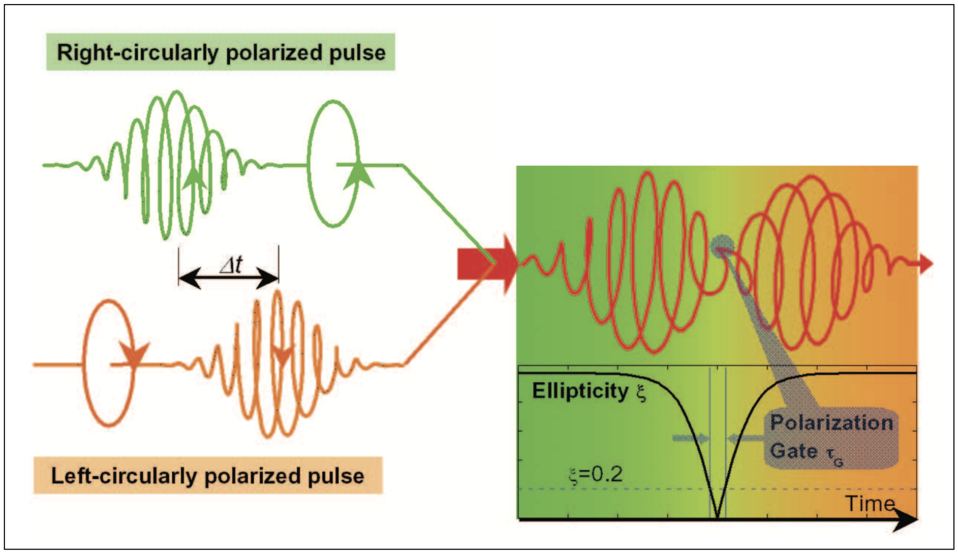

Figure 6.4: Polarization gating method where the HHG driving field is a superposition of right and left circularly polarized light with time delay τ. The resulting time dependent ellipticity drops sharply to 0 in a small window of time, and this constitutes the "gate" in which attosecond pulses can be made. This figure is from [66]

a sub-cycle time frame when the polarization of their superposition is linear, and this corresponds to the gate being open. The attosecond bursts generated at other times are suppressed by the ellipticity of the driving field. The paper this figure was taken from [66], was an experiment in attosecond pulse generation from gas phase HHG, but solid state HHG has shown similar dependence on ellipticity [76].

So, once again, let's say for arguments sake that the optics engineering challenges I have described above have been overcome, then the question becomes—how do we measure the duration of an isolated attosecond pulse? The first logical step might be to investigate whether the harmonic emission is confined to less than an optical cycle (i.e. < 10 fs). Although challenging, this measurement is still within the realm of traditional ultrafast measurement techniques—such as cross correlation FROG (XFROG) which utilizes DFG in an ultra-thin ($5\ \mu m$) BBO crystal—which has demonstrated the capability to measure 3 fs pulses [12]. Measuring absolute pulse durations less than a few fs is a tour de force experiment in its own right. One method which has been implemented in experiments that generate attosecond pulses via gas-phase HHG is the FROG-CRAB method (Frequency Resolved Optical Gating for Complete Reconstruction of Attosecond Bursts) [47]. In this method the attosecond burst is used to generate photoelectrons which are born into the presence of an additional MIR field which can be controlled with a variable delay τ. Recording the spectrogram of photoelectron energy vs. τ encodes the duration of the attosecond pulse. However, the FROG-CRAB method is based on gas-phase photoelectron spectroscopy, and the gas-phase nature is critical to assumptions in the reconstruction algorithm [17]. Surface photoemission experiments have been measuring electron dynamics on the attosecond time scales using attosecond streaking (fundamentally similar to FROG-CRAB), but the reconstruction requires the XUV pulse duration be measured in a separate gas-phase experiment [55, 57]. In principle, surface photoemission experiments can be used to directly characterize the duration of the attosecond pulses, perhaps using the knowledge of surface electron dynamics gained from these experiments.

Bibliography

[1] Florian Adler et al. “Phase-stabilized, 1.5 W frequency comb at 2.8–4.8 μm”. In: *Opt. Lett.* 34.9 (May 2009), pp. 1330–1332. DOI: `10.1364/OL.34.001330`. URL: `http://ol.osa.org/abstract.cfm?URI=ol-34-9-1330`.

[2] Govind P Agrawal. “Effect of gain dispersion and stimulated Raman scattering on soliton amplification in fiber amplifiers”. In: *Optics letters* 16.4 (1991), pp. 226–228.

[3] Govind P Agrawal. “Nonlinear fiber optics”. In: *Nonlinear Science at the Dawn of the 21st Century*. Springer, 2000, pp. 195–211.

[4] Caroline B Alden et al. “Methane leak detection and sizing over long distances using dual frequency comb laser spectroscopy and a bootstrap inversion technique”. In: *Atmos. Meas. Tech. Discuss.* 2017 (2017), pp. 1–34.

[5] Gunnar Arisholm, Rüdiger Paschotta, and Thomas Südmeyer. “Limits to the power scalability of high-gain optical parametric amplifiers”. In: *J. Opt. Soc. Am. B* 21.3 (Mar. 2004), pp. 578–590. DOI: `10.1364/JOSAB.21.000578`. URL: `http://josab.osa.org/abstract.cfm?URI=josab-21-3-578`.

[6] Morten Bache and Roland Schiek. “Review of measurements of Kerr nonlinearities in lithium niobate: the role of the delayed Raman response”. In: *arXiv preprint arXiv:1211.1721* (2012).

[7] Stéphane Balac. “High order embedded Runge-Kutta scheme for adaptive step-size control in the Interaction Picture method”. In: (2013).

[8] Stéphane Balac and Fabrice Mahé. “Embedded Runge–Kutta scheme for step-size control in the interaction picture method”. In: *Computer Physics Communications* 184.4 (2013), pp. 1211–1219.

[9] Andrius Baltuška, Takao Fuji, and Takayoshi Kobayashi. “Controlling the carrier-envelope phase of ultrashort light pulses with optical parametric amplifiers”. In: *Physical review letters* 88.13 (2002), p. 133901.

[10] Philippe M Becker, Anders A Olsson, and Jay R Simpson. *Erbium-doped fiber amplifiers: fundamentals and technology*. Elsevier, 1999.

[11] Robert W Boyd. *Nonlinear optics*. Academic press, 2020.

[12] Christian Brahms et al. “Direct characterization of tuneable few-femtosecond dispersive-wave pulses in the deep UV”. In: *Optics Letters* 44.4 (2019), pp. 731–734.

[13] James L Brooks et al. “Toward a mechanistic understanding of plasmon-mediated photocatalysis”. In: *Nanophotonics* 7.11 (2018), pp. 1697–1724.

[14] P. Bryan Changala et al. “Rovibrational quantum state resolution of the C60 fullerene”. In: *Science* 363.6422 (2019), pp. 49–54. ISSN: 0036-8075. DOI: `10.1126/science.aav2616`. eprint: `https://science.sciencemag.org/content/363/6422/49.full.pdf`. URL: `https://science.sciencemag.org/content/363/6422/49`.

[15] Sien Chi, Chir-Weei Chang, and Senfar Wen. “Femtosecond soliton propagation in erbium-doped fiber amplifiers: the equivalence of two different models”. In: *Optics communications* 106.4-6 (1994), pp. 193–196.

[16] Michael Chini, Kun Zhao, and Zenghu Chang. “The generation, characterization and applications of broadband isolated attosecond pulses”. In: *Nature Photonics* 8.3 (2014), pp. 178–186.

[17] Marcello F Ciappina et al. “Attosecond physics at the nanoscale”. In: *Reports on Progress in Physics* 80.5 (2017), p. 054401.

[18] M Conforti, F Baronio, and C De Angelis. “Ultrabroadband optical phenomena in quadratic nonlinear media”. In: *IEEE Photonics Journal* 2.4 (2010), pp. 600–610.

[19] Matteo Conforti, Fabio Baronio, and Costantino De Angelis. “Nonlinear envelope equation for broadband optical pulses in quadratic media”. In: *Physical Review A* 81.5 (2010), p. 053841.

[20] *Covesion Guide to PPLN: Material properties of Lithium Niobate*. `https://www.covesion.com/support/covesion-guide-to-ppln/material-properties-of-lithium-niobate.html`. Accessed: 2019-09-30.

[21] Flavio C. Cruz et al. “Mid-infrared optical frequency combs based on difference frequency generation for molecular spectroscopy”. In: *Opt. Express* 23.20 (Oct. 2015), pp. 26814–26824. DOI: `10.1364/OE.23.026814`. URL: `http://www.opticsexpress.org/abstract.cfm?URI=oe-23-20-26814`.

[22] A. Foltynowicz et al. “Cavity-enhanced optical frequency comb spectroscopy in the mid-infrared application to trace detection of hydrogen peroxide”. In: *Applied Physics B* 110.2 (2013), pp. 163–175. DOI: `10.1007/s00340-012-5024-7`. URL: `https://doi.org/10.1007/s00340-012-5024-7`.

[23] Tara Fortier and Esther Baumann. “20 years of developments in optical frequency comb technology and applications”. In: *Communications Physics* 2.1 (2019), pp. 1–16.

[24] Christian Gaida et al. “Watt-scale super-octave mid-infrared intrapulse difference frequency generation”. In: *Light: Science & Applications* 7.1 (2018), p. 94. DOI: `10.1038/s41377-018-0099-5`. URL: `https://doi.org/10.1038/s41377-018-0099-5`.

[25] Shambhu Ghimire and David A. Reis. “High-harmonic generation from solids”. In: *Nature Physics* 15.1 (2019), pp. 10–16. DOI: `10.1038/s41567-018-0315-5`. URL: `https://doi.org/10.1038/s41567-018-0315-5`.

[26] Shambhu Ghimire et al. “Observation of high-order harmonic generation in a bulk crystal”. In: *Nature physics* 7.2 (2011), pp. 138–141.

[27] C Randy Giles and Emmanuel Desurvire. “Modeling erbium-doped fiber amplifiers”. In: *Journal of lightwave technology* 9.2 (1991), pp. 271–283.

[28] Barry Gross and Jamal T Manassah. “Numerical solutions of the Maxwell–Bloch equations for a fiber amplifier”. In: *Optics letters* 17.5 (1992), pp. 340–342.

[29] Ben Henderson et al. “Laser spectroscopy for breath analysis: towards clinical implementation”. In: *Applied Physics B* 124.8 (2018), p. 161.

[30] Daniel D. Hickstein et al. “High-harmonic generation in periodically poled waveguides”. In: *Optica* 4.12 (Dec. 2017), pp. 1538–1544. DOI: `10.1364/OPTICA.4.001538`. URL: `http://www.osapublishing.org/optica/abstract.cfm?URI=optica-4-12-1538`.

[31] Daniel D Hickstein et al. “High-harmonic geneoration in periodically poled waveguides”. In: *Optica* 4.12 (2017), pp. 1538–1544.

[32] Nathan Hinkley et al. “An atomic clock with 10–18 instability”. In: *Science* 341.6151 (2013), pp. 1215–1218.

[33] Andreas Hugi et al. “Mid-infrared frequency comb based on a quantum cascade laser”. In: *Nature* 492.7428 (2012), pp. 229–233. DOI: `10.1038/nature11620`. URL: `https://doi.org/10.1038/nature11620`.

[34] Oc-Yeub Jeon et al. “Broadband optical parametric generation in the telecommunication band and simultaneous RGB generation by quasi-phase-matched parametric conversion processes”. In: *Journal of the Korean Physical Society* 49.9 (2006), p. 589.

[35] Nicolai Klemke et al. “Polarization-state-resolved high-harmonic spectroscopy of solids”. In: *Nature communications* 10.1 (2019), pp. 1–7.

[36] Yohei Kobayashi and Kenji Torizuka. “Measurement of the optical phase relation among subharmonic pulses in a femtosecond optical parametric oscillator”. In: *Optics letters* 25.11 (2000), pp. 856–858.

[37] A. Kowligy et al. “Efficient wideband UV/visible frequency comb generation via cascaded high-harmonic generation in lithium niobate waveguides”. In: *In preparation* (2020).

[38] Karol Krzempek et al. “Stabilized all-fiber source for generation of tunable broadband fCEO-free mid-IR frequency comb in the 7 – 9 m range”. In: *Opt. Express* 27.26 (Dec. 2019), pp. 37435–37445. DOI: `10.1364/OE.27.037435`. URL: `http://www.opticsexpress.org/abstract.cfm?URI=oe-27-26-37435`.

[39] Lyuba Kuznetsova, Andy Chong, and Frank W Wise. “Interplay of nonlinearity and gain shaping in femtosecond fiber amplifiers”. In: *Optics letters* 31.17 (2006), pp. 2640–2642.

[40] L Kuznetsova et al. “Chirped-pulse amplification near the gain-narrowing limit of Yb-doped fiber using a reflection grism compressor”. In: *Applied Physics B* 88.4 (2007), pp. 515–518.

[41] AA Lanin et al. “Mapping the electron band structure by intraband high-harmonic generation in solids”. In: *Optica* 4.5 (2017), pp. 516–519.

[42] Kevin F. Lee et al. “Harmonic generation in solids with direct fiber laser pumping”. In: *Opt. Lett.* 42.6 (Mar. 2017), pp. 1113–1116. DOI: `10.1364/OL.42.001113`. URL: `http://ol.osa.org/abstract.cfm?URI=ol-42-6-1113`.

[43] Xinlong Li et al. “High-power ultrafast Yb:fiber laser frequency combs using commercially available components and basic fiber tools”. In: *Review of Scientific Instruments* 87.9, 093114 (2016), p. 093114. DOI: `http://dx.doi.org/10.1063/1.4962867`. URL: `http://scitation.aip.org/content/aip/journal/rsi/87/9/10.1063/1.4962867`.

[44] Robert Lindberg et al. “Accurate modeling of high-repetition rate ultrashort pulse amplification in optical fibers”. In: *Scientific reports* 6 (2016), p. 34742.

[45] LW Liou and Govind P Agrawal. “Solitons in fiber amplifiers beyond the parabolic-gain and rate-equation approximations”. In: *Optics communications* 124.5-6 (1996), pp. 500–504.

[46] Kevin Luke et al. “Broadband mid-infrared frequency comb generation in a Si3N4 microresonator”. In: *Optics Letters* 40.21 (2015), pp. 4823–4826. DOI: `10.1364/OL.40.004823`. URL: `http://ol.osa.org/abstract.cfm?URI=ol-40-21-4823`.

[47] Yann Mairesse and F Quéré. “Frequency-resolved optical gating for complete reconstruction of attosecond bursts”. In: *Physical Review A* 71.1 (2005), p. 011401.

[48] Jamal T Manassah and Barry Gross. “Propagation of femtosecond pulses in a fiber amplifier”. In: *Optics communications* 122.1-3 (1995), pp. 71–82.

[49] C Manzoni and G Cerullo. “Design criteria for ultrafast optical parametric amplifiers”. In: *Journal of Optics* 18.10 (Aug. 2016), p. 103501. DOI: `10.1088/2040-8978/18/10/103501`. URL: `https://doi.org/10.1088%2F2040-8978%2F18%2F10%2F103501`.

[50] Daniel L. Maser et al. “Coherent frequency combs for spectroscopy across the 3–5 micron region”. In: *Applied Physics B* 123.5 (2017), p. 142. ISSN: 1432-0649. DOI: `10.1007/s00340-017-6714-y`. URL: `http://dx.doi.org/10.1007/s00340-017-6714-y`.

[51] PR Morkel and Richard I Laming. “Theoretical modeling of erbium-doped fiber amplifiers with excited-state absorption”. In: *Optics letters* 14.19 (1989), pp. 1062–1064.

[52] COMSOL Multiphysics. *COMSOL Multiphysics® v. 5.4. www.comsol.com. COMSOL AB, Stockholm, Sweden.®*.

[53] Y Nishida et al. “Direct-bonded QPM-LN ridge waveguide with high damage resistance at room temperature”. In: *Electronics Letters* 39.7 (2003), pp. 609–611.

[54] Lora Nugent-Glandorf, Fabrizio R. Giorgetta, and Scott A. Diddams. “Open-air, broad-bandwidth trace gas sensing with a mid-infrared optical frequency comb”. In: *Applied Physics B* 119.2 (2015), pp. 327–338. DOI: `10.1007/s00340-015-6070-8`. URL: `https://doi.org/10.1007/s00340-015-6070-8`.

[55] WA Okell et al. “Temporal broadening of attosecond photoelectron wavepackets from solid surfaces”. In: *Optica* 2.4 (2015), pp. 383–387.

[56] Vinicius Silva de Oliveira et al. “Intensity Noise Optimization of a Mid-Infrared Frequency Comb Difference Frequency Generation Source”. In: *arXiv:1904.02611* (2019).

[57] Marcus Ossiander et al. “Absolute timing of the photoelectric effect”. In: *Nature* 561.7723 (2018), pp. 374–377.

[58] C Paré and P-A Bélanger. “Optical solitary waves in the presence of a Lorentzian gain line: limitations of the Ginzburg–Landau model”. In: *Optics communications* 145.1-6 (1998), pp. 385–392.

[59] M Peroni and M Tamburrini. “Gain in erbium-doped fiber amplifiers: a simple analytical solution for the rate equations”. In: *Optics letters* 15.15 (1990), pp. 842–844.

[60] Tenio Popmintchev et al. “Bright Coherent Ultrahigh Harmonics in the keV X-ray Regime from Mid-Infrared Femtosecond Lasers”. In: *Science* 336.6086 (2012), pp. 1287–1291. DOI: `10.1126/science.1218497`. eprint: `http://www.sciencemag.org/content/336/6086/1287.full.pdf`. URL: `http://www.sciencemag.org/content/336/6086/1287.abstract`.

[61] William H Press et al. *Numerical recipes 3rd edition: The art of scientific computing*. Cambridge university press, 2007.

[62] Q Ru et al. “Two-octave-wide (3-12 {\mu} m) mid-infrared frequency comb produced as an optical subharmonic in a nondispersive cavity”. In: *arXiv preprint arXiv:2007.02496* (2020).

[63] Axel Ruehl et al. “Widely-tunable mid-infrared frequency comb source based on difference frequency generation”. In: *Opt. Lett.* 37.12 (June 2012), pp. 2232–2234. DOI: `10.1364/OL.37.002232`. URL: `http://ol.osa.org/abstract.cfm?URI=ol-37-12-2232`.

[64] Helge Rütz et al. “Quantum frequency conversion between infrared and ultraviolet”. In: *Physical Review Applied* 7.2 (2017), p. 024021.

[65] Marcus Seidel et al. “Multi-watt, multi-octave, mid-infrared femtosecond source”. In: *Science Advances* 4.4 (2018). DOI: `10.1126/sciadv.aaq1526`. eprint: `http://advances.sciencemag.org/content/4/4/eaaq1526.full.pdf`. URL: `http://advances.sciencemag.org/content/4/4/eaaq1526`.

[66] Bing Shan, Shambhu Ghimire, and Zenghu Chang. “Generation of the attosecond extreme ultraviolet supercontinuum by a polarization gating”. In: *Journal of modern optics* 52.2-3 (2005), pp. 277–283.

[67] A.E. Siegman. *Lasers*. University Science Books, 1986. ISBN: 9780935702118.

[68] Peter W Smith. “Mode-locking of lasers”. In: *Proceedings of the IEEE* 58.9 (1970), pp. 1342–1357.

[69] Mark I Stockman et al. “Attosecond nanoplasmonic-field microscope”. In: *Nature Photonics* 1.9 (2007), pp. 539–544.

[70] Henry Timmers et al. “Molecular fingerprinting with bright, broadband infrared frequency combs”. In: *Optica* 5.6 (2018), pp. 727–732.

[71] Henry Timmers et al. “Molecular fingerprinting with bright, broadband infrared frequency combs”. In: *Optica* 5.6 (June 2018), pp. 727–732. DOI: `10.1364/OPTICA.5.000727`. URL: `http://www.osapublishing.org/optica/abstract.cfm?URI=optica-5-6-727`.

[72] Th Udem, Ronald Holzwarth, and Theodor W Hänsch. “Optical frequency metrology”. In: *Nature* 416.6877 (2002), pp. 233–237.

[73] Giulio Vampa et al. “Characterization of high-harmonic emission from ZnO up to 11eV pumped with a Cr:ZnS high-repetition-rate source”. In: *Opt. Lett.* 44.2 (Jan. 2019), pp. 259–262. DOI: `10.1364/OL.44.000259`. URL: `http://ol.osa.org/abstract.cfm?URI=ol-44-2-259`.

[74] Sergey Vasilyev et al. "Super-octave longwave mid-infrared coherent transients produced by optical rectification of few-cycle 2.5-μm pulses". In: *Optica* 6.1 (Jan. 2019), pp. 111–114. DOI: `10.1364/OPTICA.6.000111`. URL: `http://www.osapublishing.org/optica/abstract.cfm?URI=optica-6-1-111`.

[75] Gabriel Ycas, Steve Osterman, and Scott A. Diddams. "Generation of a 660–2100 nm laser frequency comb based on an erbium fiber laser". In: *Opt. Lett.* 37.12 (June 2012), pp. 2199–2201. DOI: `10.1364/OL.37.002199`. URL: `http://ol.osa.org/abstract.cfm?URI=ol-37-12-2199`.

[76] Yong Sing You, David A Reis, and Shambhu Ghimire. "Anisotropic high-harmonic generation in bulk crystals". In: *Nature physics* 13.4 (2017), pp. 345–349.

[77] Chao Yu, Shicheng Jiang, and Ruifeng Lu. "High order harmonic generation in solids: a review on recent numerical methods". In: *Advances in Physics: X* 4.1 (2019), p. 1562982.

[78] Jia Yu et al. "34-fs, all-fiber all-polarization-maintaining single-mode pulse nonlinear amplifier". In: *Optics express* 24.15 (2016), pp. 16630–16637.

[79] Chuankun Zhang et al. "A noncollinear enhancement cavity for record-high out-coupling efficiency of extreme-UV frequency comb". In: *arXiv preprint arXiv:2003.02429* (2020).

[80] Feng Zhu et al. "High-power mid-infrared frequency comb source based on a femtosecond Er:fiber oscillator". In: *Opt. Lett.* 38.13 (July 2013), pp. 2360–2362. DOI: `10.1364/OL.38.002360`. URL: `http://ol.osa.org/abstract.cfm?URI=ol-38-13-2360`.

A. GNLSE Solver

This example code solves the Generalized Nonlinear Schrodinger Equation (GNLSE) for pulse propagation down optical fibers, and includes the effects of Kerr nonlinearity and Ramam Scattering [3]. The ERK3(4) algorithm [8] is an adaptive step size method which controls the local error to less than a specified tolerance [61] .

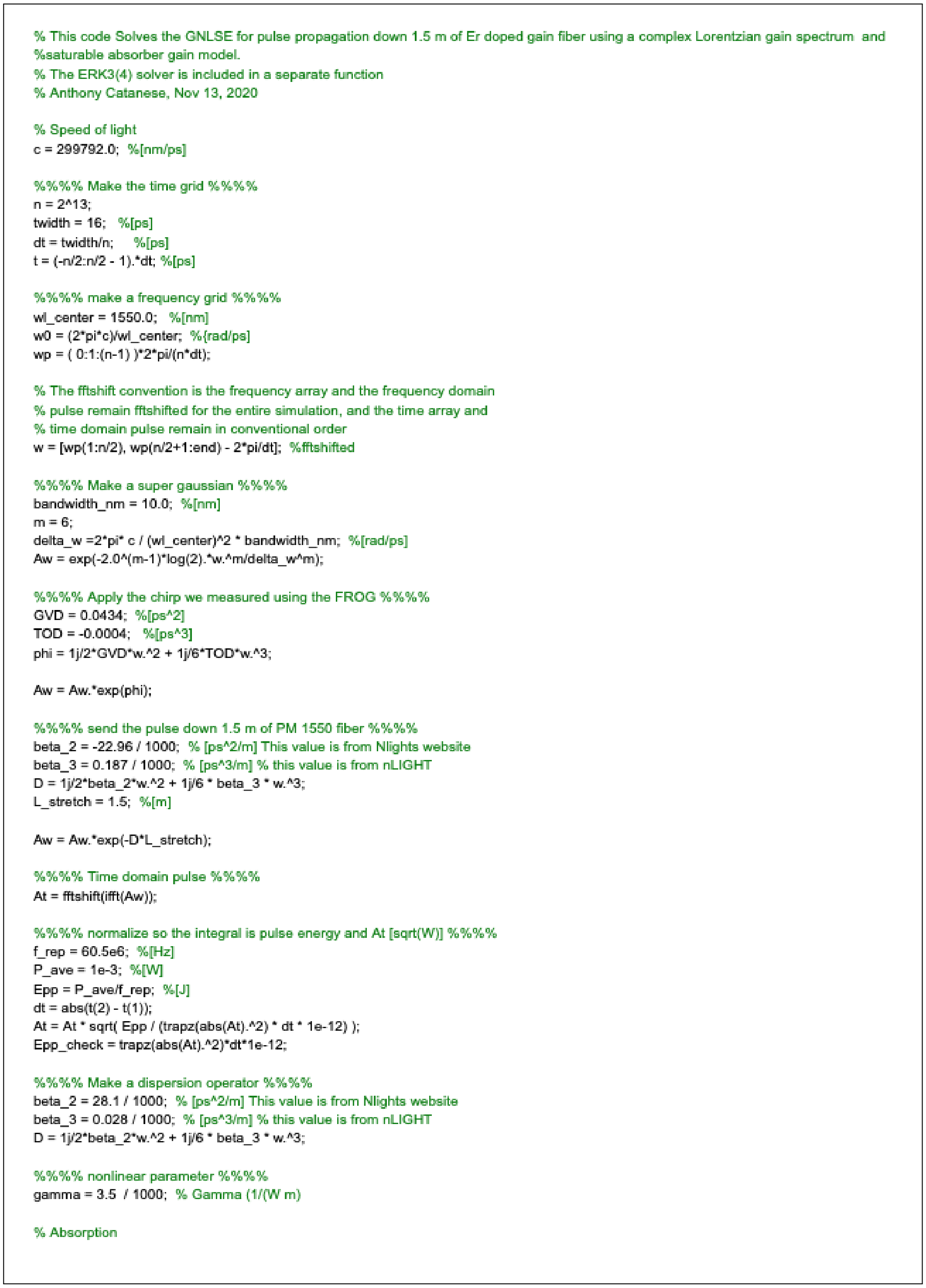

```
% This code Solves the GNLSE for pulse propagation down 1.5 m of Er doped gain fiber using a complex Lorentzian gain spectrum  and
%saturable absorber gain model.
% The ERK3(4) solver is included in a separate function
% Anthony Catanese, Nov 13, 2020

% Speed of light
c = 299792.0;  %[nm/ps]

%%%% Make the time grid %%%%
n = 2^13;
twidth = 16;   %[ps]
dt = twidth/n;     %[ps]
t = (-n/2:n/2 - 1).*dt; %[ps]

%%%% make a frequency grid %%%%
wl_center = 1550.0;   %[nm]
w0 = (2*pi*c)/wl_center;  %{rad/ps]
wp = ( 0:1:(n-1) )*2*pi/(n*dt);

% The fftshift convention is the frequency array and the frequency domain
% pulse remain fftshifted for the entire simulation, and the time array and
% time domain pulse remain in conventional order
w = [wp(1:n/2), wp(n/2+1:end) - 2*pi/dt];  %fftshifted

%%%% Make a super gaussian %%%%
bandwidth_nm = 10.0;  %[nm]
m = 6;
delta_w =2*pi* c / (wl_center)^2 * bandwidth_nm;  %[rad/ps]
Aw = exp(-2.0^(m-1)*log(2).*w.^m/delta_w^m);

%%%% Apply the chirp we measured using the FROG %%%%
GVD = 0.0434;  %[ps^2]
TOD = -0.0004;   %[ps^3]
phi = 1j/2*GVD*w.^2 + 1j/6*TOD*w.^3;

Aw = Aw.*exp(phi);

%%%% send the pulse down 1.5 m of PM 1550 fiber %%%%
beta_2 = -22.96 / 1000;  % [ps^2/m] This value is from Nlights website
beta_3 = 0.187 / 1000;  % [ps^3/m] % this value is from nLIGHT
D = 1j/2*beta_2*w.^2 + 1j/6 * beta_3 * w.^3;
L_stretch = 1.5;  %[m]

Aw = Aw.*exp(-D*L_stretch);

%%%% Time domain pulse %%%%
At = fftshift(ifft(Aw));

%%%% normalize so the integral is pulse energy and At [sqrt(W)] %%%%
f_rep = 60.5e6;  %[Hz]
P_ave = 1e-3;  %[W]
Epp = P_ave/f_rep;  %[J]
dt = abs(t(2) - t(1));
At = At * sqrt( Epp / (trapz(abs(At).^2) * dt * 1e-12) );
Epp_check = trapz(abs(At).^2)*dt*1e-12;

%%%% Make a dispersion operator %%%%
beta_2 = 28.1 / 1000;  % [ps^2/m] This value is from Nlights website
beta_3 = 0.028 / 1000;  % [ps^3/m] % this value is from nLIGHT
D = 1j/2*beta_2*w.^2 + 1j/6 * beta_3 * w.^3;

%%%% nonlinear parameter %%%%
gamma = 3.5  / 1000;  % Gamma (1/(W m)

% Absorption
```

```
alpha = 0.0;

%%%% Fiber length %%%%
L = 1.5;  %[m]

%%%% Gain %%%%
saturation_energy = 1e-9;  %[J]
g0 = 7.65;  %full power pump forward and backward

g=@(Epp, g0) g0*1./(1+Epp/saturation_energy);  % Gain vs. z
Er_gain_bandwidth_nm = 35.0;  %[nm]
Er_delta_w = Er_gain_bandwidth_nm/1550.0 * 2*pi*c./1550.0;  %bandwidth [rad/ps]
Gw = -w./(Er_delta_w/2) ./ (1+w.^2./(Er_delta_w/2).^2) + 1j./(1+w.^2./(Er_delta_w/2).^2);  % gain profile

%%%% Raman For Undoped Fused Silica from Agrawal, 6th edition, section 2.3.3 %%%%
fr = 0.245;
tau1 = 0.0122; %[ps]
tau2 = 0.032;  %[ps]
hr = (tau1^(-2) + tau2^(-2))*tau1 * exp(-t/tau2).*sin(t/tau1);
fb = 0.21;
taub = 0.096;  %[ps]
RT = (1-fb)*hr + fb*( (2*taub - t)/taub^2 ).*exp(-t/taub); %[1/ps]
RT(t<0) = 0;                % heaviside step function
RW = (fft(fftshift(RT)));  %[1/ps]
RW = RW * 1/(sqrt(max(abs(RW).^2)));  % normalize to peak amplitude 1

%%%% Call the solver %%%%
[w, AW, z, Epp_save] = ERK34(t, At, w, w0, gamma, D, g, g0, Gw, RW, fr, L);
%%%%%%%%%%%%%%%%%%%%%%%%%

%% Plot the results

% Normalize them so that the integral of any size in z sums up to the
% average power in the pulse
P_ave_vec = Epp_save * f_rep * 1e3;  % Average Power [mW]
df = abs(w(2)-w(1))/(2*pi);
PW = zeros(length(z), length(w));
for pp=1:length(z)
    temp = fftshift(abs(AW(pp, :)).^2);
    PW(pp, :) = temp * P_ave_vec(pp) / (trapz(temp).*df);
    % Check this normalization
    %P_ave_check = trapz(PW(pp, :))*df
end

fig = figure();
set(gcf, 'Position',  [500, 500, 800, 1200])

subplot(411)
plot(fftshift(w+w0)/(2*pi), PW(end, :), "LineWidth", 2, "color", 'b')
title("Final Frequency Domain Pulse")
xlabel("Frequency [THz]")
ylabel("Spectral Power Density [mW/THz]")
xlim([w0/(2*pi)-10, w0/(2*pi)+10])
set(gca,'FontSize',14)

subplot(412)
% Plot a heat map of the frequency domain
[W, Z] = meshgrid((fftshift(w)+w0)/(2*pi), z);

h = surf(W, Z, PW);
colormap jet
xlim([w0/(2*pi)-10, w0/(2*pi)+10])
title("Frequency Domain vs. Propagation Distance z")
xlabel("Frequency [THz]")
ylabel("Propagation Distance z [m]")
```

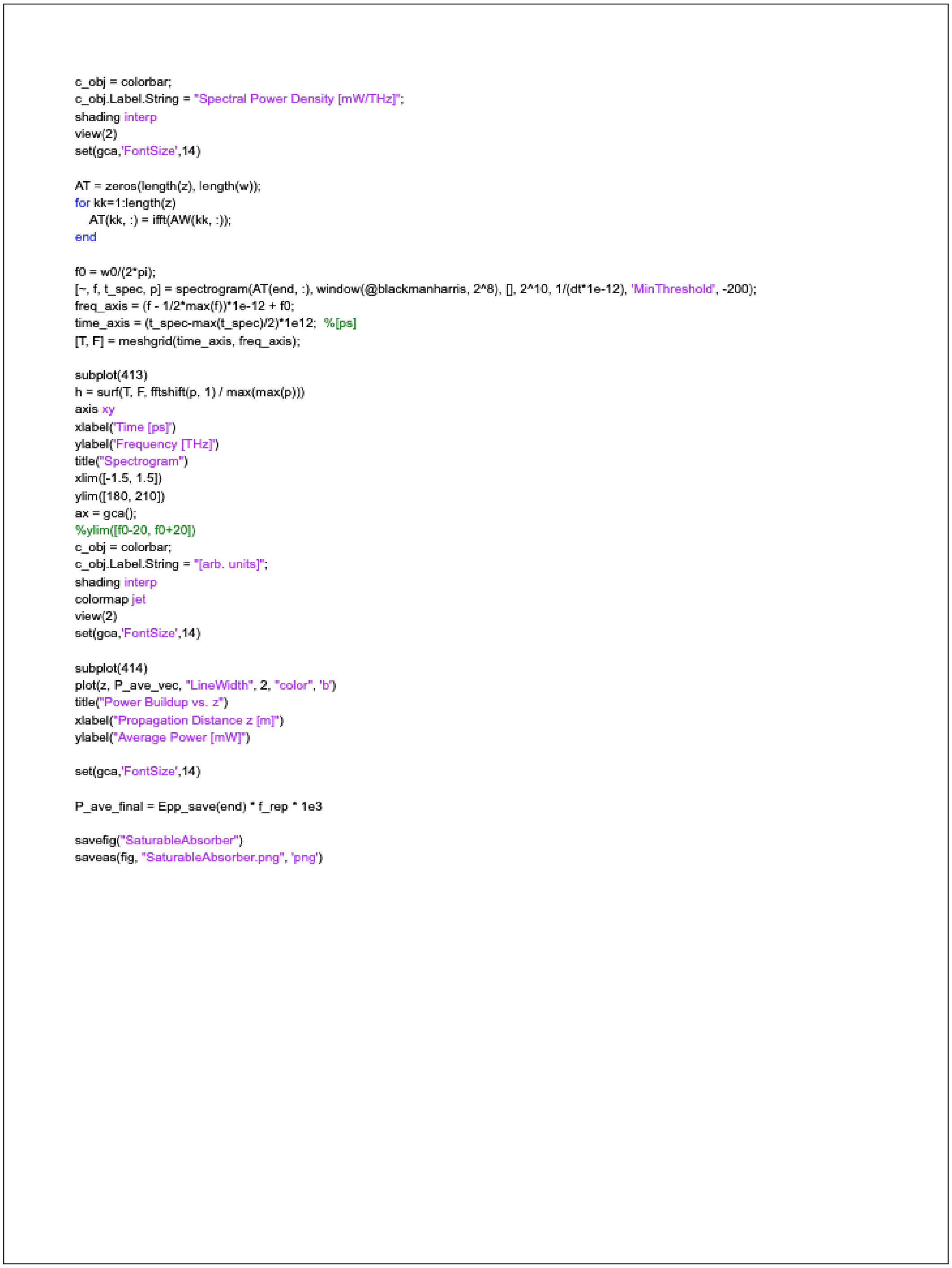

```
c_obj = colorbar;
c_obj.Label.String = "Spectral Power Density [mW/THz]";
shading interp
view(2)
set(gca,'FontSize',14)

AT = zeros(length(z), length(w));
for kk=1:length(z)
   AT(kk, :) = ifft(AW(kk, :));
end

f0 = w0/(2*pi);
[~, f, t_spec, p] = spectrogram(AT(end, :), window(@blackmanharris, 2^8), [], 2^10, 1/(dt*1e-12), 'MinThreshold', -200);
freq_axis = (f - 1/2*max(f))*1e-12 + f0;
time_axis = (t_spec-max(t_spec)/2)*1e12;  %[ps]
[T, F] = meshgrid(time_axis, freq_axis);

subplot(413)
h = surf(T, F, fftshift(p, 1) / max(max(p)))
axis xy
xlabel('Time [ps]')
ylabel('Frequency [THz]')
title("Spectrogram")
xlim([-1.5, 1.5])
ylim([180, 210])
ax = gca();
%ylim([f0-20, f0+20])
c_obj = colorbar;
c_obj.Label.String = "[arb. units]";
shading interp
colormap jet
view(2)
set(gca,'FontSize',14)

subplot(414)
plot(z, P_ave_vec, "LineWidth", 2, "color", 'b')
title("Power Buildup vs. z")
xlabel("Propagation Distance z [m]")
ylabel("Average Power [mW]")

set(gca,'FontSize',14)

P_ave_final = Epp_save(end) * f_rep * 1e3

savefig("SaturableAbsorber")
saveas(fig, "SaturableAbsorber.png", 'png')
```

```
% The ERK3(4) solver takes in the following parameters:
%
%   't'
%   time â€˜tâ€™ [ps] (1D row vector)
%   'At'
%   frequency domain electric field â€˜Atâ€™ [sqrt(W)], (1D row vector)
%   'w'
%   frequency â€˜wâ€™ [rad/ps], (1D row vector), fftshifted
%   'w0'
%   central frequency, â€˜w0â€™ [rad/ps], scalar
%   'gamma'
%   chi^3 nonlinear scale factor â€˜gammaâ€™ [1/m], scalar
%   'D'
%   dispersion Operator 'D' [1/m], (1D row vector), fftshifted
%   'g'
%   gain amplitude callable function 'g' [1/m]
%   'g0'
%   gain amplitude coefficient 'g_0' [1/m], scalar
%   'Gw'
%   gain spectrum 'Gw', (1D row vector), fftshifted
%   'RW'
%   frequency domain Raman response 'RW', normalized to max amplitude 1, (1D row
%   vector), fftshifted
%   'fr'
%   Raman fraction 'fr', scalar quantity
%   'length'
%   Fiber propagation distance 'length' [1/m]
%
% The ERK3(4) solver returns the following values
%
%   'w'
%   Final frequency domain grid 'w' [rad/ps], (1D row vector), fftshifted
%   'AW'
%   Final frequency domain pulse 'AW' [sqrt(W)] (z_steps, length(w)), fftshifted
%   'z'
%   The location at which the electric field is saved 'z' [m], (1D row vector)
%   'Epp_save'
%   The pulse energy at the save points 'Epp_save' [J]


function [w, AW, z, Epp_save] = ERK34(t, At, w, w0, gamma, D, g, g0, Gw, RW, fr, Length)

% Transpose everything to col vectors
t = transpose(t);  %[ps]
At = transpose(At);  %[sqrt(W)]
w = transpose(w);  %[rad/ps]
D = transpose(D);  %[1/m]
Gw = transpose(Gw); %[no units]
RW = transpose(RW); %[no units]

dt = abs(t(2) - t(1));  %[ps]

function cubic_nL = NL(z, AT, w, gamma, RW, fr, w0, t)

  % Calculate the time domain intensity
  IT = abs(AT).^2;

  % Convolve the Raman response
  RS = ifft(fft(IT).*RW);

  % Add the Kerr and Raman terms together
  KR = AT.*(1-fr).*IT + AT.*fr.*RS;

  % Take the derivative in the frequency domain
  dKRdt = ifft(1j*w.*fft(KR));
```

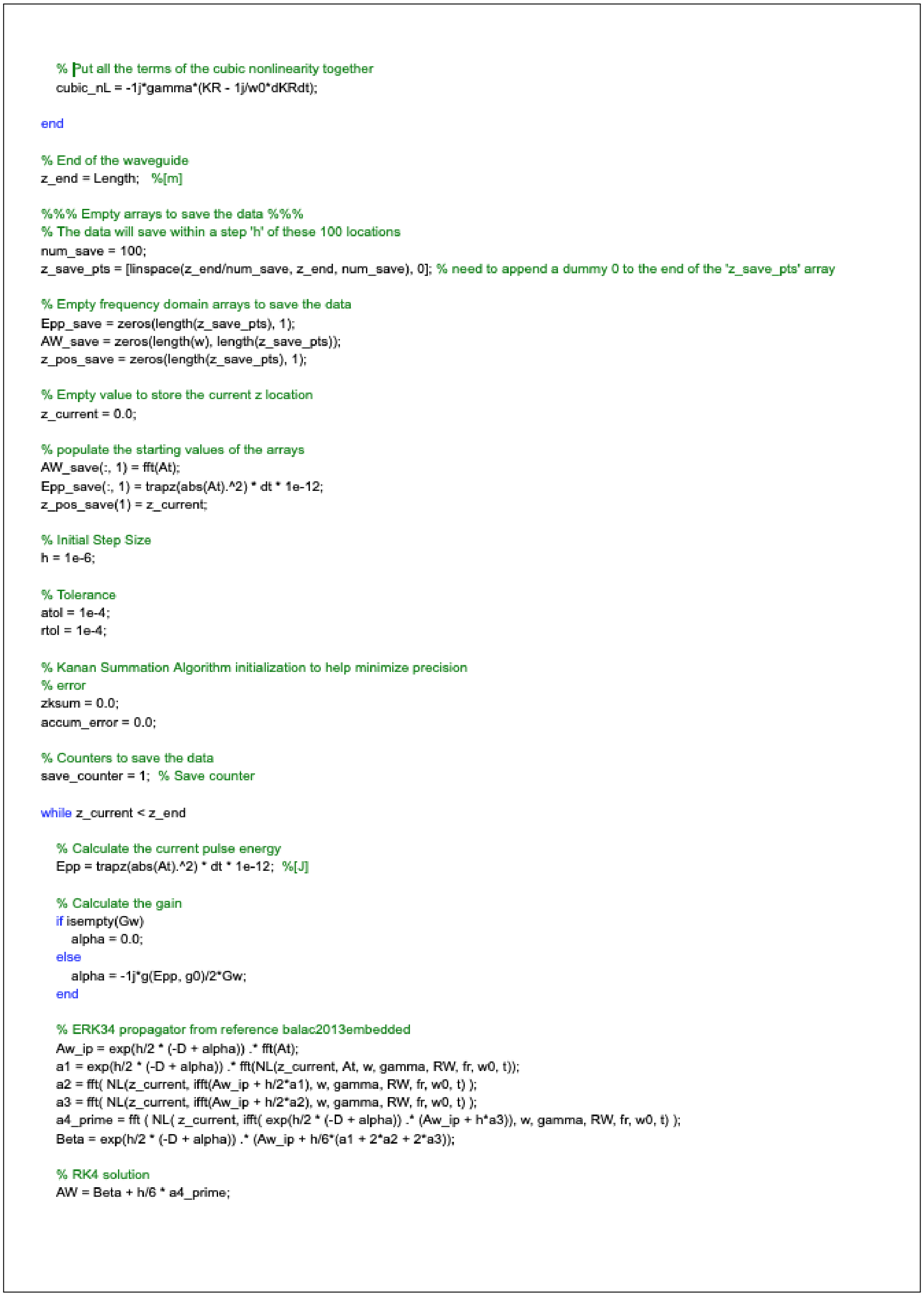

```
    % Put all the terms of the cubic nonlinearity together
    cubic_nL = -1j*gamma*(KR - 1j/w0*dKRdt);

end

% End of the waveguide
z_end = Length;   %[m]

%%% Empty arrays to save the data %%%
% The data will save within a step 'h' of these 100 locations
num_save = 100;
z_save_pts = [linspace(z_end/num_save, z_end, num_save), 0]; % need to append a dummy 0 to the end of the 'z_save_pts' array

% Empty frequency domain arrays to save the data
Epp_save = zeros(length(z_save_pts), 1);
AW_save = zeros(length(w), length(z_save_pts));
z_pos_save = zeros(length(z_save_pts), 1);

% Empty value to store the current z location
z_current = 0.0;

% populate the starting values of the arrays
AW_save(:, 1) = fft(At);
Epp_save(:, 1) = trapz(abs(At).^2) * dt * 1e-12;
z_pos_save(1) = z_current;

% Initial Step Size
h = 1e-6;

% Tolerance
atol = 1e-4;
rtol = 1e-4;

% Kanan Summation Algorithm initialization to help minimize precision
% error
zksum = 0.0;
accum_error = 0.0;

% Counters to save the data
save_counter = 1;  % Save counter

while z_current < z_end

    % Calculate the current pulse energy
    Epp = trapz(abs(At).^2) * dt * 1e-12;  %[J]

    % Calculate the gain
    if isempty(Gw)
        alpha = 0.0;
    else
        alpha = -1j*g(Epp, g0)/2*Gw;
    end

    % ERK34 propagator from reference balac2013embedded
    Aw_ip = exp(h/2 * (-D + alpha)) .* fft(At);
    a1 = exp(h/2 * (-D + alpha)) .* fft(NL(z_current, At, w, gamma, RW, fr, w0, t));
    a2 = fft( NL(z_current, ifft(Aw_ip + h/2*a1), w, gamma, RW, fr, w0, t) );
    a3 = fft( NL(z_current, ifft(Aw_ip + h/2*a2), w, gamma, RW, fr, w0, t) );
    a4_prime = fft ( NL( z_current, ifft( exp(h/2 * (-D + alpha)) .* (Aw_ip + h*a3)), w, gamma, RW, fr, w0, t) );
    Beta = exp(h/2 * (-D + alpha)) .* (Aw_ip + h/6*(a1 + 2*a2 + 2*a3));

    % RK4 solution
    AW = Beta + h/6 * a4_prime;
```

```
    % Time domain temporary RK4 solution
    At_temp = ifft(AW);

    % RK3 solution used to determine the error in the step
    AW3 = Beta + h/30 * ( 2*a4_prime + 3 * fft( NL(z_current + h, At_temp, w, gamma, RW, fr, w0, t) ) );

    % The logic for controlling the step size is right from Numerical
    % Recipes 17.2
    Delta = abs(AW - AW3);
    scale = atol + abs(AW) * rtol;
    err = norm( (Delta ./ scale).^2 );

    % if err > 1 then discard this round and try again with a larger step
    % size
    if err > 1
        h = h * 0.2;
       continue
    end

    % Assign the temporary value of the time domain electric field to the
    % for the next round of the loop
    At = At_temp;

    % Kahan summation algorithm to reduce floating point adding error
    temp_num = h + accum_error;
    temp_sum = zksum + temp_num;
    accum_error = temp_num - (temp_sum - zksum);
    zksum = temp_sum;

    % update the position of the solver from the Kahan summation
    z_current = zksum;

    % Save Data logic
    if abs( (z_current - z_save_pts(save_counter)) ) < h

        % Save the current z location
        z_pos_save(save_counter + 1) = z_current;

        fprintf('%05.1f %% complete\n', z_pos_save(save_counter + 1)/z_end*100);

        % Save the pulse energy
        Epp_save(save_counter + 1) = trapz(abs(At).^2) * dt * 1e-12;  % Pulse energy in [J]

        % Save the current Frequency Domain Electric Field
        AW_save(:, save_counter + 1) = AW;

        % Advance the save counter
        save_counter = save_counter + 1;
    end

    % Update the step size
    h = h * max( 0.2, min(10, 0.9*(1/err)^(1/4)) );

    % Guarantee that the algorithm takes at least 2 steps between every
    % save point
    if h > Length / (2*num_save)
        h = Length / (2*num_save);
    end

end

% Transpose the arrays so they are all row vectors, and the frequency grid
% marches down the z axis
w = transpose(w);
AW = transpose(AW_save);
```

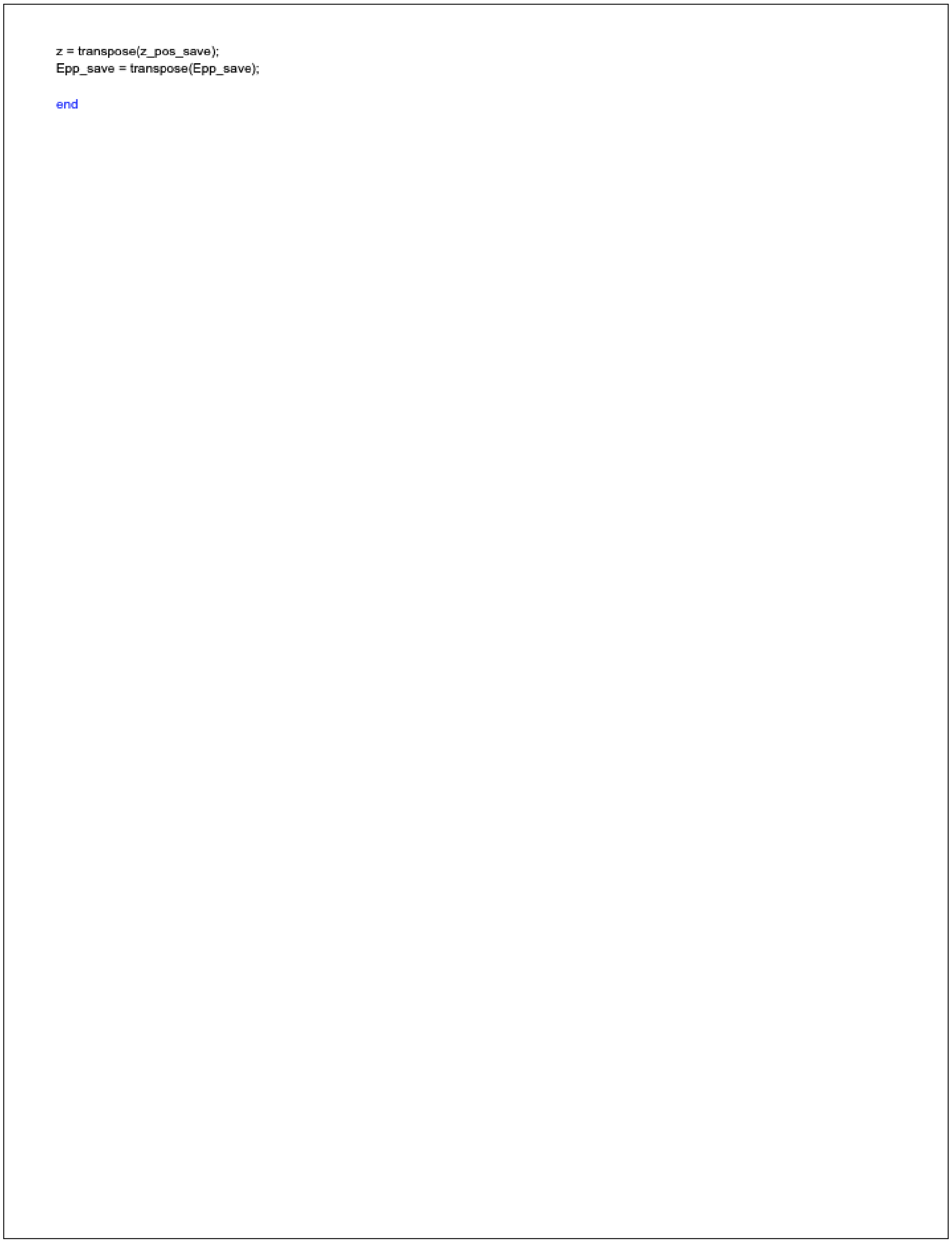

```
z = transpose(z_pos_save);
Epp_save = transpose(Epp_save);

end
```